

On the simulation of ship motions induced by extreme waves

A dissertation submitted in partial fulfillment of the requirements for the degree of
Doctor of Philosophy at George Mason University

By

Haidong Lu
Master of Engineering
University of Shanghai for Science and Technology, 2004
Bachelor of Engineering
University of Shanghai for Science and Technology, 2001

Director: Dr. Chi Yang, Professor
Department of Computational and Data Sciences

Fall Semester 2009
George Mason University
Fairfax, VA

Copyright © 2009 by Haidong Lu
All Rights Reserved

Dedication

To my dear parents and grandpa.

Acknowledgments

I am very much obliged to my advisor, Dr. Chi Yang, for her kind guidance and support in all aspects during the past five years at Mason. She guides me to the ‘deep water’ in ocean engineering; more important, she shows me how to ‘sail’ there with no fear.

I feel thankful to Dr. Rainald Löhner, my committee member and the director of our CFD group. In his classes, he teaches the fundamental skills of CFD; in seminars each semester, he shows the depth and width of the application of CFD; in the computer code of FEFLO, he demonstrates the exact way to generate the power of CFD. I feel lucky to use FEFLO in my research and enjoy the fun of CFD.

I also would like to thank other two committee members, Dr. Francis Noblesse and Dr. Jeng-Eng Lin. Dr. Noblesse always encourages me to throw a ‘pure’ mechanic view on many problems in hydrodynamics. Dr. Lin has always been ready to give his inspiring advice in my study of PDE and in my thesis work.

I am grateful to my colleagues at CFD group: Drs. Juan Cebal, Fernando Camelli, Fernando Mut, Hyunyul Kim for their kindness and help. I feel thankful to my friends at CDS department and other departments of Mason, though most of them have left for new careers after graduation.

I also owe a big deal to my old teachers and friends from China for their considerations and kind concerns. Quite a few of my old friends are also pursuing their dreams around the world, such as U.S., U.K., Canada. With them, I enjoy the friendship beyond time and space.

This research is partially supported by the Office of Naval Research (ONR) and the Naval Surface Warfare Center, Carderock Division (NSWCCD). Their support made this research possible, and I am very grateful.

Finally, I would like to thank my parents for their love and care and everything.

Table of Contents

	Page
List of Tables	vii
List of Figures	viii
Abstract	xii
1 Introduction	1
1.1 Ship Motions in Extreme Waves and Relevant Problems	1
1.1.1 Ship-type Offshore Units in Offshore Engineering	1
1.1.2 Green Water Problem	3
1.1.3 Ship-ship Hydrodynamic Interactions at Offloading Operation	4
1.2 Experiments and Numerical Solutions	4
1.2.1 Model Tests	4
1.2.2 Numerical Approaches	6
1.3 Outline of the Dissertation	9
2 Numerical Methods	11
2.1 Introduction	11
2.2 Basic Elements of the Solver	12
2.3 Temporal Discretization	13
2.4 Spatial Discretization	16
2.4.1 The advection operator	17
2.4.2 The divergence operator	18
2.5 Volume of Fluid Extensions	19
2.5.1 Extrapolation of the Pressure	19
2.5.2 Extrapolation of the Velocity	20
2.5.3 Imposition of Constant Mass	21
2.5.4 Deactivation of Air Region	22
2.6 Rigid Body Motion and Mesh Movement	22
2.7 A Simple Mooring Cable Model	23
2.8 Wavemaker	24
3 Validations	25
3.1 Introduction	25

3.2	Green Water Overtopping a Fixed Deck	25
3.2.1	Setup	25
3.2.2	Results	28
3.3	Green Water on the Deck of an FPSO Model	36
3.3.1	Setup	36
3.3.2	Results	39
3.4	Two Side-by-side Boxes Moored in Dam-breaking Waves	45
3.5	Closure	48
4	Case Studies	51
4.1	Introduction	51
4.2	Single FPSO in Extreme Waves	52
4.3	FPSO Model Moored in Extreme Waves	60
4.4	Two Side-by-side Vessels Moored in Extreme Waves	63
4.4.1	Freely Moving Side-by-side FPSO and LNGC	65
4.4.2	Side-by-side FPSO and LNGC with Spread Mooring constraints	68
4.4.3	Side-by-side FPSO and LNGC with Side Mooring constraints	68
4.5	Ships with Different Mooring Configurations	80
4.5.1	Freely-Moving FPSO and LNGC in Tandem	81
4.5.2	FPSO and LNGC in Tandem with Cross-mooring Cable Constrains	82
4.5.3	Comparisons of Different Configurations	83
4.6	Closure	83
5	Summary and Conclusions	89
5.1	Summary and Conclusions	89
5.2	Future Work	90
	Bibliography	91

List of Tables

Table	Page
3.1 Wavemaker Motions	27
3.2 Main particulars for FPSO	36
4.1 Main particulars for FPSO model and LNGC model	65

List of Figures

Figure	Page
1.1 FPSO <i>YÙUM K'AK'NÁAB</i> , BW Offshore	2
1.2 LNGC <i>Arctic Princess</i> , Höegh LNG	2
1.3 The main phases of the green water problem schematically	3
2.1 Extrapolation of the pressure	20
2.2 Extrapolation of the velocity	21
3.1 Definition sketch of green water overtopping problem	26
3.2 Wavemaker displacement in x direction	26
3.3 Comparison of wave elevation with experimental measurements: 1	28
3.4 Comparison of wave elevation with experimental measurements: 2	29
3.5 Comparison of free surface elevation at the leading edge position of the deck and twelve time instances used for velocity comparisons	31
3.6 Comparison of vertical variation of horizontal velocity u (m/s) for the case without the fixed deck	32
3.7 Comparison of vertical variation of horizontal velocity u (m/s) for the case with the fixed deck	33
3.8 Comparison of vertical distribution of velocity vector at the leading edge position of the fixed deck	34
3.9 Snapshots of green water overtopping a fixed deck	35
3.10 Sketch of the setup of model test	36
3.11 Problem definition of an FPSO in numerical seakeeping tank	37
3.12 Surface girds on the FPSO model	38
3.13 Time history of prescribed heave and pitch motions of FPSO model	39
3.14 Vertical displacement of water probe on the deck	39
3.15 Water height on deck	40
3.16 Wave elevation at a given position in front of the hull	40
3.17 FPSO model in extreme waves (top: full view; bottom: close view): 1	41
3.18 FPSO model in extreme waves (top: full view; bottom: close view): 2	42

3.19 FPSO model in extreme waves (left: full view; bottom: close view): 3 . . .	43
3.20 FPSO model in extreme waves (top: full view; bottom: close view): 4 . . .	44
3.21 Two identical boxes moored side-by-side in dam-breaking waves	45
3.22 Surface grids on walls and boxes: top–full view; bottom–close view	46
3.23 Comparison of motion responses between each box: surge, heave, and sway, respectively	47
3.24 Comparison of motion responses between each box: roll, yaw, and pitch, respectively	48
3.25 Snapshots of side-by-side moored boxes in extreme waves (1)	49
3.26 Snapshots of side-by-side moored boxes in extreme waves (2)	50
4.1 Comparison of heave and pitch motions	52
4.2 Comparison of the water height on deck	53
4.3 Absolute water height on deck	53
4.4 Vertical displacement of the wave probe on deck	54
4.5 Comparison of the wave elevation	54
4.6 Comparison of heave force and pitch moment	55
4.7 Snapshots of the free surface wave elevation (top: prescribed motion; bottom: freely moving (1)	56
4.8 Snapshots of the free surface wave elevation (top: prescribed motion; bottom: freely moving (2)	57
4.9 Snapshots of the free surface wave elevation (top: prescribed motion; bottom: freely moving (3)	58
4.10 Snapshots of the free surface wave elevation (top: prescribed motion; bottom: freely moving (4)	59
4.11 FPSO model moored in wave tank	60
4.12 Comparison of motion responses of FPSO model with and without mooring constraints	61
4.13 Comparison of the wave elevation at wave probe in front of the FPSO . . .	62
4.14 Vertical displacement of the wave probe on deck	62
4.15 Comparison of the water height on deck	63
4.16 Side-by-side FPSO and LNGC freely moving	63
4.17 Side-by-side FPSO and LNGC with different mooring configurations	64
4.18 Mesh configuration: surface grids on walls of the tank (top) and the ship bodies(bottom)	66

4.19	Motion responses of freely moving side-by-side FPSO and LNGC	67
4.20	Side-by-side FPSO and LNGC constrained with spread mooring cables . . .	68
4.21	Side-by-side FPSO and LNGC constrained with side mooring cables	69
4.22	Motion responses of side-by-side FPSO and LNGC with spread mooring cables	70
4.23	Motion responses of side-by-side FPSO and LNGC with side mooring cables	71
4.24	Comparison of motion responses of side-by-side FPSO and LNGC with or without mooring constraints (FPSO)	72
4.25	Comparison of motion responses of side-by-side FPSO and LNGC with or without mooring constraints (LNGC)	73
4.26	Snapshots of side-by-side FPSO and LNGC in extreme waves with or with- out mooring constraints (top: free; middle: spreading mooring constraint; bottom: side mooring constraint)	74
4.27	Snapshots of side-by-side FPSO and LNGC in extreme waves with or with- out mooring constraints (top: free; middle: spreading mooring constraint; bottom: side mooring constraint)	75
4.28	Snapshots of side-by-side FPSO and LNGC in extreme waves with or with- out mooring constraints (top: free; middle: spreading mooring constraint; bottom: side mooring constraint)	76
4.29	Snapshots of side-by-side FPSO and LNGC in extreme waves with or with- out mooring constraints (top: free; middle: spreading mooring constraint; bottom: side mooring constraint)	77
4.30	Snapshots of side-by-side FPSO and LNGC in extreme waves with or with- out mooring constraints (top: free; middle: spreading mooring constraint; bottom: side mooring constraint)	78
4.31	Snapshots of side-by-side FPSO and LNGC in extreme waves with or with- out mooring constraints (top: free; middle: spreading mooring constraint; bottom: side mooring constraint)	79
4.32	Problem definition of ships in tandem	80
4.33	Comparison of motion responses of freely-moving FPSO and LNGC in tan- dem configuration	81
4.34	Comparison of motion responses of FPSO and LNGC in tandem with cross- mooring cable constraints	82

4.35	Comparison of motion responses of freely-moving FPSO in side-by-side and in tandem configurations	84
4.36	Comparison of motion responses of freely-moving LNGC in side-by-side and in tandem configurations	85
4.37	Comparison of motion responses of FPSO in side-by-side and in tandem configurations with mooring cable constraints	86
4.38	Comparison of motion responses of LNGC in side-by-side and in tandem configurations with mooring cable constraints	87

Abstract

ON THE SIMULATION OF SHIP MOTIONS INDUCED BY EXTREME WAVES

Haidong Lu, PhD

George Mason University, 2009

Dissertation Director: Dr. Chi Yang

In rough sea conditions, ships or offshore structures may experience highly nonlinear phenomena such as slamming and green water on deck. Impact loads due to slamming and green water shipping are associated with highly nonlinear free surface flows. These impact loads can cause serious structural damages, and are of considerable concern to the stability and survivability of ships. There is a great need for calculation methods to simulate ship dynamics in extreme waves.

In this dissertation, a numerical seakeeping tank is developed to investigate ship motions induced by extreme waves. The numerical seakeeping tank is based on the coupling of a parallel incompressible flow solver, a Volume of Fluid (VOF) technique, and a simple mooring cable model. Specifically, an Arbitrary Lagrangian-Eulerian (ALE) frame of reference is used to handle the freely moving body. The incompressible Euler/Navier-Stokes equations in this frame are solved using projection schemes and a Finite Element Method (FEM) on unstructured grids. The VOF technique is used to capture the violent free surface motion. The simple mooring cable model is used to account for the mooring effects. The position of the ship is obtained based upon the solution of the general equations of rigid body motion with six degrees-of-freedom (6-DOF) in terms of the hydrodynamic forces and the mooring

cable tension forces acting on the ship.

Validations of the numerical seakeeping tank developed are first performed for the following problems: green water overtopping a fixed deck; green water on the deck of a ship model; and two side-by-side moored boxes in dam-breaking waves. Numerical results predicted by the present numerical seakeeping tank show fairly good agreement with the experimental measurements. The numerical seakeeping tanks is then used to investigate a single ship in extreme waves with or without mooring cable constraints, and multiple ships interactions in extreme waves with or with mooring cable constraints. Highly nonlinear wave-ship interactions and mooring effects have been modeled successfully.

Chapter 1: Introduction

1.1 Ship Motions in Extreme Waves and Relevant Problems

In a long history, ships have been used in a broad variety of human activities on water, such as transportation of goods and passengers, fishing, warfare, sports, and entertainments. For each type of ships engaged in different activities, there are requirements and setting limits considering reliability, safety, and economy. For example, oceangoing ships are designed to operated in a wave environment, which could turn to be very hostile sometimes. That results in engineering problems like large-amplitude motions of the ships and excessive structural loading on the hull associated with rough sea environment [1, 2].

These problems are particularly emphasized in offshore industry in recent decades [3]. Due to the increasing worldwide demand of energy, more vessels and offshore units have been designed and built for exploration and transportation of oil and Liquefied Natural Gas (LNG) in industry. Moreover, as drilling has been pushed into deep-water area, more and more vessels and offshore structures will be operating in rough sea conditions. Offloading of oil and gas in harsh environments is one of such examples which needs to be performed with great care.

In this dissertation, focusing on particular problems such as green water problem and mooring configurations for offloading operations in offshore engineering, a numerical sea-keeping tank is developed and used to predict ship motions induced by extremes waves. The same approach could also be applied to ship motion research in general.

1.1.1 Ship-type Offshore Units in Offshore Engineering

Faced with the increasing demand of energy, oil and gas exploration and production companies are drilling further out into the sea. Drilling in deep-water area requires development

of new offshore structures and facilities. More ship-type offshore units have thus been introduced in offshore engineering in recent decades, such as Floating Production Storage and Offloading units (FPSOs).



Figure 1.1: FPSO *YÙUM K'AK'NÁAB*, BW Offshore



Figure 1.2: LNGC *Arctic Princess*, Höegh LNG

The first FPSO in the Gulf of Mexico area, for instance, was installed in 2007 (see Figure 1.1). The *YÙUM K'AK'NÁAB* [4] in this figure was designed for operation for fifteen years at the Ku-Maloob-Zaap field, with its production capacity upto 200,000 barrels of oil per day (BOPD) and storage capacity of 2,500,000 barrels. Other common vessels in

offshore engineering include oil tankers, LNG carriers (LNGCs), and Floating Storage and Regasification Units (FSRU), etc. Figure 1.2 shows one of the largest LNGCs in the world – the *Arctic Princess*, which has the cargo capacity of $147,208\text{ m}^3$ [5].

Often moored permanently at a certain position at sea during one mission, FPSOs like *YÙUM K'AK'NÁAB* or other offshore structures are easier to confront harsh environments than other marine vessels. FPSOs in the Gulf of Mexico, for example, would be found in storm and high current conditions in hurricane seasons [6]. Growing concerns in offshore industry for safety, environment, and economy have brought forth a great need for investigation of vessels like FPSOs in rough sea conditions.

1.1.2 Green Water Problem

One common but complex problem arises to the safety and operability of an FPSO or an LNGC, like other vessels, is green water problem. This problem has been known in the maritime world for a long time: at rough sea or in heavy storms, ocean water flows on the deck of a vessel due to the large relative motion between ocean waves and the vessel. This problem is also known as ‘shipping of water’, ‘deck wetness’ or ‘green water loading’ [7,8].

Green water could cause severe damages to ship deck and other facilities on the deck, due to the impact loads of entering water on deck, as several accidents in field have been reported [9]. In order to understand the main physics of the green water problem, Buchner [7] has summarized the main phases of green water loading as shown in Figure 1.3 (left: top view; right: side view):

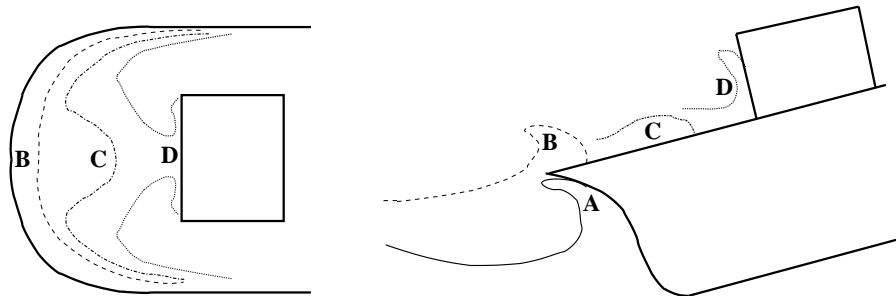


Figure 1.3: The main phases of the green water problem schematically

- A. Nonlinear swell-up around the bow;
- B. ‘Dam breaking’-type flow onto the deck;
- C. ‘Hydraulic jump’-type shallow water flow on the moving deck, focusing into a high velocity water ‘jet’ when the water fronts the sides meet; and
- D. Water impact and water run-up in front of the structure (the deckhouse in our model), eventually turning over.

Green water problem is thus associated with highly nonlinear free surface flows, which is very challenging to predict.

1.1.3 Ship-ship Hydrodynamic Interactions at Offloading Operation

Another common challenge is offloading of oil or LNG between terminals and tankers or other transport vessels – e.g., LNG offloading operations between an FPSO and an LNGC in deep-water, which need great attention to both the offloading techniques and mooring configurations of each vessel. Two mooring methods are widely used for offloading operations in offshore industry: side-by-side mooring configuration and tandem mooring configuration. Each of these two methods requires vessels to be maintained at an operational distance between each other.

Similar to single vessel case, two vessels in harsh weather conditions would also encounter the green water problem. Moreover, these two vessels also experience hydrodynamic interactions between each other. Special attentions, therefore, are required to deal with the free surface flow with wave-body interactions and mooring effects.

1.2 Experiments and Numerical Solutions

1.2.1 Model Tests

In order to investigate the green water effects as well as ship-ship hydrodynamic interactions with or without mooring constraints, both model tests and numerical simulations can be

carried out. Several model tests on green water problem, for example, have been conducted as follows.

Buchner [7] at MARIN has reported an extensive series of model tests on green water problem. The following problems have been studied: non-linear relative wave motions at the bow, water flow onto and on the bow deck, green water impact loading, and green water from the side and stern. A clear description of green water problem has been concluded based on experimental results.

Cox and Ortega [10] have successfully conducted experimental measurements on a green water overtopping problem using a narrow wave flume at Texas A&M University. By generating a transient wave composed of two sinusoidal waves with different periods and amplitudes, one large overtopping wave was produced in front of a fixed thin flat deck located above the initial still free surface.

Sames [11] has presented the research on the prediction of green water loads for a RORO passenger ferry. Focusing on the green water loads on the forward bulkhead of the superstructure of a RORO passenger ferry, he presented a detailed study of the European research project DEXTREMEL.

Li et al. [12] have conducted experimental measurement on green water problem on an FPSO model in the seakeeping tank at Shanghai Jiao Tong University. Restricted in heave and pitch motions, the FPSO model was encountering green water on bow area in extreme head waves. Water wave height at several locations on the deck was measured and recorded.

Ryu et al. [13] have investigated the run-up and green water velocities due to breaking waves impinging and overtopping problem, which was measured in a two dimensional (2-D) wave tank. Based on experimental measurements, a similarity profile for the green water flow on top of a structure was obtained by using dimensional analysis, and a prediction equation was also formulated.

Though great progresses have been made in modern experimental techniques and several experimental measurements have been carried out successfully as mentioned above, model tests in laboratories still could meet the limits. It is usually complicated and costly to

conduct a model test in laboratories in offshore engineering: it is difficult to set up measurement instruments a priori to cover all major details; furthermore, the challenges are increasing for model tests for tough sea conditions, such as large waves with a long time period and extreme deep water. On the other hand, numerical methods may overcome some of those difficulties and thus provide an alternative approach for predictions and partially replace model tests in laboratories.

1.2.2 Numerical Approaches

Numerical methods for predicting ship motion responses in waves have been widely used the marine community. For instance, potential flow based 2-D strip theory methods or 3-D panel methods can provide solutions either in the frequency domain or in the time domain. These methods are popular and effective in solving linear or non-linear free-surface flow problems. In recent years, the rapid development of computer hardware and software has enabled researchers to apply more complex fully nonlinear unsteady RANS/Navier-Stokes solvers to solve highly nonlinear free surface flow problems.

The main focus of this dissertation is to develop a computation tool for predicating large-amplitude motion responses of single FPSO model, side-by-side moored and tandem moored FPSO and LNGC in extreme waves. In order to investigate highly nonlinear hydrodynamic interactions including green water on deck, ship-ship hydrodynamic interactions, and mooring effects, the numerical model should be able to handle complex nonlinear free surface, so that the following phenomena can be modeled [7]:

- Water entry of a bow structure;
- Complex free surface flow onto the deck;
- ‘Hydraulic jump’-type shallow water flow on a moving ship deck;
- Short duration of water impact on a structure;
- Overturning flow after run-up of the water in front of the structure;

- Wave-body interactions;
- Ship-ship hydrodynamic interactions; and
- Mooring constraints.

Modern seakeeping computations are performed using a wide variety of techniques – from simple strip theory (e.g., Ogilvie and Tuck 1969 [14], Salvesen et al. 1970 [15], Kashiwagi et al. 2000 [16]) to complex fully nonlinear unsteady RANS/Navier-Stokes computations (e.g., Weymouth et al. 2005 [17], Hu and Kashiwagi 2007 [18]). The numerical simulation of the motion responses of side-by-side moored or tandem moored ships are far more difficult than the single ship seakeeping computations. Various approximations are adopted in the simulation studies of side-by-side moored ships (e.g., Buchner et al. 2001 [19], Hong et al. 2005 [20], Fournier et al. 2006 [21], Cho et al. 2007 [22], Naciri et al. 2007 [23]).

It is noteworthy that numerical methods based on potential theory have been developed for decades to simulate nonlinear wave problems (e.g., Wu and Eatock Taylor 1994 and 1995 [24, 25], Ma 2006 [26]), wave-body interactions (e.g., Kirkgöz and Mamak 2004 [27], Wang and Wu 2006 [28]), and green water problem (e.g., Trulsen et al. 2002 [29], Greco et al. 2005, [30]).

However, simulations of free surfaces associated with extreme waves problems need special attention because of the occurrence of large interface deformations and even topology changes. Methods based on potential theory mentioned above would break down when violent free surface motion occurs, e.g., overturning and breaking waves.

A variety of techniques have been developed to deal with free surface or interface, which include mesh-less methods and methods based on structure or unstructured grids [31–34]. Some researchers have also presented hybrid methods: Enright [35], for example, used “particle level set method” for the enhanced resolution of free surface flows in his dissertation work. In general, the computation of highly nonlinear free surface flows is difficult because neither the shape nor the position of the interface between air and water is known a priori; on the contrary, it often involves unsteady fragmentation and merging process.

For those mesh-based methods, there are basically two approaches to compute flows with free surface: interface-tracking and interface-capturing methods. The interface-tracking methods compute the water flow only, using a self-adjusted grid that adapts itself to the shape and position of free surface in each time step. This approach has been widely used in the numerical simulation of free surface flow problem (e.g., [26, 28, 36] in recent years). It was noted in literature (e.g., [33]) that simply following Lagrangian motion, a considerable distortion of grids could appear even if the interface is undergoing relatively mild deformation. This could be overcome by using methods in a mixed manner between the Lagrangian motion and the fixed Eulerian reference. This method, however, could not be used if the interface topology changes significantly (e.g., overturning or breaking waves).

On the other hand, the interface-capturing approach considers both fluids as a single effective fluid with variable properties, and the interface is captured as a region of sudden change in fluid properties. The interface-capturing methods based on the Eulerian approach require no geometry manipulations after the mesh is generated and thus can be applied to interfaces of a complex topology such as overturning or breaking waves. Three typical methods in this approach are Marker and Cell (MAC) method [37], Volume Of Fluid (VOF) method [38], and the level set method [39].

The VOF method is adopted and further developed in this dissertation. It was first reported by Nichols and Hirt in 1975 [38], and more completely by Hirt and Nichols in 1981 [40]. This method has been improved in several aspects in the recent years (e.g., Scardovelli and Zaleski 1999 [33]) and used to simulate breaking waves (e.g., Chen and Kharif 1999 [41], Biaisser et al. 2004[42]), green water effects (e.g., Fekken et al. 1999 [43], Huijsmans and van Groesen 2004 [44]), sloshing (e.g., Rhee 2005 [45], Yang and Löhner 2005 [46]), and large-amplitude ship motion responses with green water on deck (Yang et al. 2006, 2007a,b, Lu et al. 2008 [47–50]).

1.3 Outline of the Dissertation

In this dissertation, a single-phase VOF method is presented together with the coupling of an unstructured grid based Euler/Navier-Stokes finite-element flow solver to model the ship motions due to extreme waves. The mooring cables are modeled with a simple elastic cable model. Contact algorithms are also implemented to account for the contact forces between ships or ship and walls. Thus the position of the ship is obtained based upon the solution of the general equations of rigid body motion (6-DOF) and the hydrodynamic forces, the mooring cable tension forces, and contact forces acting on the ship. A steep regular wave is considered in all ship(s) motion cases, and generated using a piston-type wavemaker by moving the piston paddle with a sinusoidal excitation. A fixed grid is used to cover the space occupied by both the water and the air phase. An extrapolation algorithm is developed for obtaining the pressure and velocity in the air region. The surface nodes of the ship move according to a 6-DOF integration of the rigid body motion equations; approximately thirty layers of elements close to the ‘wavemaker plane’ and the ship are moved. The Navier-Stokes/VOF equations are integrated using an arbitrary Lagrangian-Eulerian frame of reference.

In short, the objective of this dissertation is to develop a numerical seakeeping tank: it could be used to simulate ship motions induced by extreme waves, to provide reliable information for most common problems occur in offshore engineering; it could also be used to conduct numerical investigations of other problems of hydrodynamics of free surface flows. This dissertation is presented in the following structure:

- Chapter 2 provides the description of the numerical methods used in the numerical seakeeping tank.
- Chapter 3 presents validations of the numerical seakeeping tank on following problems:
 1. Green water overtopping a fixed deck;
 2. Green water on the deck of an FPSO model in head waves; and

3. Two side-by-side moored identical boxes in dam-breaking waves.
- Chapter 4 presents the results of four case studies, focusing on ship motions induced by extreme waves:
 1. Freely moving FPSO model in extreme waves;
 2. FPSO model moored in extreme waves;
 3. Two side-by-side vessels moored in extremes waves; and
 4. Ship-ship interactions with different mooring configurations.
 - In Chapter 5, this dissertation is concluded with some recommendations for future work.

Chapter 2: Numerical Methods

2.1 Introduction

With the aim of modeling ship motions induced by extreme waves, a numerical seakeeping tank is developed in this dissertation. This numerical seakeeping tank is based on the coupling of a parallel incompressible flow solver, a Volume of Fluid (VOF) technique, and a simple mooring cable model.

Specifically, an Arbitrary Lagrangian-Eulerian (ALE) frame of reference is used to handle the freely moving body. The incompressible Euler/Navier-Stokes equations in this frame are solved using projection schemes and a Finite Element Method (FEM) on unstructured grids. The VOF technique is used to capture the violent free surface motion. The simple mooring cable model is used to account for the mooring effects. The position of the ship is obtained based upon the solution of the general equations of rigid body motion with six degrees-of-freedom (6-DOF) in terms of the hydrodynamic forces and the mooring cable tension forces acting on the ship. In addition, piston- or flap-type wavemakers are used to generate extreme waves in the numerical seakeeping tank.

Finally, the numerical seakeeping tank described above could handle highly nonlinear hydrodynamic interaction problems, such as green water on deck, sloshing, wave-body interaction, and mooring effects. In this chapter, numerical methods used in this numerical seakeeping tank are presented in following (also see Löhner [51]).

2.2 Basic Elements of the Solver

The governing equations in the fluid dynamics model applied in this dissertation are the incompressible Navier-Stokes equations, which are written in an ALE frame as follows,

$$\rho \mathbf{v}_{,t} + \rho \mathbf{v}_a \cdot \nabla \mathbf{v} + \nabla p = \nabla \cdot \mu \nabla \mathbf{v} + \rho \mathbf{g} \quad , \quad (2.1a)$$

$$\nabla \cdot \mathbf{v} = 0 \quad . \quad (2.1b)$$

Here ρ denotes the density, \mathbf{v} the velocity vector, p the pressure, μ the viscosity and \mathbf{g} the gravity vector. The advective velocity is given by $\mathbf{v}_a = \mathbf{v} - \mathbf{w}$, where \mathbf{w} is the mesh velocity. We remark that both the air and water phases are considered incompressible, thus Eqn. 2.1b.

The water-air interface is described by a scalar equation of the form:

$$\Phi_{,t} + \mathbf{v}_a \cdot \nabla \Phi = 0 \quad . \quad (2.2)$$

In the classic VOF technique, Φ represents the total density of the material in a cell/element or control volume. It is also noteworthy that for the level set approach, Φ represents the signed distance to the interface.

The incompressible Navier-Stokes equations given by Eqns. 2.1 are solved using projection schemes. The main elements of the numerical schemes are as follows:

- Spatial discretization using unstructured grids (in order to allow for arbitrary geometries and adaptive refinement);
- Spatial approximation of unknowns with simple finite elements (in order to have a simple input or output and code structure);
- Temporal approximation using implicit integration of viscous terms and pressure (the interesting scales are the ones associated with advection);

- Temporal approximation using explicit integration of advective terms;
- Low-storage, iterative solvers for the resulting systems of equations (in order to solve large 3-D problems); and
- Steady results that are independent from the chosen time-step (in order to have confidence in convergence studies).

Recently, efforts have been devoted to integrate the advective terms in a more efficient way, either through multi-stepping or implicit iterative solvers (Löhner, 2004 [52]; Löhner et al., 2007 [53]).

The computer code based on the numerical schemes described above with interface capture option (VOF technique) has been used to simulate a numerical wave tank, where the waves are generated by the sinusoidal excitation of a piston paddle, and a freely floating ship moves in response to the waves according to the hydrodynamic forces. Highly nonlinear wave-body interactions, such as slamming and green water on deck, have been modeled successfully (Yang and Löhner, 2006 [54]; Löhner et al., 2007 [53]; Yang et al., 2007 [48, 49]; Lu et al., 2008 [50, 55]).

2.3 Temporal Discretization

For most of the applications listed above, the important physical phenomena propagate with the advective timescales. It therefore could be assumed that the advective terms require an explicit time integration. Diffusive phenomena typically occur at a much faster rate, and can or should therefore be integrated implicitly. Given that the pressure establishes itself immediately through the pressure-Poisson equation, an implicit integration of pressure is also required. The hyperbolic character of the advection operator and the elliptic character of the pressure-Poisson equation have led to a number of so-called projection schemes. The key idea is to predict first a velocity field from the current flow variables without taking the divergence constraint into account. In a second step, the divergence constraint is enforced

by solving a pressure-Poisson equation. The velocity increment can therefore be separated into an advective-diffusive and pressure increment:

$$\mathbf{v}^{n+1} = \mathbf{v}^n + \Delta \mathbf{v}^a + \Delta \mathbf{v}^p = \mathbf{v}^* + \Delta \mathbf{v}^p \quad (2.3)$$

For an explicit (forward Euler) integration of the advective terms, with implicit integration of the viscous terms, one complete time-step is given by:

- Advective-Diffusive Prediction: $\mathbf{v}^n \longrightarrow \mathbf{v}^*$

$$\left[\frac{\rho}{\Delta t} - \theta \nabla \mu \nabla \right] (\mathbf{v}^* - \mathbf{v}^n) + \rho \mathbf{v}_a^n \cdot \nabla \mathbf{v}^n + \nabla p^n = \nabla \mu \nabla \mathbf{v}^n + \rho \mathbf{g}; \quad (2.4)$$

- Pressure Correction: $p^n \longrightarrow p^{n+1}$

$$\nabla \cdot \mathbf{v}^{n+1} = 0 \quad , \quad (2.5)$$

$$\rho \frac{\mathbf{v}^{n+1} - \mathbf{v}^*}{\Delta t} + \nabla (p^{n+1} - p^n) = 0 \quad , \quad (2.6)$$

which results in

$$\nabla \cdot \frac{1}{\rho} \nabla (p^{n+1} - p^n) = \frac{\nabla \cdot \mathbf{v}^*}{\Delta t} \quad ; \quad (2.7)$$

- Velocity Correction: $\mathbf{v}^* \longrightarrow \mathbf{v}^{n+1}$

$$\mathbf{v}^{n+1} = \mathbf{v}^* - \frac{\Delta t}{\rho} \nabla (p^{n+1} - p^n) \quad . \quad (2.8)$$

At steady state, $\mathbf{v}^* = \mathbf{v}^n = \mathbf{v}^{n+1}$ and the residual of the pressure correction vanish, implying that the result does not depend on the time-step Δt . The factor θ denotes the implicitness-factor for viscous terms ($\theta = 1$: first-order, fully implicit; $\theta = 0.5$ second-order,

Crank-Nicholson). One can replace the one-step explicit advective-diffusive predictor by a multistage Runge-Kutta scheme (Löhner, 2004 [52]), allowing for higher accuracy in the advection-dominated regions and larger time-steps without a noticeable increment in CPU cost. A k -step, time-accurate Runge-Kutta scheme of order k for the advective parts may be written as:

$$\rho \mathbf{v}^i = \rho \mathbf{v}^n + \alpha^i \gamma \Delta t (-\rho \mathbf{v}_a^{i-1} \cdot \nabla \mathbf{v}^{i-1} - \nabla p^n + \nabla \mu \nabla \mathbf{v}^{i-1}) \quad , i = 1, k-1 ; \quad (2.9)$$

$$\left[\frac{\rho}{\Delta t} - \theta \nabla \mu \nabla \right] (\mathbf{v}^k - \mathbf{v}^n) + \rho \mathbf{v}_a^{k-1} \cdot \nabla \mathbf{v}^{k-1} + \nabla p^n = \nabla \mu \nabla \mathbf{v}^{k-1} . \quad (2.10)$$

Here, the α^i the standard Runge-Kutta coefficients $\alpha^i = 1/(k+1-i)$. As compared to the original scheme given by Eqn. 2.4, the $k-1$ stages of Eqn. 2.9 may be seen as a predictor (or replacement) of v^n by v^{k-1} . The original right-hand side has not been modified, so that at steady-state $v^n = v^{k-1}$, preserving the requirement that the steady-state be independent of the time-step Δt . The factor γ denotes the local ratio of the stability limit for explicit time-stepping for the viscous terms versus the time-step chosen. Given that the advective and viscous time-step limits are proportional to:

$$\Delta t_a \approx \frac{h}{|\mathbf{v}|} ; \quad \Delta t_v \approx \frac{\rho h^2}{\mu} , \quad (2.11)$$

we immediately obtain

$$\gamma = \frac{\Delta t_v}{\Delta t_a} \approx \frac{\rho |\mathbf{v}| h}{\mu} \approx Re_h , \quad (2.12)$$

or, in its final form:

$$\gamma = \min(1, Re_h) . \quad (2.13)$$

In regions away from boundary layers, this factor is $O(1)$, implying that a high-order Runge-Kutta scheme is recovered. Conversely, for regions where $Re_h = O(0)$, the scheme

reverts back to the original one (Eqn. 2.4). Projection schemes of this kind (explicit advection with a variety of schemes, implicit diffusion, pressure-Poisson equation for either the pressure or pressure increments) have been widely used in conjunction with spatial discretization based on finite differences (e.g., Kim and Moin, 1985 [56]; Gresho et al., 1982 [57]; Bell and Marcus, 1992 [58]; Alessandrini and Delhommeau, 1996 [59]), finite volumes (e.g., Kallinderis and Chen, 1996 [60]), and finite elements (e.g., Gresho et al., 1982 [57]; Donea et al., 1982 [61]; Gresho and Chan, 1990 [62]; Löhner, 1990 [63]; Martin and Löhner, 1992 [64]; Ramamurti and Löhner, 1996 [65]; Takamura et al., 2001 [66]; Eaton, 2001 [67]; Löhner, 2004 [52]).

One complete time-step is then composed of the following substeps:

- Predict velocity (advective-diffusive predictor, Eqns. 2.4, 2.9, 2.10);
- Extrapolate the pressure (imposition of boundary conditions);
- Update the pressure (Eqn.2.7);
- Correct the velocity field (Eqn.2.8);
- Extrapolate the velocity field; and
- Update the scalar interface indicator.

2.4 Spatial Discretization

As stated before, we desire a spatial discretization with unstructured grids in order to:

- Approximate arbitrary domains, and
- Perform adaptive refinement in a straightforward manner, i.e., without changes to the solver.

From a numerical point of view, the difficulties in solving Eqns. 2.1 and 2.2 are the usual ones. First-order derivatives are problematic (overshoots, oscillations, instabilities), while

second-order derivatives can be discretized by a straightforward Galerkin approximation. The advection operator will be treated first, followed by the divergence operator. Given the tetrahedral grids solvers based on edge data structures incur a much lower indirect addressing and CPU overhead than those based on element data structure [51], only the former will be considered here.

2.4.1 The advection operator

It is well known that a straightforward Galerkin approximation of the advection terms will lead to an unstable scheme (recall that on a 1-D mesh of elements with constant size, the Galerkin approximation is simply a central difference scheme). Three ways have emerged to modify (or stabilize) the Galerkin discretization of the advection terms:

- integration along characteristics;
- Taylor-Galerkin (or streamline diffusion), and
- edge-based up-winding.

Only the third option above is considered here. So the Galerkin approximation for the advection terms yields a right-hand side of the form

$$r^i = D^{ij} \mathcal{F}_{ij} = D^{ij} (\mathbf{f}_i + \mathbf{f}_j), \quad (2.14)$$

where the \mathbf{f}_i are the ‘fluxes along edges’

$$\mathbf{f}_i = S_k^{ij} \mathbf{F}_k^{ij}, \quad S_k^{ij} = \frac{d_k^{ij}}{D^{ij}}, \quad D^{ij} = \sqrt{d_k^{ij} d_k^{ij}} \quad (2.15)$$

$$\mathcal{F}_{ij} = \mathbf{f}_i + \mathbf{f}_j, \quad \mathbf{f}_i = (S_k^{ij} v_i^k) \mathbf{v}_i, \quad \mathbf{f}_j = (S_k^{ij} v_j^k) \mathbf{v}_j \quad (2.16)$$

and the edge-coefficients are based on the shape-functions N^i as follows:

$$d^{ij} = \frac{1}{2} \int_{\Omega} (N_{,k}^i N^j - N_{,k}^j N^i) d\Omega \quad (2.17)$$

A consistent numerical flux is given by

$$\mathcal{F}_{ij} = \mathbf{f}_i + \mathbf{f}_j - |v^{ij}|(\mathbf{v}_i - \mathbf{v}_j), \quad v^{ij} = \frac{1}{2} S_k^{ij} (v_i^k + v_j^k). \quad (2.18)$$

As with all other edge-based upwind fluxes, this first-order scheme can be improved by reducing the difference $\mathbf{v}_i - \mathbf{v}_j$ through (limited) extrapolation to the edge center [51]. The same scheme is used for the transport equation that describes the propagation of the VOF fraction, PC or distance to the free surface given by Eqn. 2.2.

2.4.2 The divergence operator

A persistent difficulty with incompressible flow solvers has been the derivation of a stable scheme for the divergence constraint (see, Eqn. 2.1). The stability criterion for the divergence constraint is also known as the Ladyzenskaya-Babuska-Brezzi (LBB) condition. The classic way to satisfy the LBB has been to use different functional spaces for the velocity and pressure discretization. Typically, the velocity space has to be richer, containing more degrees of freedom than the pressure space. Elements belonging to this class are the p1/p1+bubble mini-element, the p1/iso-p1 element, and the p1/p2 element. An alternative way to satisfy the LBB condition is through the use of artificial viscosities [63], stabilization or a ‘consistent numerical flux’ (more elegant terms for the same thing). The equivalency of these approaches has been repeatedly demonstrated (e.g., [51, 63]). The approach taken here is based on consistent numerical fluxes, as it fits naturally into the edge-based framework. For the divergence constraint, the Galerkin approximation along edge i, j is given

by

$$\mathcal{F}_{ij} = \mathbf{f}_i + \mathbf{f}_j, \quad \mathbf{f}_i = S_k^{ij} v_i^k, \quad \mathbf{f}_j = S_k^{ij} v_j^k \quad (2.19)$$

A consistent numerical flux may be constructed by adding pressure terms of the form:

$$\mathcal{F}_{ij} = \mathbf{f}_i + \mathbf{f}_j - |\lambda^{ij}|(p_i - p_j), \quad (2.20)$$

where the eigenvalue λ^{ij} is given by the ratio of the characteristic advective time-step of the edge δt and the characteristic advective length of the edge l :

$$\lambda^{ij} = \frac{\Delta t^{ij}}{l^{ij}}. \quad (2.21)$$

Higher-order schemes can be derived by reconstruction and limiting, or by substituting the first-order differences of the pressure with third-order differences:

$$\mathcal{F}_{ij} = \mathbf{f}_i + \mathbf{f}_j - |\lambda^{ij}| \left(p_i - p_j + \frac{l^{ij}}{2} (\nabla p_i + \nabla p_j) \right). \quad (2.22)$$

This results in a stable, low-diffusion, fourth-order damping for the divergence constraint.

2.5 Volume of Fluid Extensions

The extension of a solver for the incompressible Navier-Stokes equations to handle free surface flow via the VOF technique requires a series of extensions.

2.5.1 Extrapolation of the Pressure

The pressure in the gas region needs to be extrapolated properly in order to obtain the proper velocities in the region of the free surface. This extrapolation is performed using a three step procedure, as can be seen in Figure 2.1. In the first step, the pressures for all points in the gas region are set to (constant) values, either the atmospheric pressure or, in

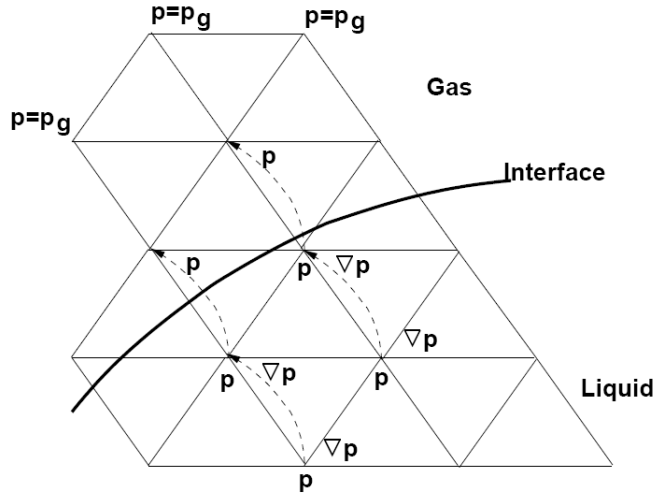


Figure 2.1: Extrapolation of the pressure

the case of bubbles, the pressure of the particular bubble. In the second step, the gradient of the pressure for the points in the liquid that are close to the liquid-gas interface are extrapolated from the points inside the liquid region. This step is required as the pressure gradient for these points can not be computed properly from the data given. Using this information (i.e., pressure and gradient of pressure), the pressure for the points in the gas that are close to the liquid-gas interface are computed.

2.5.2 Extrapolation of the Velocity

The velocity in the gas region needs to be extrapolated properly in order to propagate accurately the free surface. As shown in Figure 2.2, this extrapolation is started by initializing all velocities in the gas region to $\mathbf{v} = \mathbf{0}$. Then, for each subsequent layer of points in the gas region where velocities have not been extrapolated (unknown values), an average of the velocities of the surrounding points with known values is taken.

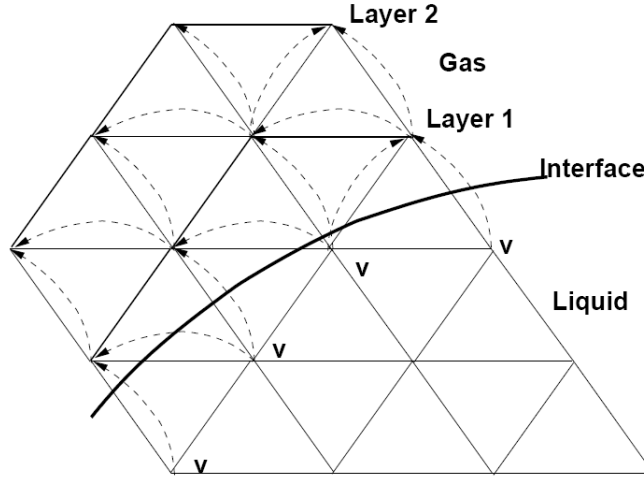


Figure 2.2: Extrapolation of the velocity

2.5.3 Imposition of Constant Mass

Experience indicates that the amount of liquid mass (as measured by the region where the VOF indicator is larger than a cut-value) does not remain constant for typical runs. The reasons for this loss or gain of mass are manifold: loss of steepness in the interface region, inexact divergence of the velocity field, boundary velocities, etc. This lack of exact conservation of liquid mass has been reported repeatedly in the literature. The recourse taken here is the classic one: add or remove mass in the interface region in order to obtain an exact conservation of mass. At the end of every time-step, the total amount of fluid mass is compared to the expected value. The expected value is determined from the mass at the previous time-step, plus the mass-flux across all boundaries during the time-step. The differences in expected and actual mass are typically very small, so that quick convergence is achieved by simply adding and removing mass appropriately. The amount of mass taken or added is made proportional to the absolute value of the normal velocity of the interface:

$$v_n = \left| \mathbf{v} \cdot \frac{\nabla \Phi}{|\nabla \Phi|} \right|. \quad (2.23)$$

In this way the regions with no movement of the interface remain unaffected by the changes made to the interface in order to impose strict conservation of mass.

2.5.4 Deactivation of Air Region

Given that the air region is neither treated nor updated, any CPU spent on it may be considered wasted. Most of the work is spent in loops over the edges (upwind solvers, limiters, gradients, etc.). Given that edges have to be grouped in order to avoid memory contention or allow vectorization when forming right-hand sides (Löhner, 1993 [68]), this opens a natural way of avoiding unnecessary work: form relatively small edge-groups that still allow for efficient vectorization, and deactivate groups instead of individual edges (Löhner, 2001 [69]). In this way, the basic loops over edges do not require any changes. The `if`-test whether an edge group is active or inactive occurs outside the inner loops over edges, leaving them unaffected. On scalar processors, edges-groups as small as `ngrp=8` are used. Furthermore, if points and edges are grouped together in such a way that proximity in memory mirrors spatial proximity, most of the edges in air will not incur any CPU penalty.

2.6 Rigid Body Motion and Mesh Movement

Each ship is treated as a rigid body, and the flow solution is obtained in an ALE frame. The rigid body motion problem is solved in a body-fixed reference frame, where the origin is located at the center of the mass. According to kinematics, the general motion of a rigid body can be decomposed into a translational motion and a rotational motion. In the dissertation, the velocity of any point on a rigid body is equal to the the velocity of the ship mass center plus the velocity due to the rotation about the body-fixed reference frame. During each time-step, the hydrodynamic forces on the body are computed based on the current flow field solution, the mooring forces are computed from a simple elastic cable model described in the next subsection, and the contact forces are evaluated when the contact between ships or between ship and the wall occurs. The position of the ship(s)

is updated based upon the solution of the general equations of rigid body motion (6-DOF). The flow solution is then updated, and so are the hydrodynamic forces, mooring forces, and contact forces on the body.

A fixed grid is used, which covers the space occupied by both the water and the air phase. Since the grid does not follow the deformation of the free surface, the grid movement is only necessary for the elements close to the ‘wavemaker plane’ and the ship. The mesh at the ‘wavemaker plane’ is moved using a sinusoidal excitation. The ship is treated as a free, floating object subject to the hydrodynamic forces of the water and mooring tensions. The surface nodes of the ship move according to a 6-DOF integration of the rigid body motion equations. Approximately thirty layers of elements close to the ‘wavemaker plane’ and the ship are moved, and the Navier-Stokes/VOF equations are integrated using an ALE frame of reference.

2.7 A Simple Mooring Cable Model

As the first step toward a comprehensive finite element modeling of the mooring cables, a simple mooring constrain system is first introduced. The resulting mooring forces are incorporated into the the general equations of rigid body motion (6-DOF). The mooring cable is modeled as an elastic cable. The resulting tension forces are evaluated according to the location of the ship and the mooring application points. For the given stiffness k and the distance between two mooring application points, the tension force \mathbf{F}_T can be expressed as:

$$\mathbf{F}_T = k\Delta\mathbf{L} , \quad (2.24)$$

where,

$$\Delta\mathbf{L} = (|\mathbf{L}| - L_0) \frac{\mathbf{L}}{|\mathbf{L}|} , \text{ for } |\mathbf{L}| > L_0, \quad (2.25)$$

and

$$\mathbf{L} = \mathbf{x}_2 - \mathbf{x}_1 . \quad (2.26)$$

Here k denotes the stiffness of the cable, L_0 the original length of the cable, and \mathbf{x}_1 and \mathbf{x}_2 coordinates of two ends of the cable line, respectively. In particular, \mathbf{F}_T is set to $\mathbf{0}$ when $|\mathbf{L}| < L_0$.

For each time-step, the distance between two mooring application points can be evaluated in terms of the ship position. The mooring tension force can then be computed and added to the general equations of rigid body motion (6-DOF). A new ship position can be obtained and the new flow field can then be computed.

2.8 Wavemaker

In the present numerical seakeeping tank, the wave is generated in the same way as in the physical tank. In particular, for either piston-type wavemaker or flap-type wavemaker, a movable paddle is placed at the upstream end of the numerical seakeeping tank, and waves are generated by given oscillations of the paddle.

To generate desired waves, the oscillation of the wavemaker paddle is given by referring to the first-order wave theory as follows (see [70, 71]):

for flap-type wavemaker,

$$\frac{H}{S} = 4 \left(\frac{\sinh kh}{kh} \right) \frac{kh \sinh kh - \cosh kh + 1}{\sinh 2kh + 2kh}; \quad (2.27)$$

for piston-type wavemaker,

$$\frac{H}{S} = \frac{2(\cosh 2kh - 1)}{\sinh 2kh + 2kh}, \quad (2.28)$$

where H denotes the wave height, S the stroke of the wavemaker, k wave number, and h water depth.

Chapter 3: Validations

3.1 Introduction

In this chapter, validations of the numerical seakeeping tank based on the numerical methods in last chapter are performed. Specially, the free surface flow solver presented in last chapter has been validated in dam-breaking problem (Löhner et al. [72]) and sloshing problem (Yang and Löhner [46]).

Focusing on the green water problem, the numerical seakeeping tank is first used to perform a validation with a simplified model test of the green water overtopping a fixed deck. Then it is further validated on a more complicated 3-D case in this chapter – green water on the deck of an FPSO model. Comparisons between numerical results and experimental measurements show a fairly good agreement in both cases.

Mooring constraints, however, are not considered in either of these two green water problems. Therefore, the problem of two side-by-side moored boxes in extreme waver is simulated in order to validate the simple mooring code of the present numerical seakeeping tank. Reliable results are presented and discussed.

3.2 Green Water Overtopping a Fixed Deck

3.2.1 Setup

The green water overtopping a fixed deck problem was first investigated experimentally by Cox and Ortega [10]. To simplify the overtopping process and measurement techniques, the experiment was conducted in a narrow wave flume at Texas A&M University, restricting the study to two dimensions. As shown schematically in Figure 3.1, the similar setup is applied in this numerical study, where x is the horizontal coordinate, positive in the direction of

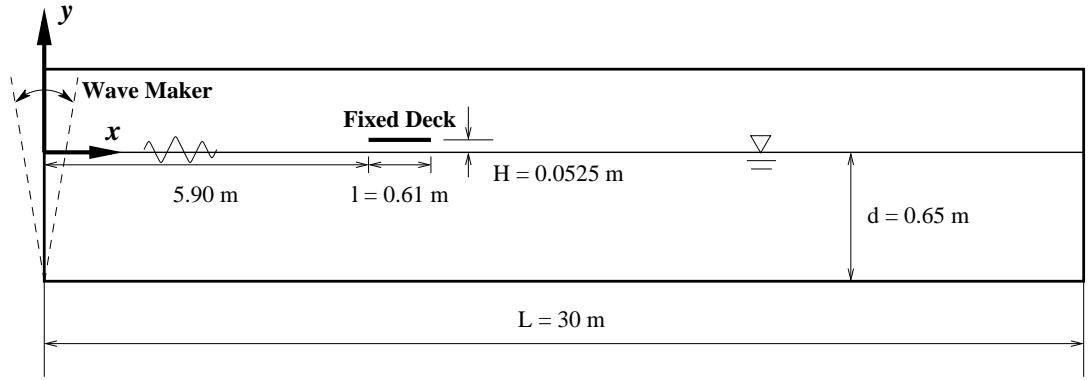


Figure 3.1: Definition sketch of green water overtopping problem

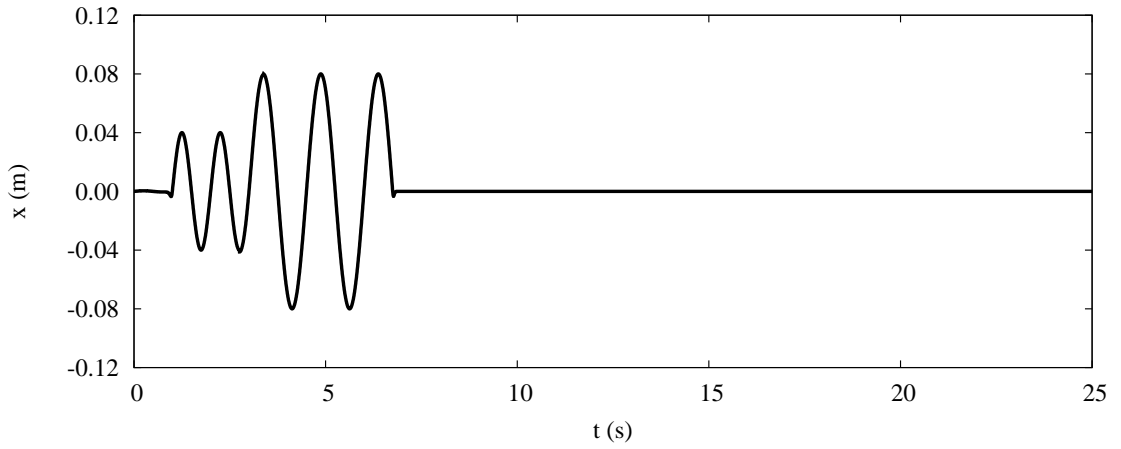


Figure 3.2: Wavemaker displacement in x direction

wave propagation with $x = 0 \text{ m}$ at the left end, and y is the vertical coordinate, positive upward with $y = 0 \text{ m}$ at the initial free surface. The numerical wave tank shown in Figure 3.1 is 30 m long and 0.65 m deep. Two cases are carried out using the same tank: one is the wave tank with a fixed deck, and the other without the fixed deck. The fixed deck is 61 cm long and just 1.15 cm thick; it sits at $y = 5.25 \text{ cm}$, i.e., the height from the initial free surface to the bottom of the deck.

A flap-type wavemaker located at the left end in the figure above is used to generate a transient wave. Specially, in order to model freak waves observed in the laboratory or nature, the transient wave is chosen in such a way that it produced one large overtopping wave at the leading edge of the deck. As shown in Figure 3.2, the wavemaker signal comprises two cycles of a sinusoidal wave with period $T_1 = 1.0 \text{ s}$, and two and a half cycles of a sinusoidal

wave with period $T_2 = 1.5$ s and larger amplitude. Table 3.1 shows the following excitation periods and amplitudes considered in our simulation.

	units	Wave 1	Wave 2
period	sec	1.0	1.5
displacement	m	0.04	0.08
cycles	-	2	2.5

It should be noted that, due to the lack of complete experimental data, the amplitudes of the wavemaker signal in the numerical simulations are based on several trials prior to the final run. Furthermore, to prevent sharp changes between two different sinusoidal waves, a smooth function is considered for the wave input (Gomez-Gesteira et al. 2005 [73]). The details are specified as follows:

(1) for $t_0 < t < t_1$,

$$x = A_1 \sin(\omega_1 t), \quad (3.1)$$

where $t_0 = 1.0$ sec is the start time, $t_1 = t_0 + 2T_1 - T_1/2$, and $\omega_1 = 2\pi/T_1$;

(2) for $t_1 < t < t_3$,

$$\alpha_1 = 0.5(-\tanh(\mu(t - t_2)) + 1) \quad (3.2a)$$

$$\alpha_2 = 0.5(\tanh(\mu(t - t_2)) + 1) \quad (3.2b)$$

$$x = \alpha_1 A_1 \sin(\omega_1 t) + \alpha_2 A_2 \sin(\omega_2(t - t_2)) \quad (3.2c)$$

where $t_2 = t_0 + 2T_1 = 3$ sec, $t_3 = t_2 + T_2/2$, α_1 and α_2 smooth coefficients, $\omega_1 = 2\pi/T_1$, and $\mu = \max\{\omega_1, \omega_2\}$;

(3) for $t_3 < t < t_4$,

$$x = A_2 \sin(\omega_2(t - t_2)), \quad (3.3)$$

where, $t_4 = t_2 + 2.5T_2$ is the end time of the transient wave.

In the end, in order to satisfy the objective of modeling the large overtopping wave on

the deck, the leading edge of the deck in our simulation is therefore adjusted to the location at $x = 5.9 \text{ m}$, compared with $x = 8.0 \text{ m}$ in the experimental measurements.

3.2.2 Results

With the given oscillatory movement of the wavemaker in Figure 3.2, the largest wave occurs at the leading edge position of the fixed deck after a few small waves pass the deck position without touching the bottom of the deck.

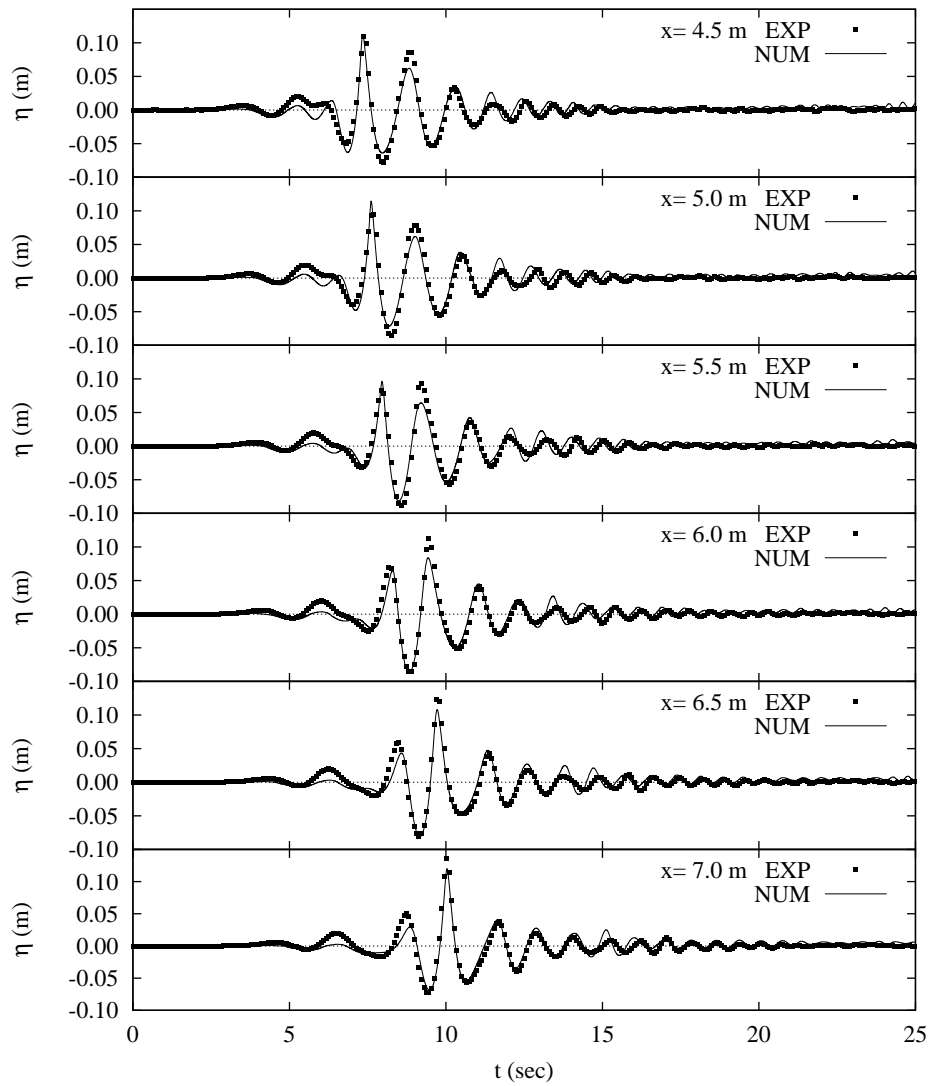


Figure 3.3: Comparison of wave elevation with experimental measurements: 1

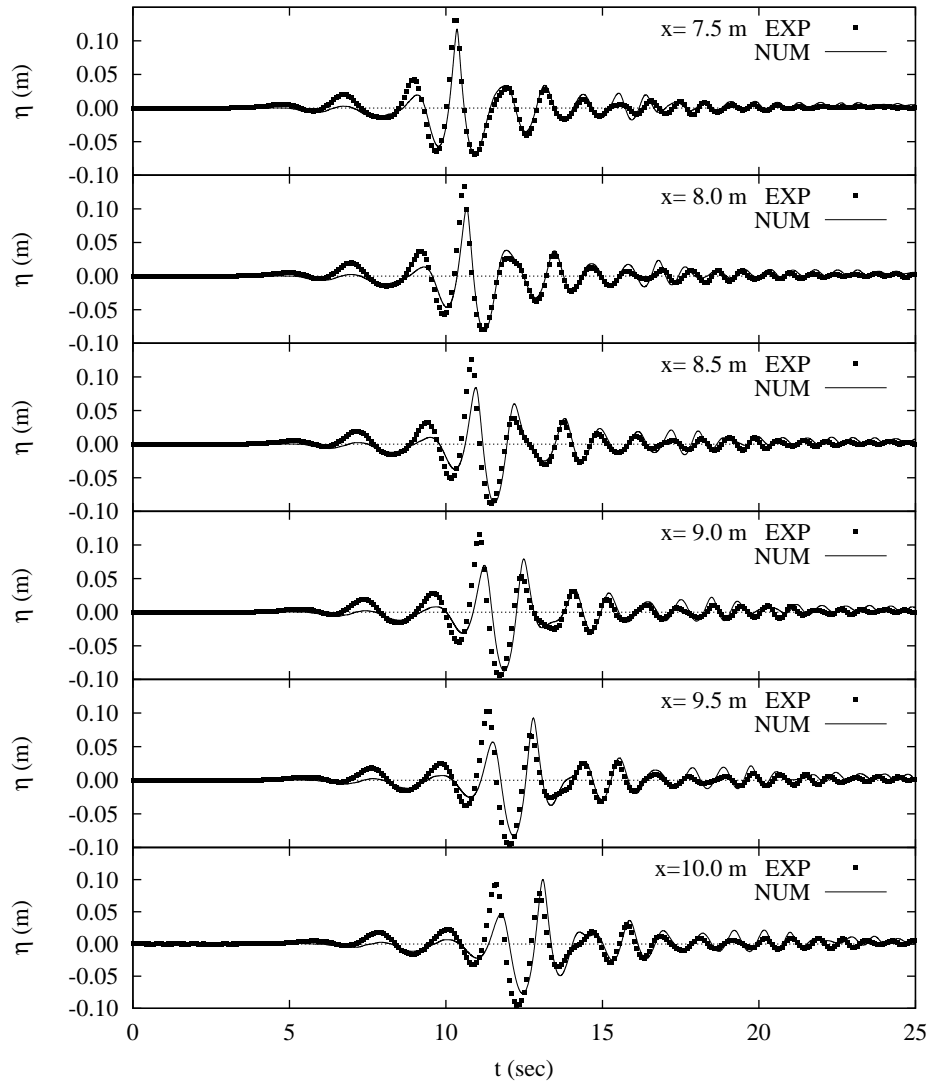


Figure 3.4: Comparison of wave elevation with experimental measurements: 2

Considering the observation that the largest wave in our simulation occurs at a different location in x -direction from experimental measurements because of the differences in wavemaker signals, we choose twelve locations by keeping the same distance of $\Delta x = 0.5 \text{ m}$ between two neighboring locations, and introduce a time shift of $\Delta t = 1.275 \text{ sec}$ in numerical results in the following comparison with experiments.

Figures 3.3 and 3.4 compare the free surface elevation between numerical results and experimental measurements at twelve different locations for the case without the deck. In these figures, the fulfilled squares denote the experimental measurements, and the solid line numerical results. It can be observed that the transient wave in our simulation exhibits the same behavior as the experiments: in the direction of wave propagation (i.e., x -direction, as from the top to the bottom in Figures 3.3 and 3.4), two large waves initially exist at the left in the wave tank, then, as approaching to the deck, gradually transform into one single and larger wave, which finally decomposes into two large waves at the right end. Thus a large wave similar to the one that overtopping the deck in experiments is successfully modeled in the present numerical wave tank. Meanwhile, it can be seen that the amplitude of the large wave in numerical simulation is slight smaller than that in experiments, and the wave patterns after $x = 9.0 \text{ m}$ in the Figure 3.4 differ to each other.

For further validation, the numerical results are compared in detail with experimental measurements in the following. Figure 3.5 compares the free surface elevations of the largest wave at the leading edge of the deck between numerical results and experimental measurements for each of the cases – without deck (depicted on the left) and with the fixed deck (depicted on the right). The dash lines indicate experimental measurements, and the solid lines numerical results. The twelve dots (i.e., $a - l$) for each case indicate twelve time instances used for velocity comparison in Figures 3.6 and 3.7. The vertical dotted lines indicate the time moment at which distribution of velocity vectors are given, as shown in Figure 3.8.

It can be seen from Figure 3.5 that the largest wave at the position of leading edge of the fix deck is modeled with a reasonable accuracy compared with experimental measurements.

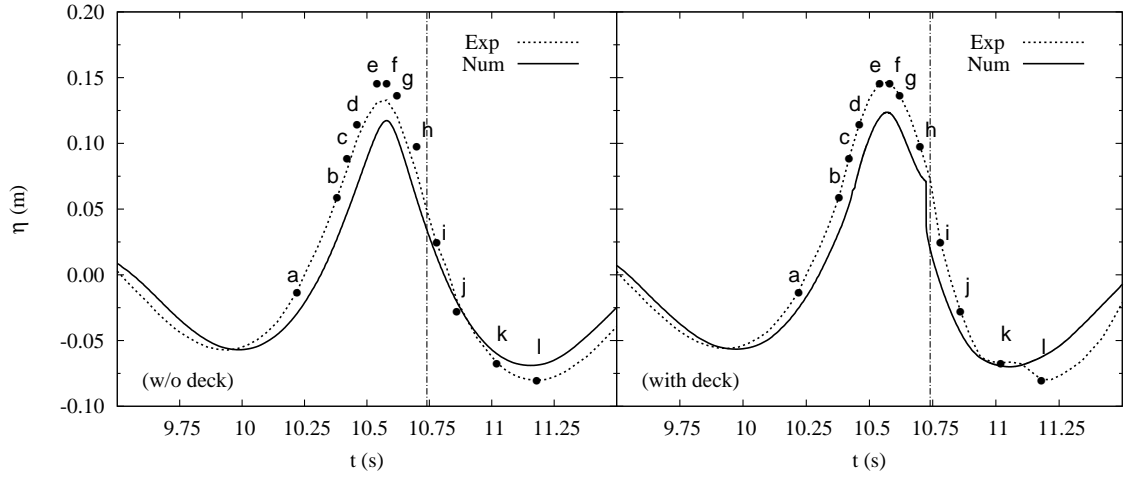


Figure 3.5: Comparison of free surface elevation at the leading edge position of the deck and twelve time instances used for velocity comparisons

It can also be observed that the effect of the deck is captured with a reasonable accuracy as well; the wave elevation for the case with deck is considerably larger than that for the case without deck.

Figures 3.6 and 3.7 show the detailed vertical variation of the horizontal velocity between the numerical results and experimental measurements at the twelve specified time instances, which are indicated by the dots ‘a – l’ in Figure 3.5, respectively. Figure 3.6 compares the results of the case without deck, and Figure 3.7 the results of the case with the fixed deck. In each figure, the solid lines denote the numerical results, the dots the experimental measurements, and the horizontal double dotted line the height of the deck structure. It can be seen from Figures 3.6 and 3.7 that the simulation results are in fairly good agreement with experimental measurements for the case with or without the fixed deck. In addition, the pattern in Figure 3.7 clearly shows the separation of the water due to the existence of deck.

Figure 3.8 shows vertical distribution of velocity vectors in front of the deck. The comparison for the case without the fixed deck is given on the left, and the comparison for the case with deck is given on the right. The red lines indicate the experimental measurements at $t = 10.74$ s at various positions along the vertical direction; the blue lines indicate the numerical results at $t = 9.215$ s at the same positions as those in experiments. Compared

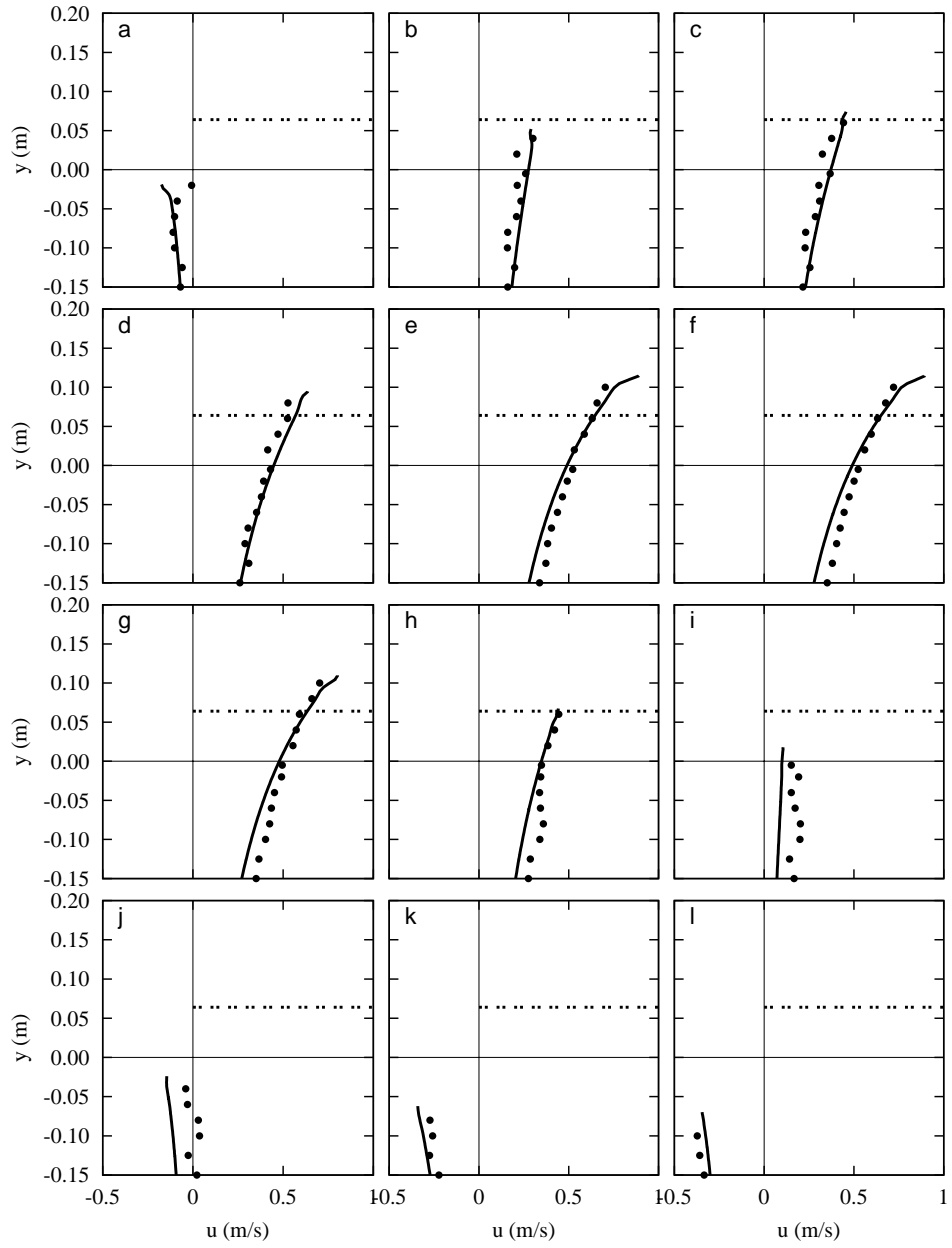


Figure 3.6: Comparison of vertical variation of horizontal velocity u (m/s) for the case without the fixed deck

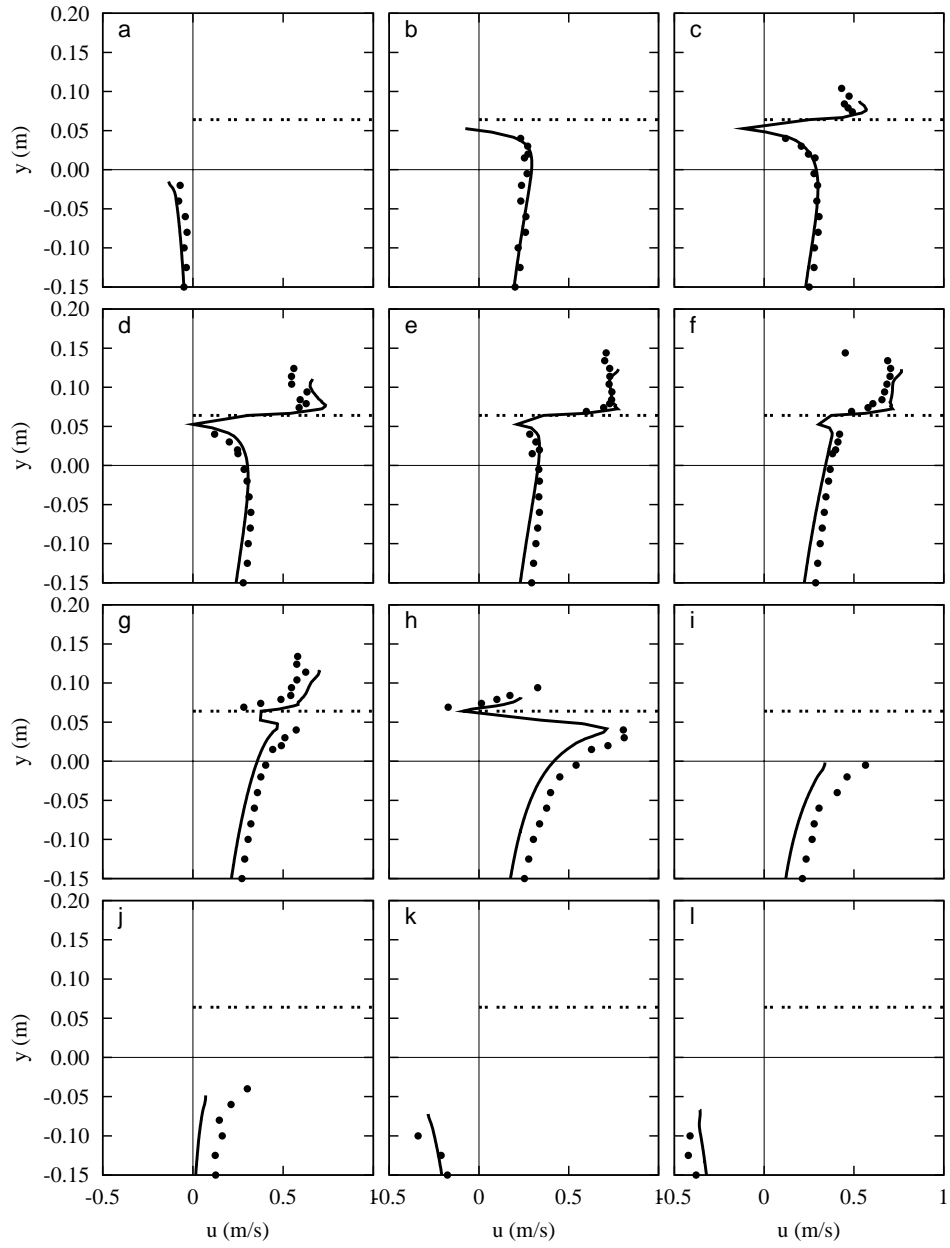


Figure 3.7: Comparison of vertical variation of horizontal velocity u (m/s) for the case with the fixed deck

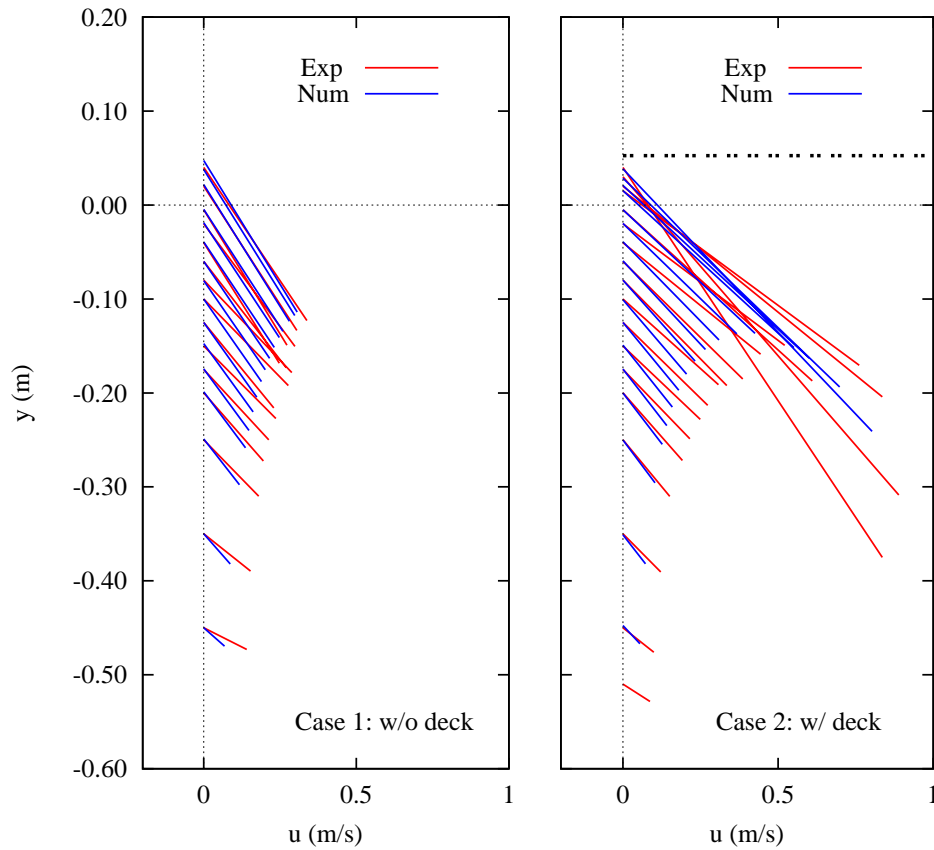


Figure 3.8: Comparison of vertical distribution of velocity vector at the leading edge position of the fixed deck

with experimental results, the similar distribution of velocity vectors can be observed in numerical results. Specially for the case with the fixed deck, the similar transition of velocity with significantly larger magnitude can be observed at the position close to bottom of the deck. This again demonstrates that the present numerical model and computer code can be used to simulate highly nonlinear waves and wave-body interactions.

Figure 3.9 briefly shows that a large wave approaches, separates, and passes by the fixed deck. The observation of the wave separation in front of the fixed deck and green water overtopping the deck demonstrates that this numerical tool can capture the highly nonlinear free surface accurately.

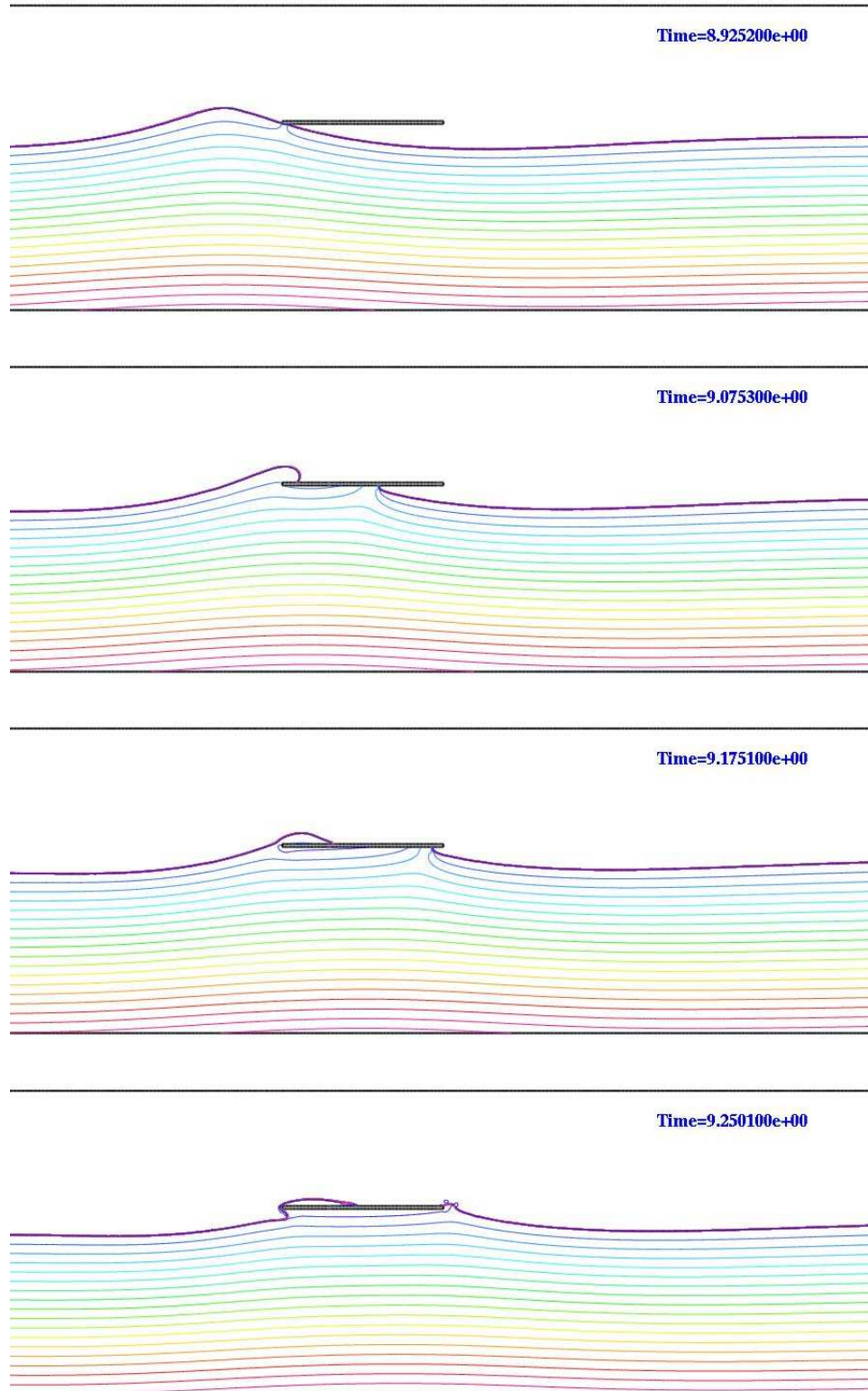


Figure 3.9: Snapshots of green water overtopping a fixed deck

3.3 Green Water on the Deck of an FPSO Model

This numerical seakeeping tank is also validated by investigating the green water on the deck of an FPSO model in extreme head waves. The model test of this problem was carried out in the State Key Laboratory of Ocean Engineering at Shanghai Jiao Tong University [12]. Table 3.2 gives the main dimensions of the full size FPSO, as well as that of the FPSO model with an 1:64 scale. Specially, a box-like deckhouse was added to the FPSO, located on the fore part of the deck, i.e., 0.36 m from the bow.

Table 3.2: Main particulars for FPSO

	units	Ship	Model
length	m	225.0	3.5156
beam	m	46.0	0.7188
depth	m	24.1	0.3766
draft	m	18.5	0.2896
displacement	t	170131.5	0.6490

3.3.1 Setup

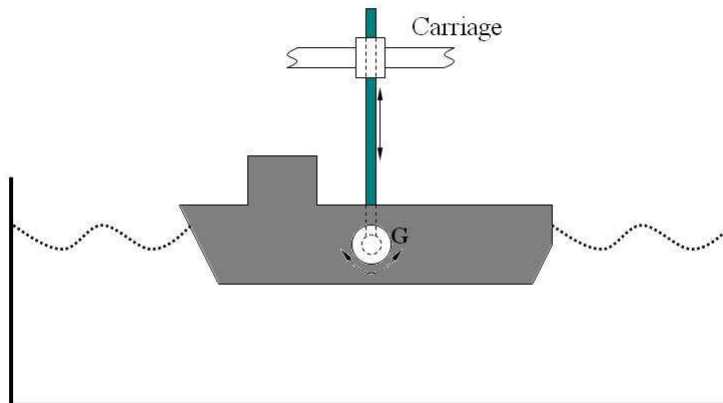


Figure 3.10: Sketch of the setup of model test

As shown in Figure 3.10, the motion of the FPSO model is restricted by attaching the model through the center of the gravity of the model to a slide rod with roller bearing. Therefore, only the heave motion and the pitch motion are allowed. This corresponds well with the real operating environment of an FPSO. The wave induced loading on deck and deckhouse in green water incidents is usually the cause of structure damages to an FPSO. To determine the pressure values on deck quantitatively, several pressure gauges were used. The pressure gages were mounted on the deck and the front wall of the deck house. The wave loading was so big that several pressure gauges were destroyed during the model test. Due to some uncertainties in the measurement of pressure, the pressure will not be discussed in this validation. On the other hand, the water height on the deck of an FPSO, resulting from green water loading, was measured using wave meters on the deck. The displacement of heave and pitch were also measured using non-contact optical motion measuring systems. Furthermore, the green water on the deck was video recorded.

Problem Definition

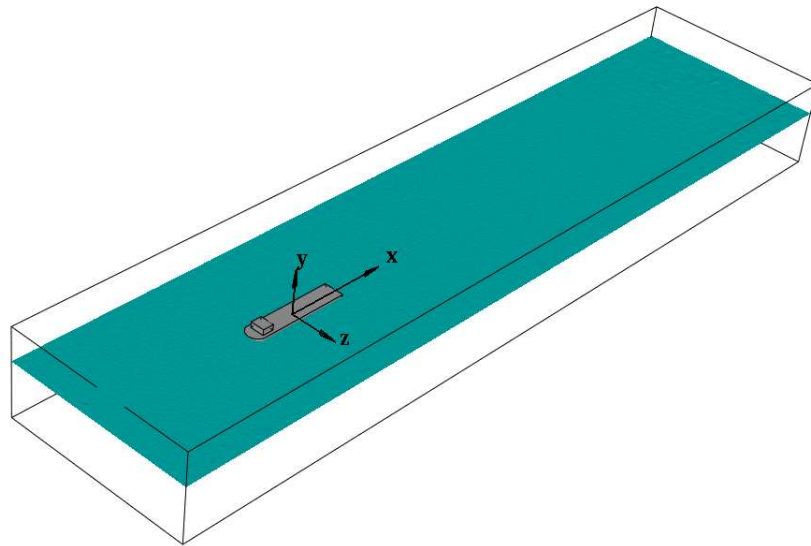


Figure 3.11: Problem definition of an FPSO in numerical seakeeping tank

The same constraint as in the model test is used in this validation: i.e., the model is free to heave and pitch in head waves. For the present head wave condition, the computational

domain consists of one half of the ship, a symmetric plane at the centerline, a piston paddle at the left wall, a side wall and a right wall at the far end downstream. Specially, the waves are generated by moving the left wall of the domain with a given sinusoidal excitation, i.e., $x = x_0 + a \sin(\omega t)$, where x_0 is the initial location of wavemaker in x -direction. The sinusoidal excitation period is defined as $T = \omega/2\pi$. The following excitation period and amplitude are considered in the numerical simulation:

$$T = 1.7 \text{ sec}, \quad a = 0.0495 \text{ m},$$

which generates a regular wave that has wave length $L = 4.48m$ and wave height $H = 0.19m$. The same type of regular wave was used in the experiment.

A large element size is specified at the far end of the domain in order to damp the waves. Figure 3.12 shows the surface grids on the body of the FPSO model and the symmetric plane of the tank: fine grids with the thickness of almost four grid layers is used on the surface of the FPSO model. The mesh has approximate `nElem = 4,995,500` elements.

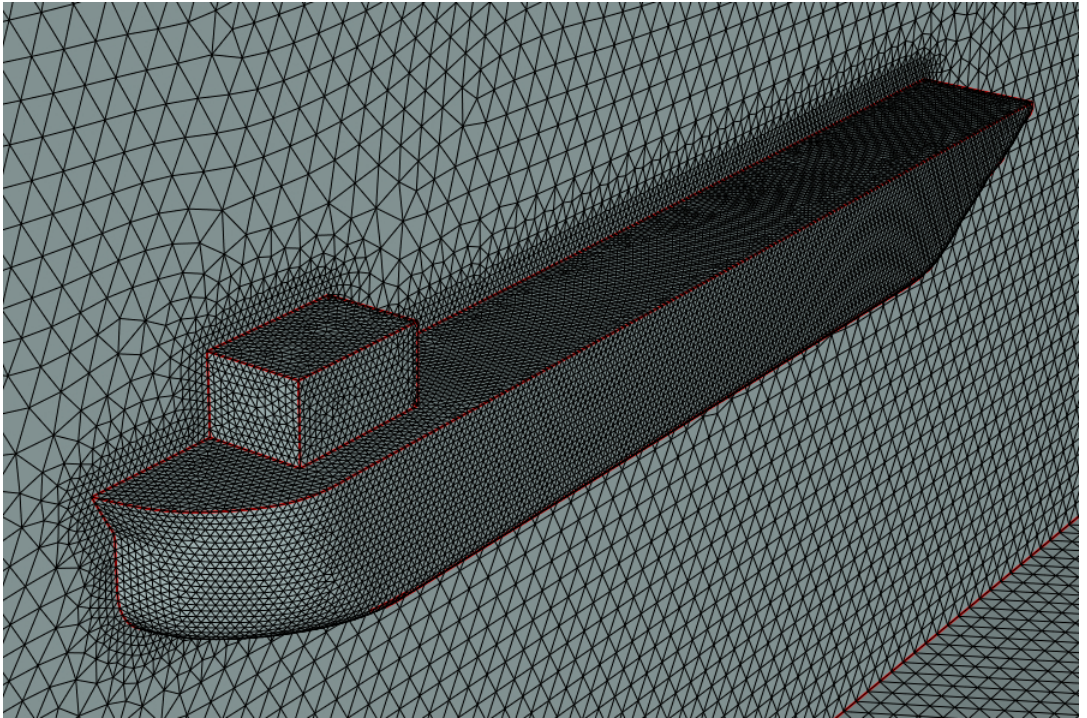


Figure 3.12: Surface grids on the FPSO model

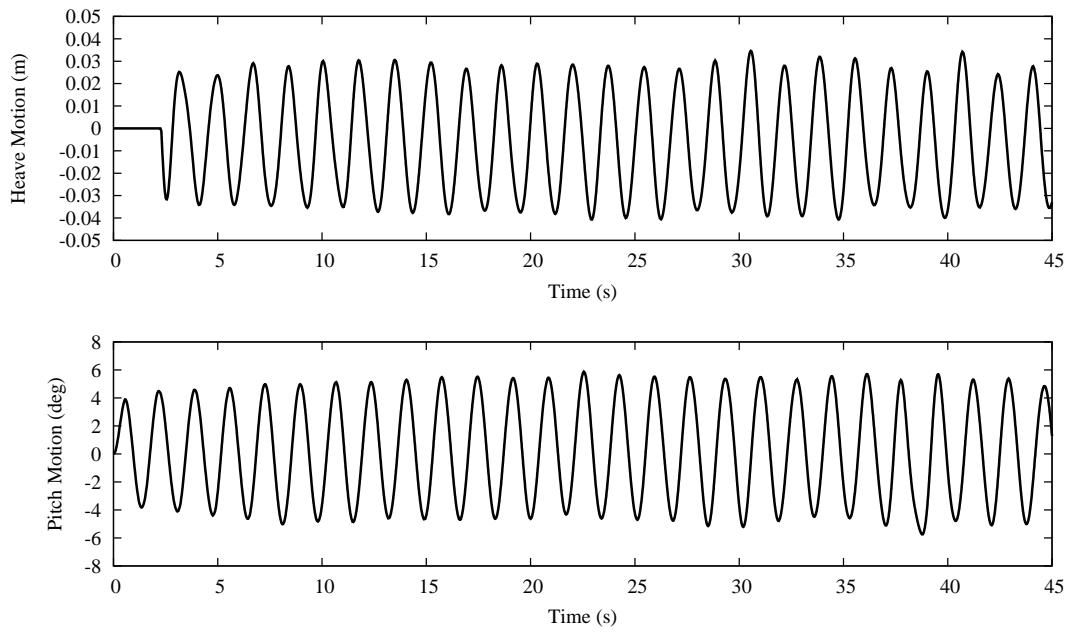


Figure 3.13: Time history of prescribed heave and pitch motions of FPSO model

In this numerical simulation, the FPSO model is moved with prescribed heave and pitch motions, as shown in Figure 3.13. These values were obtained from the experimental measurement with slight modification close to the starting time, and thus are used as the prescribed motions in this numerical simulation.

3.3.2 Results

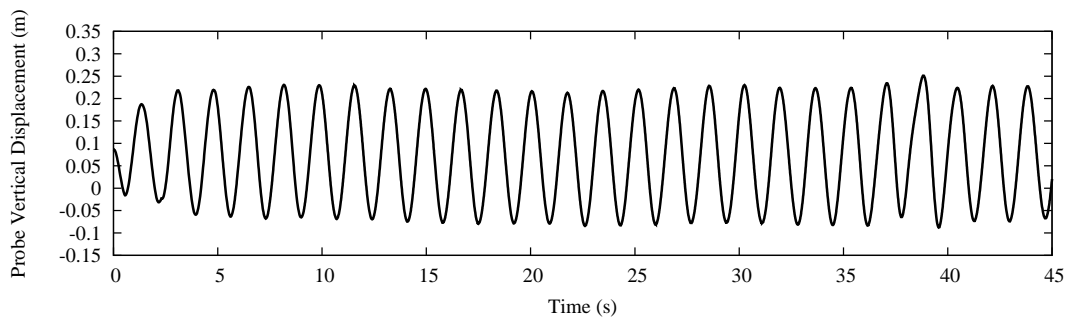


Figure 3.14: Vertical displacement of water probe on the deck

The water height on a given location on the deck in front of the deckhouse (i.e., 0.08 m from the deckhouse) is recorded. The time history of the vertical displacement of this

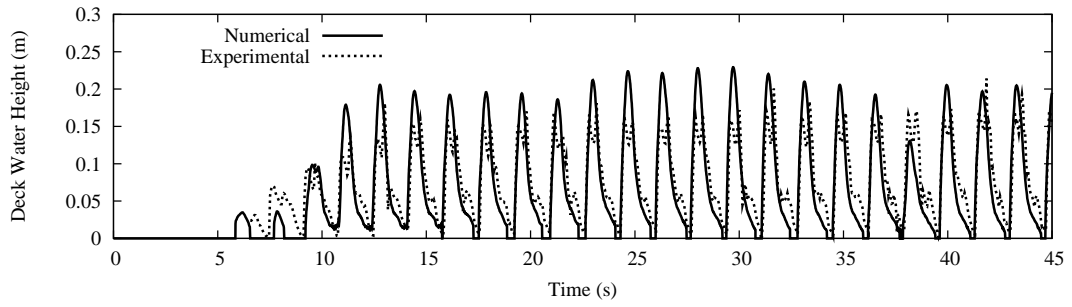


Figure 3.15: Water height on deck

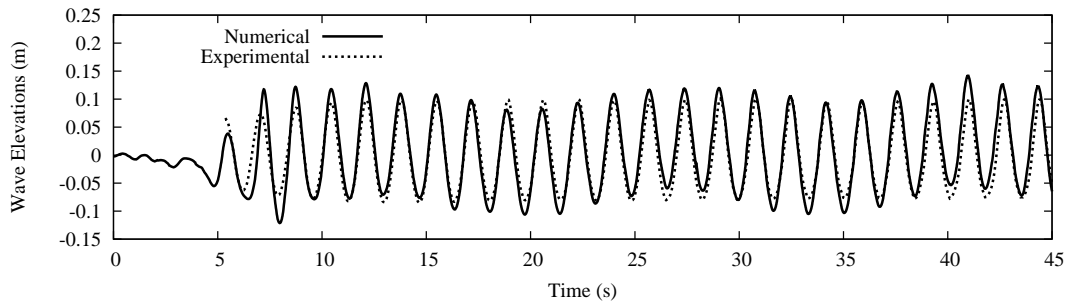


Figure 3.16: Wave elevation at a given position in front of the hull

location is shown in Figure 3.14. The comparison of the water height on the deck obtained from the numerical simulation where the hull is subject to the prescribed heave and pitch motion and that from the experimental measurement is shown in Figure 3.15.

The water height on the deck is measured with respect to the moving hull deck position. The wave elevation time history at a given location in front of the bow is also compared in Figure 3.16. It can be seen from the comparison that the wave elevation in front of the hull in numerical simulation is fairly close to the experimental results. That demonstrates that the wavemaker used in this numerical seakeeping tank works fairly well. Figures 3.17 - 3.20 show the snapshots of the free surface elevation at selected time instances. In each figure, the top shows the full view of the FPSO model sitting in extreme waves, and the bottom the close view of wave-hull interaction at the bow area. Severe green water on deck can be observed for the prescribed motion case from these figures: the similar scenario was also observed from recorded videos in experiments.

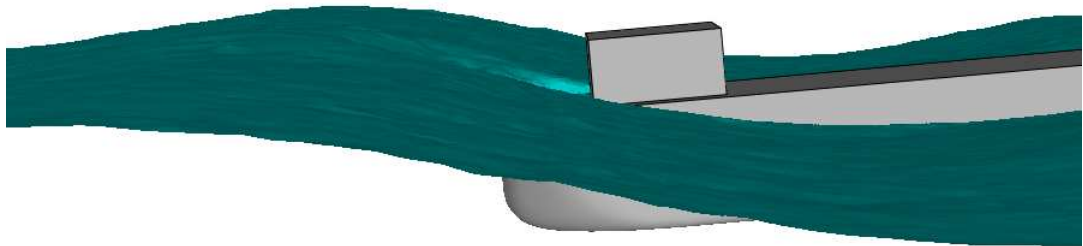
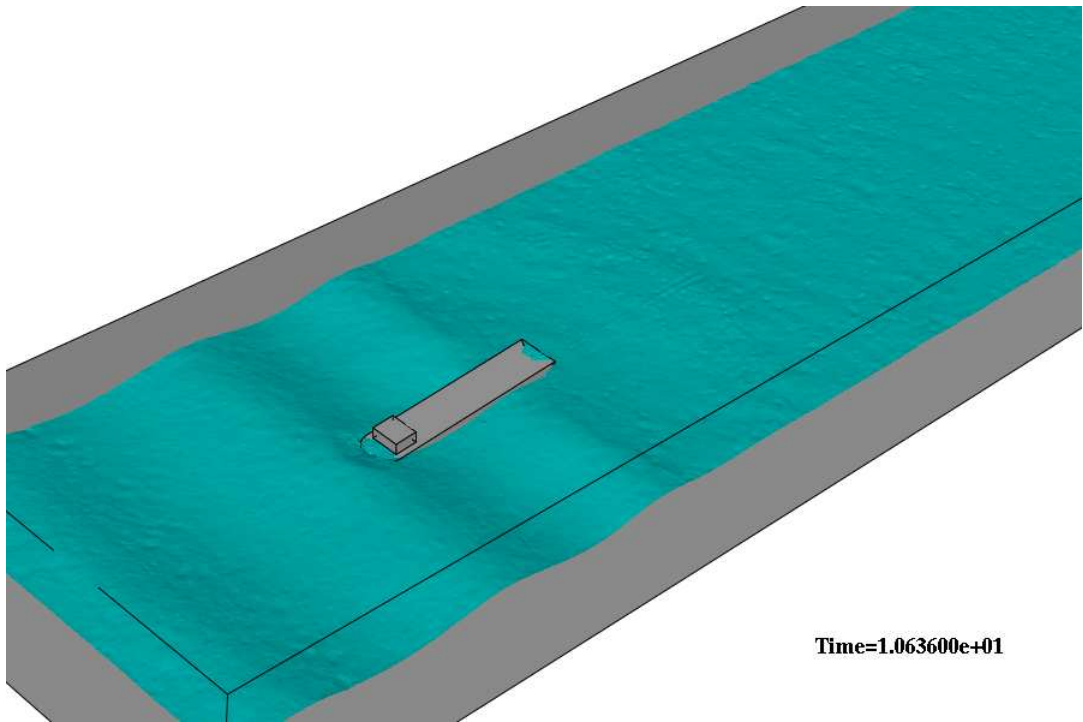


Figure 3.17: FPSO model in extreme waves (top: full view; bottom: close view): 1

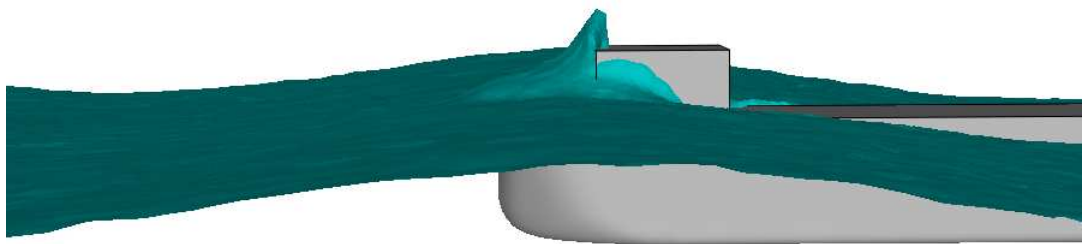
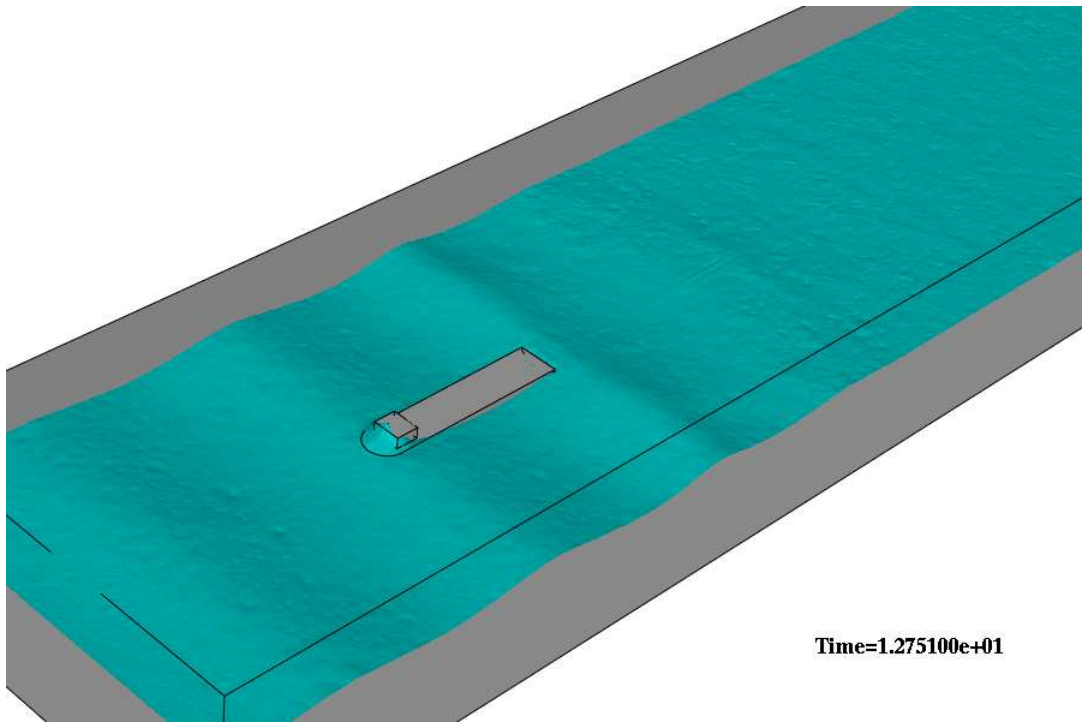


Figure 3.18: FPSO model in extreme waves (top: full view; bottom: close view): 2

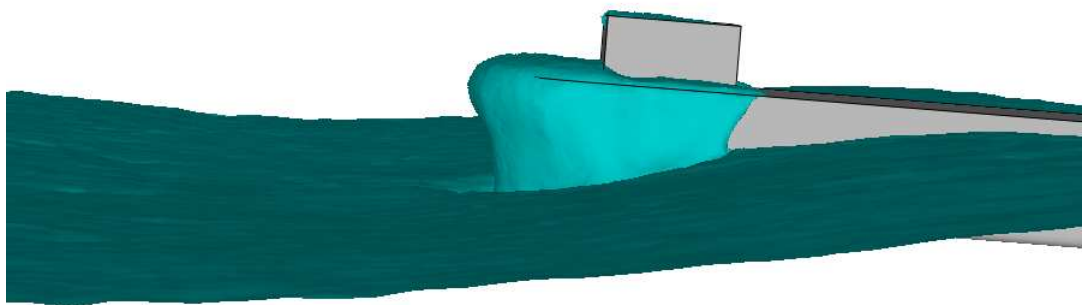
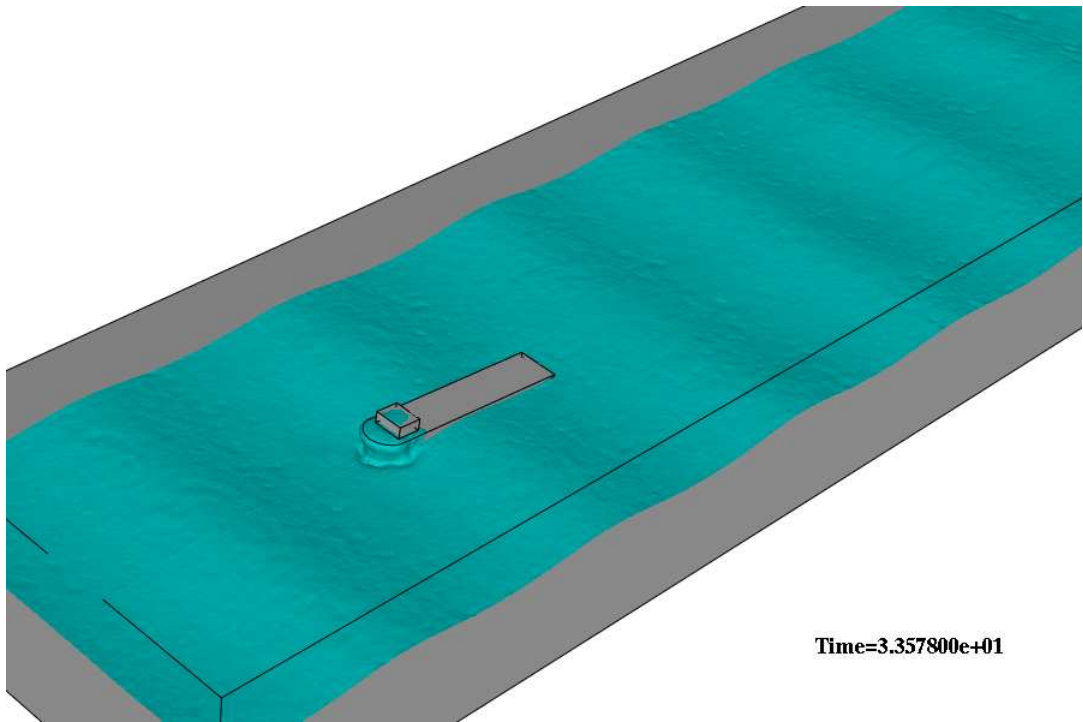


Figure 3.19: FPSO model in extreme waves (left: full view; bottom: close view): 3

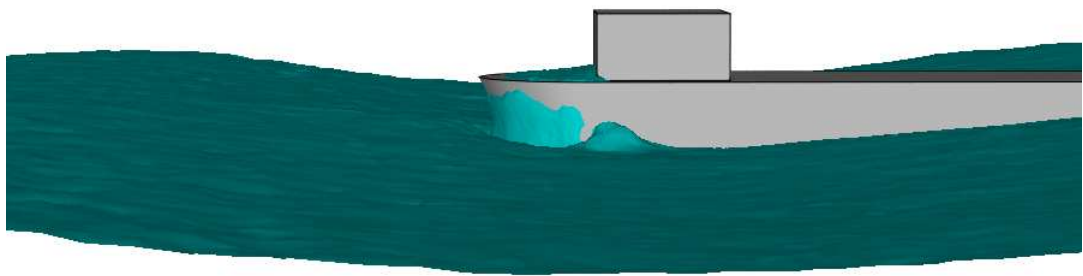
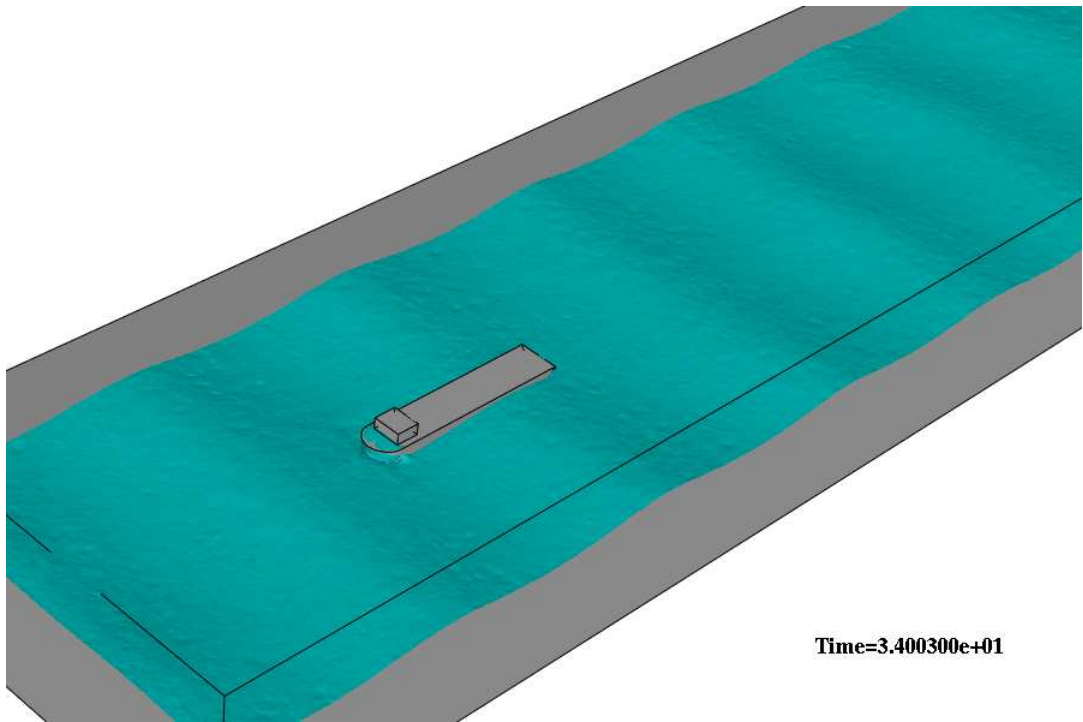


Figure 3.20: FPSO model in extreme waves (top: full view; bottom: close view): 4

3.4 Two Side-by-side Boxes Moored in Dam-breaking Waves

In order to validate the simple mooring code introduced in last chapter, a simple case is set up. As shown in Figure 3.21, two identical boxes with dimension of $2\text{m} \times 1\text{m} \times 1\text{m}$ ($L \times W \times H$) are moored side-by-side with six mooring cables in a tank.

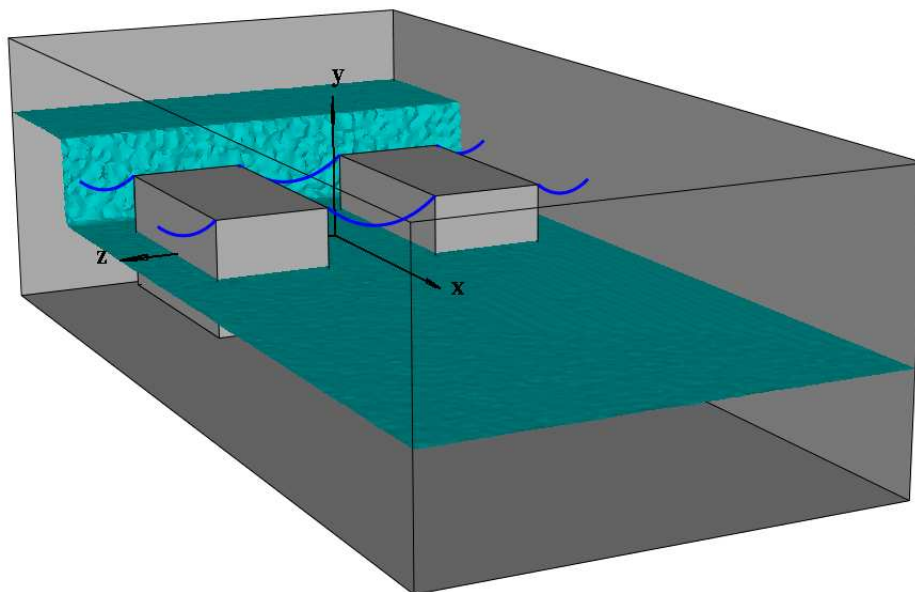


Figure 3.21: Two identical boxes moored side-by-side in dam-breaking waves

Each box is allowed to move in full 6-DOF but with the mooring constraints, and half of each box sits below the free surface at initial. A dam-breaking wave with an initial height of 0.8 m is specified as an incoming wave. As can be seen in Figure 3.22, a uniform mesh is mainly used for the whole computational domain, with relatively fine grids specified on the surface of each box. The computational domain has approximately $\text{nelem} = 1,080,500$ tetrahedral elements.

The comparison of 6-DOF motion responses of each box is plotted in Figures 3.23 and 3.24. It can be observed from Figures 3.23 and 3.24 that the magnitudes of the motion responses in full 6-DOF of Box 1 are very close to these of Box 2. It can also be observed that the directions of these motion responses of Box 1 are either the same as these of Box 2 (i.e., responses in surge, heave, and pitch motions) or opposite to these of Box 2 (i.e.,

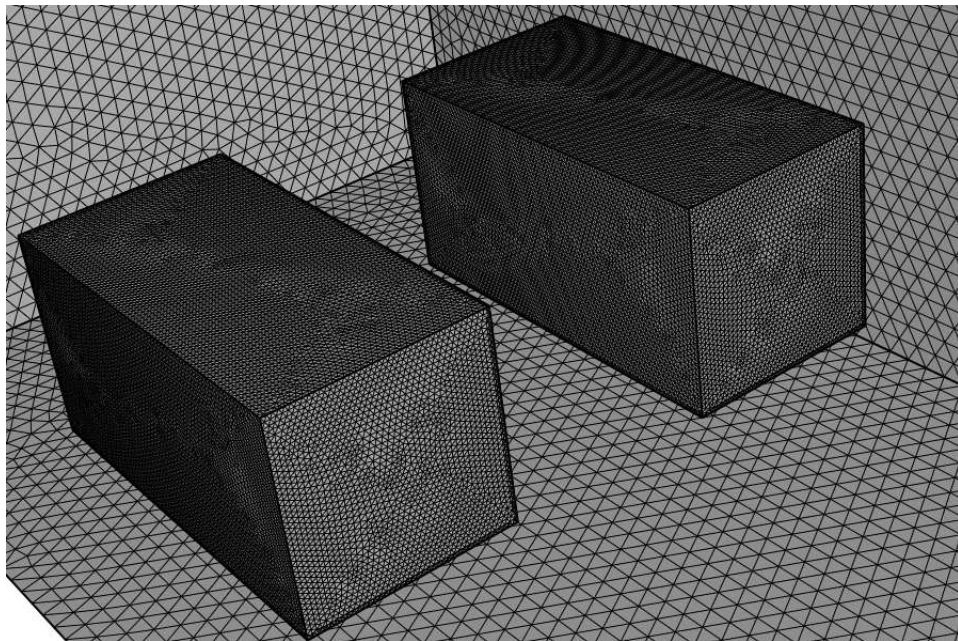
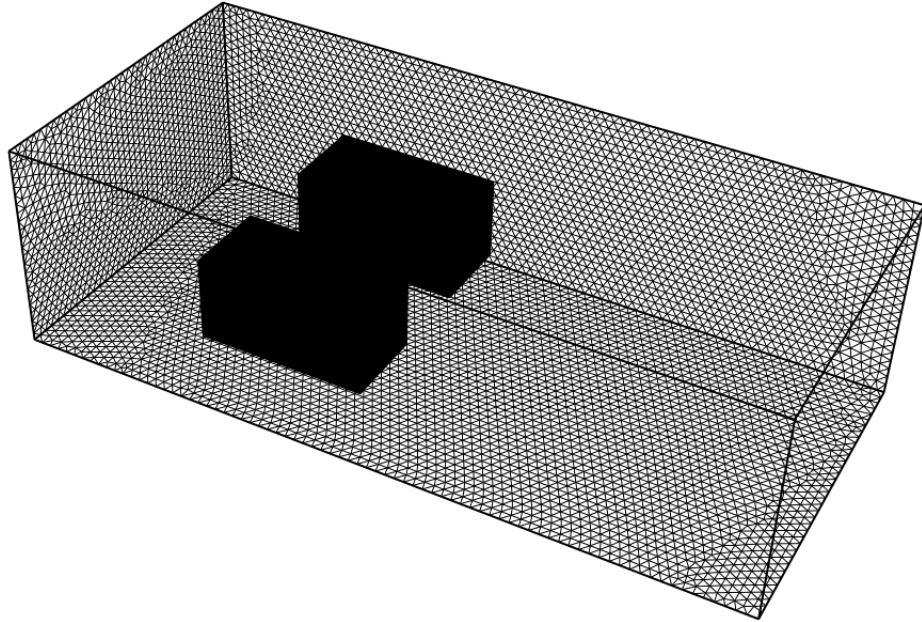


Figure 3.22: Surface grids on walls and boxes: top–full view; bottom–close view

responses in sway, roll, and yaw motions), as expected.

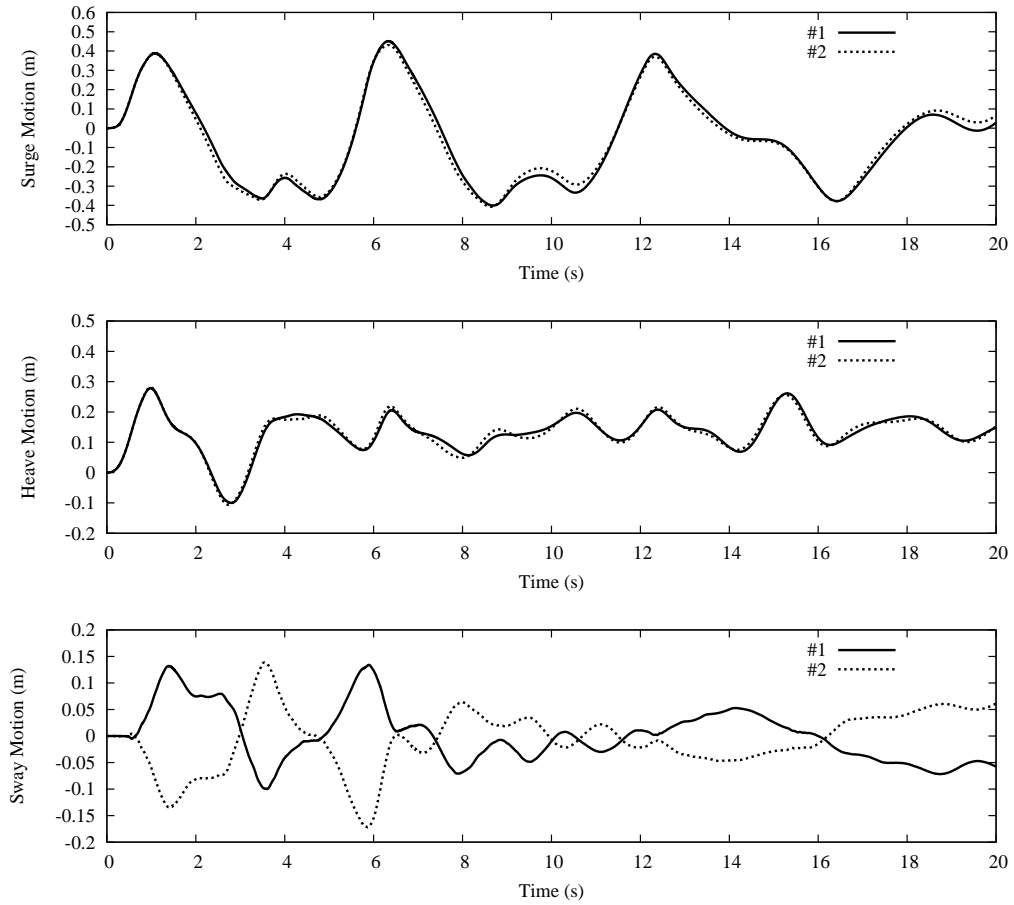


Figure 3.23: Comparison of motion responses between each box: surge, heave, and sway, respectively

Figures 3.25 and 3.26 show the snapshots of two boxes in dam-breaking waves at selected time instances. Violent free surface motion and body movements in this case are observed in these snapshots. It can also be observed that constrained with the given mooring cables, those two boxes move symmetrically in the dam-breaking waves. That can be concluded that the present simple mooring code provide reliable mooring constraints in this problem.

The results of this validation shows that the the computer code based on the coupling of the simple mooring cable model, the unstructured grid-based incompressible flow solver and the general equations of rigid body motion (6-DOF) can be used to simulate the motion responses of moored bodies in full 6-DOF in extreme waves.

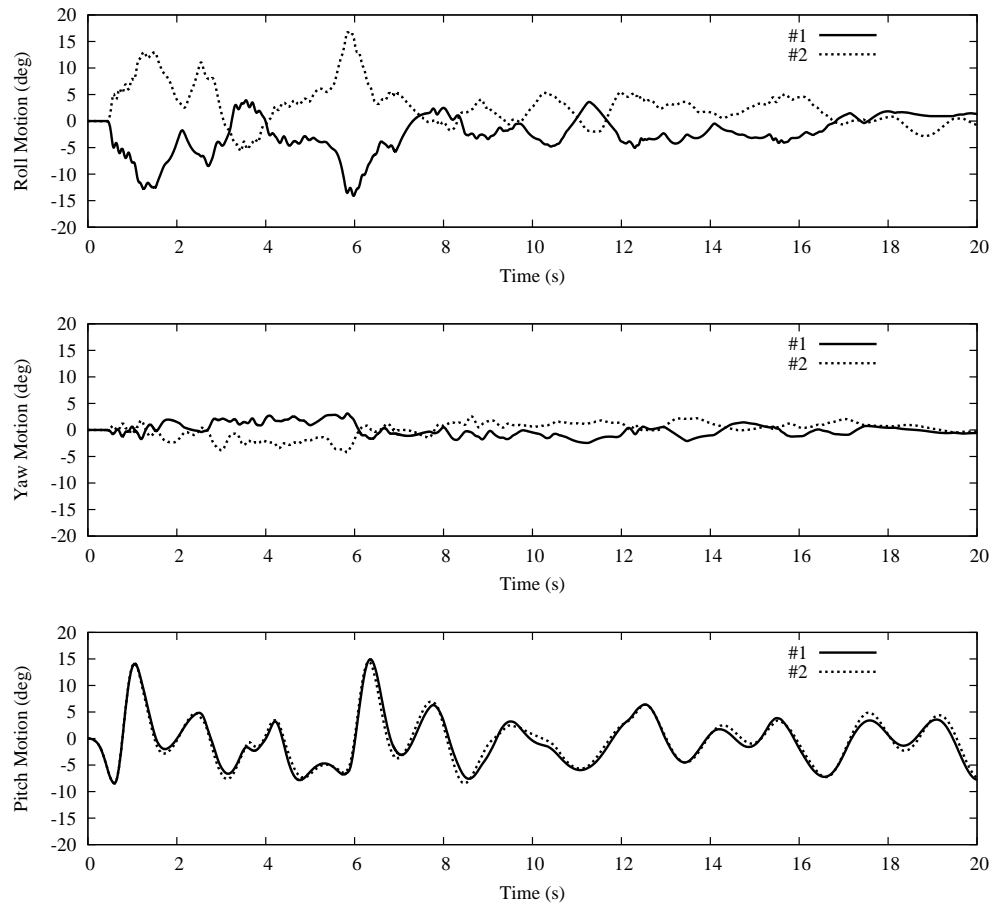


Figure 3.24: Comparison of motion responses between each box: roll, yaw, and pitch, respectively

3.5 Closure

In this chapter, the numerical method and the computer code introduced in the last chapter have been validated by investigating two green water problems: green water overtopping a fixed deck and green water on the deck of an FPSO model. The numerical results of each problem are in fairly good agreement with experimental measurements. The computer code coupled with a simple mooring cable model is also used to investigate motion responses of two side-by-side moored boxes in dam-breaking waves. The results presented in this chapter have demonstrated that the computer code introduced in last chapter could be used to simulate these complex highly nonlinear interface problems including green water on deck, wave-body hydrodynamic interactions, and mooring cable effects.

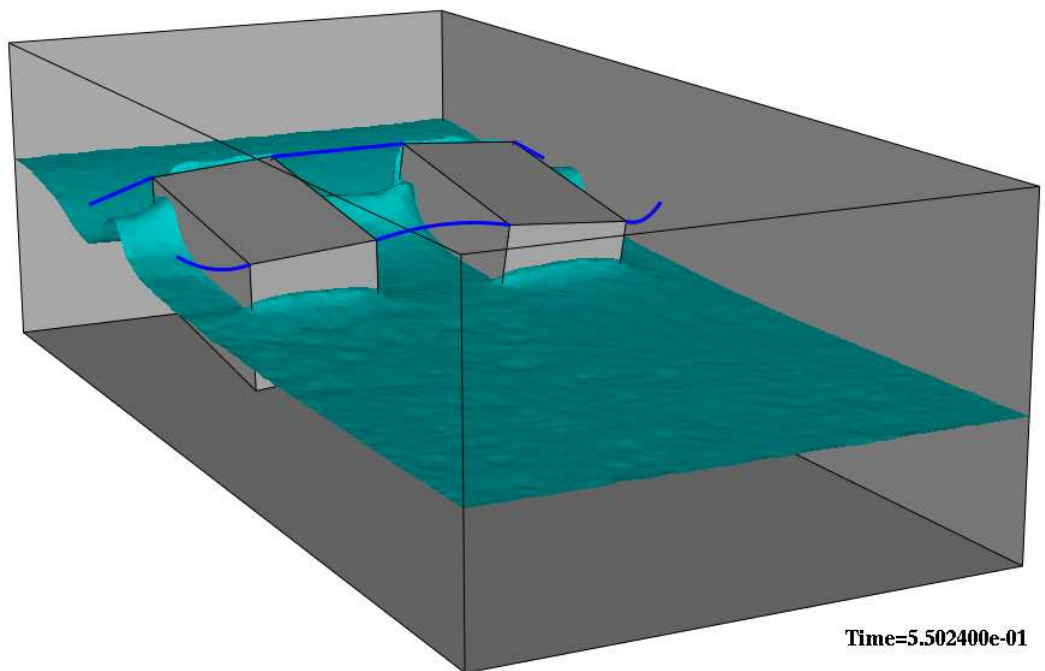
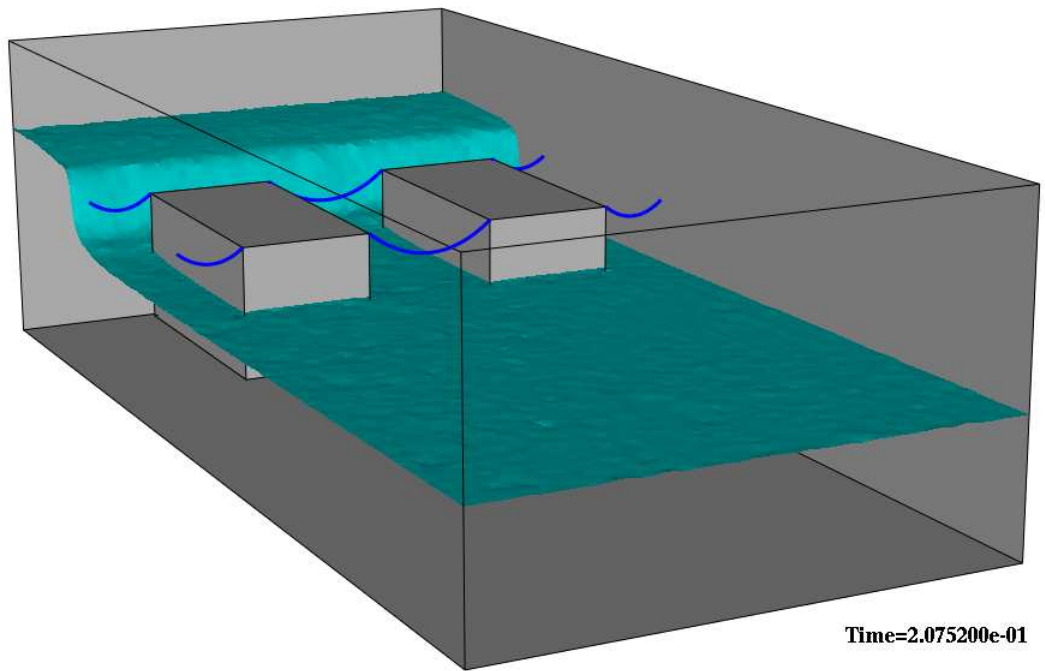


Figure 3.25: Snapshots of side-by-side moored boxes in extreme waves (1)

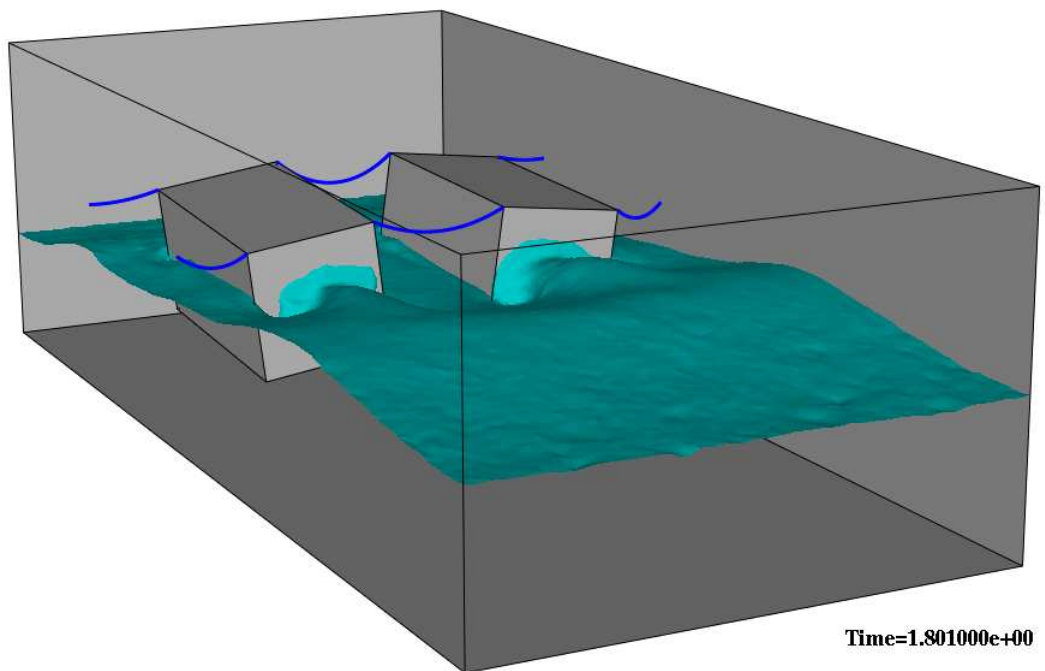
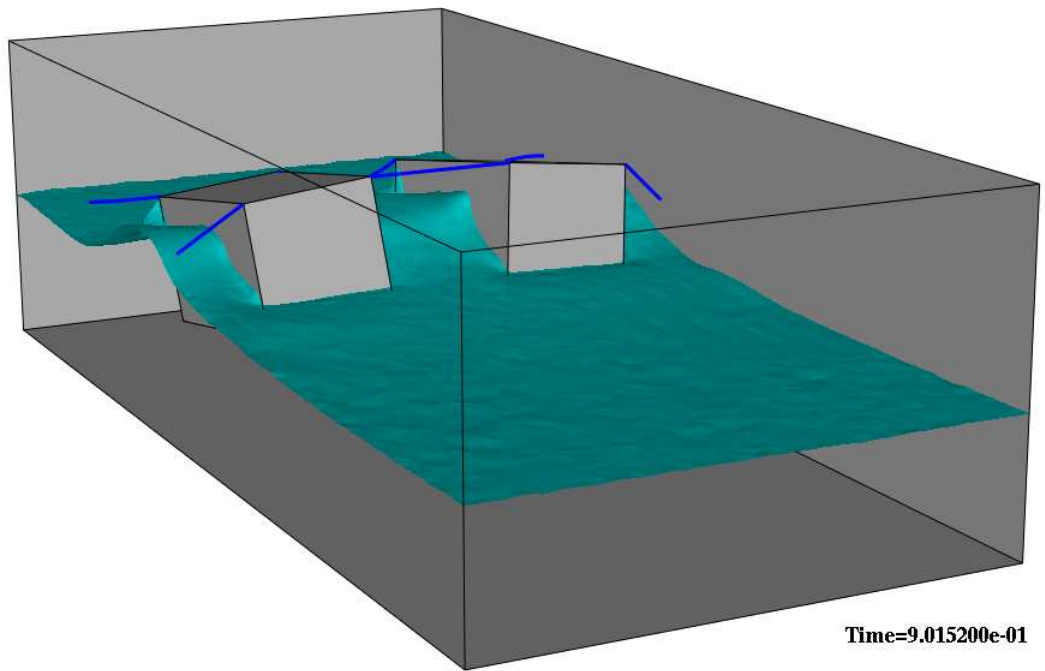


Figure 3.26: Snapshots of side-by-side moored boxes in extreme waves (2)

Chapter 4: Case Studies

4.1 Introduction

The validated numerical seakeeping tank is used to simulate motion responses of single ship or multiple vessels in extreme waves in this chapter. These common situations in offshore engineering usually consist of highly nonlinear phenomena such as ship-ship hydrodynamic interactions between two ships, green water on deck, and the effects of mooring cables.

As mentioned in previous, ships or other offshore units in rough seas are very likely to be subject to green water problem. That could cause severe damage to the hull and the superstructure of the vessel. Therefore, we first present case studies about a single FPSO model in extremes waves, including a freely moving single FPSO model in extreme waves and a single FPSO model moored by a simple spreading cable system in extreme waves.

In addition, offloading operation of oil or LNG in offshore engineering is usually performed between terminals (e.g., FPSOs) and tankers/carriers (e.g., LNGCs). That requires two vessels be moored at a limited distance to each other. Therefore, the ship-ship hydrodynamic interactions and mooring effects can not be ignored in this situation. In this chapter, two common mooring configurations in offshore engineering are applied to two vessels: i.e., an FPSO and an LNGC are either side-by-side moored or moored in tandem in extreme waves. Ship motion responses for each case are investigated and compared in detail.

An extreme regular wave is generated by a piston-type wavemaker with a given sinusoidal excitation, i.e., $x = x_0 + a \sin(\omega t)$. The sinusoidal excitation period is define as $T = \omega/2\pi$. The following excitation period and amplitude are considered:

$$T = 1.7 \text{ sec}, \quad a = 0.0495 \text{ m}.$$

That generates a wave with period $T = 1.7 \text{ sec}$, wave length $L = 4.48 \text{ m}$, and wave height $H = 0.19 \text{ m}$. The same regular wave is applied to all case studies in this chapter.

4.2 Single FPSO in Extreme Waves

The present numerical seakeeping tank is first used for further investigations of a single ship in extreme waves. The same FPSO model introduced in the validation in last chapter is used. The ship is allowed to freely move in heave and pitch motions subject to the hydrodynamic force in the same head waves. In addition, the same geometry and mesh configurations as the prescribed case is performed.

Figure 4.1 shows heave and pitch motions of each case: the solid line indicates the case of FPSO with prescribed motion; the dash line indicates the case of FPSO which is free to heave and pitch motion. It can be seen in Figure 4.1 that the freely moving FPSO is subject to large heave motion after 10 sec, and extremely larger heave motion after about 38 sec, while its pitch motion is slightly small compared with the prescribed motion.

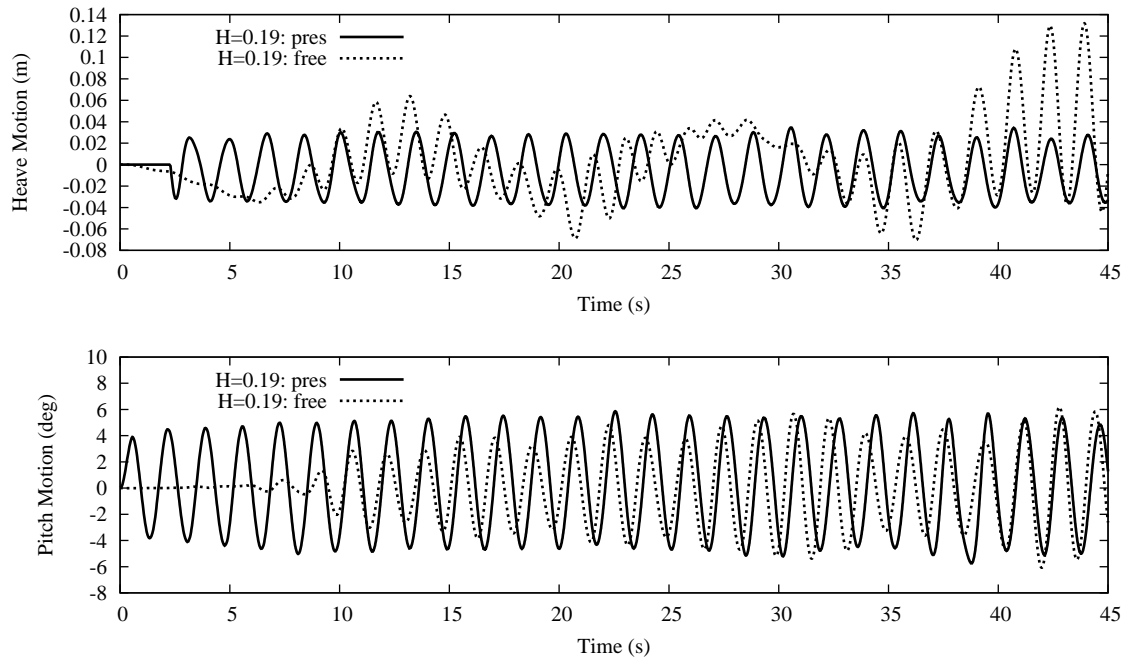


Figure 4.1: Comparison of heave and pitch motions

Figure 4.2 shows comparison of water height on deck for each case with experimental measurements. It can be seen that the predicted water height on the deck is in better agreement with experimental measurements for prescribed motion than that for the freely moving.

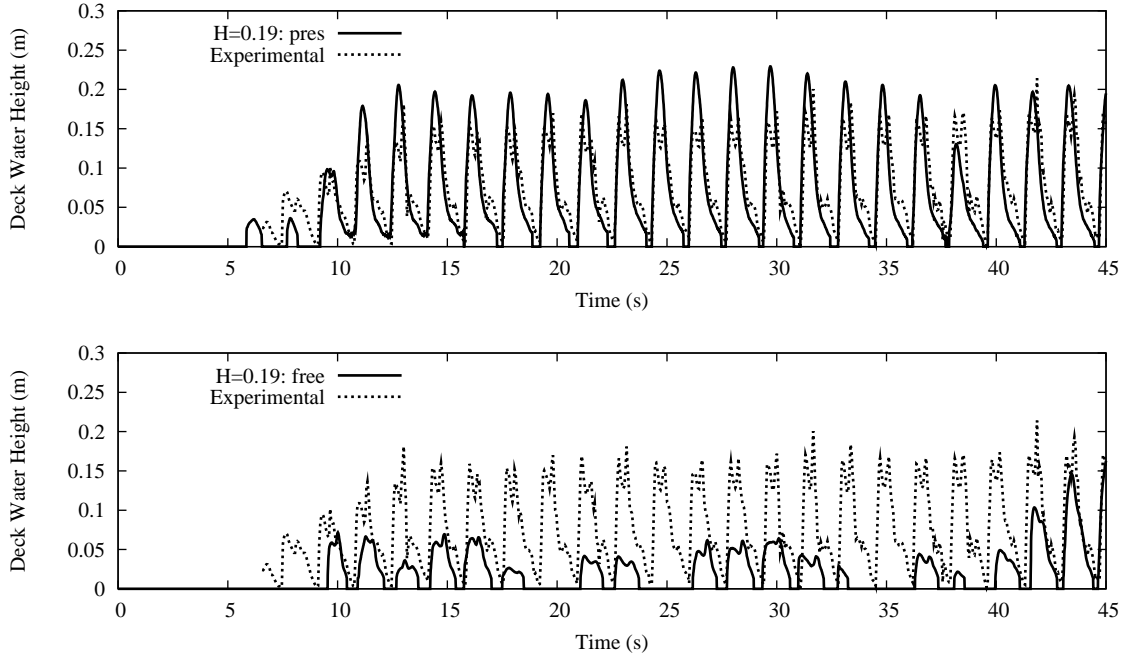


Figure 4.2: Comparison of the water height on deck

The absolute water height at the same given deck location is shown in Figure 4.3 for both prescribed motion case and freely moving case. It can be seen from Figure 4.2 and Figure 4.3 that the absolute water heights on deck prescribed motion case and freely moving

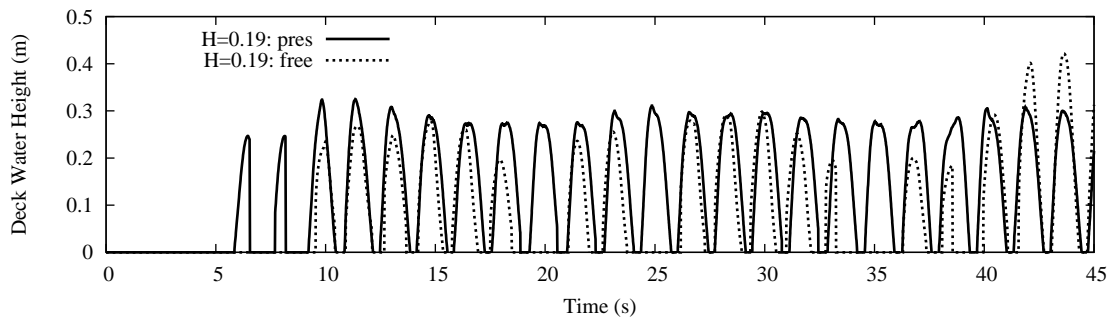


Figure 4.3: Absolute water height on deck

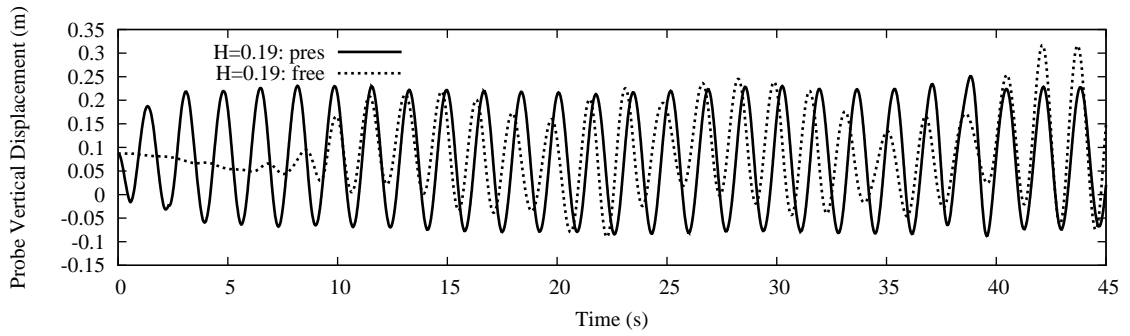


Figure 4.4: Vertical displacement of the wave probe on deck

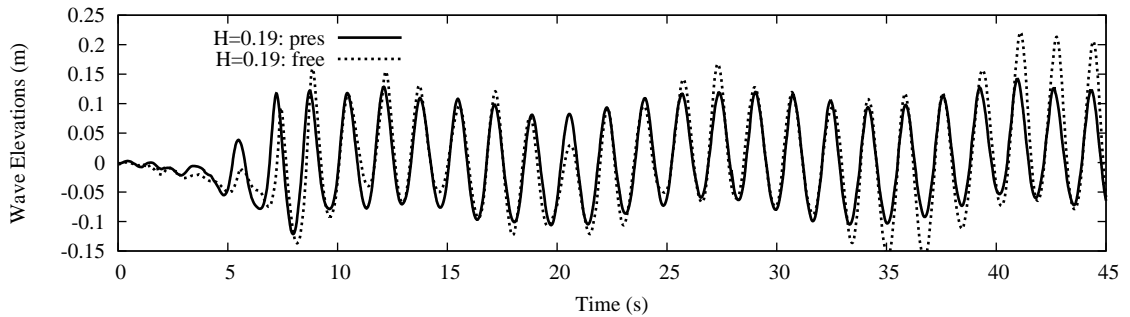


Figure 4.5: Comparison of the wave elevation

case are fairly close in comparison with the relative water heights on deck. Therefore, the vertical motion of the hull has a very large effect on green water on deck.

For further investigation, Figure 4.4 provides vertical displacement of wave probe at the same position on the deck (i.e., 0.08 m in front of the deckhouse) for both cases, and Figure 4.5 shows wave elevation at a same give position in front of the hull. It can be seen from Figure 4.4 that the lowest position of the wave probe for freely moving case is higher than the one for prescribed motion case for most periods; on the other hand, the incoming wave elevation is fairly close between these two cases, as shown in Figure 4.5. That also explains that there are less green water on deck for freely moving case than those for the prescribed motion case.

In addition, Figure 4.6 shows the heave force and pitch moment for both prescribed motion and freely moving cases. It can be seen that significantly larger heave force and pitch moment occur to the prescribed motion case. It shows that small difference in ship

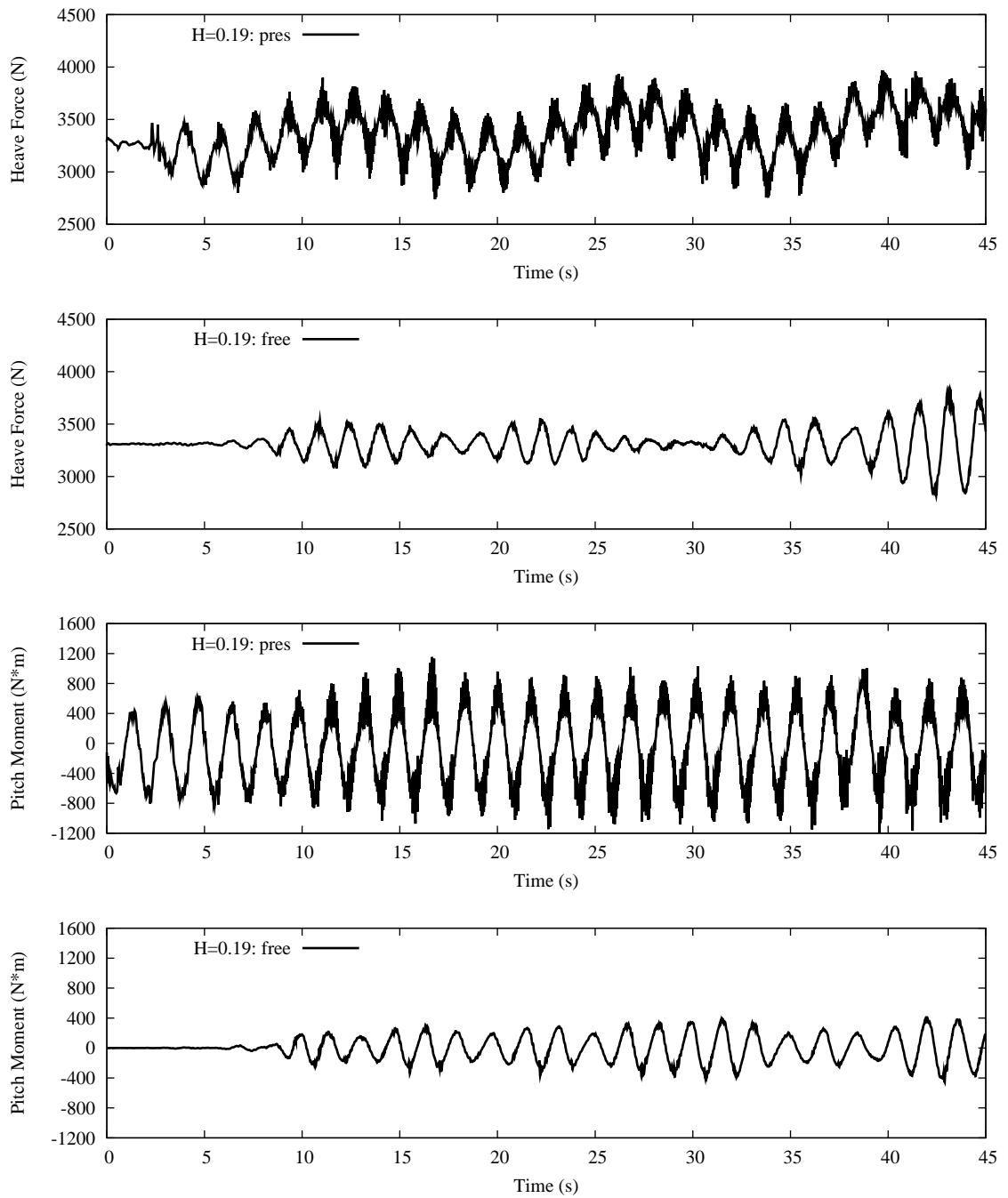
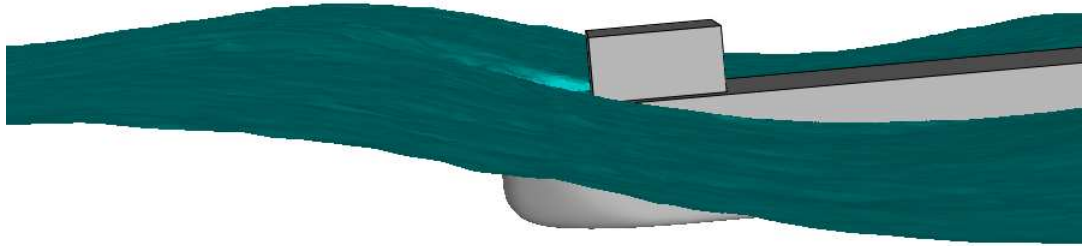
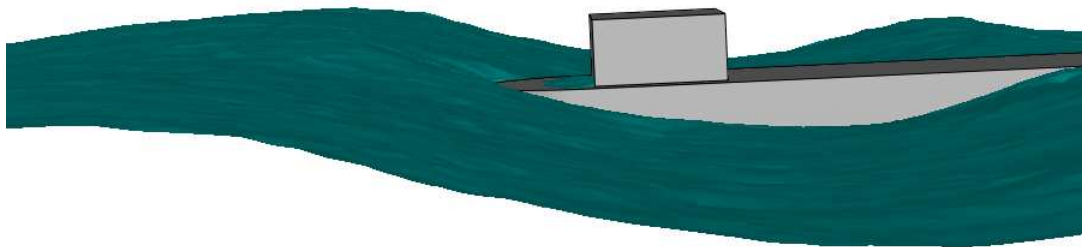


Figure 4.6: Comparison of heave force and pitch moment

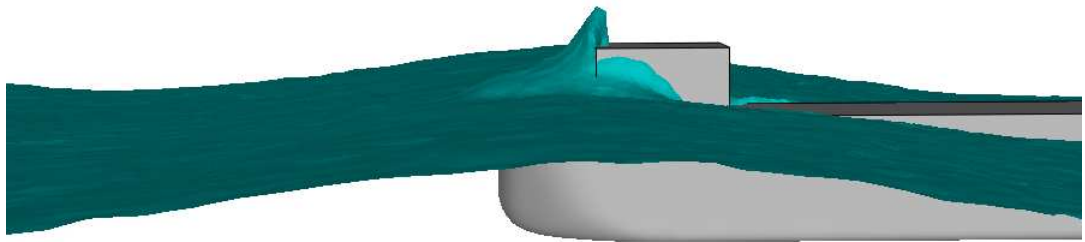


Time=1.063600e+01

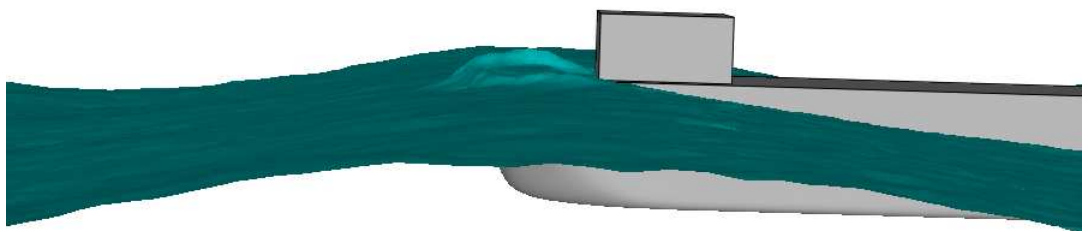


Time=1.067200e+01

Figure 4.7: Snapshots of the free surface wave elevation (top: prescribed motion; bottom: freely moving (1))

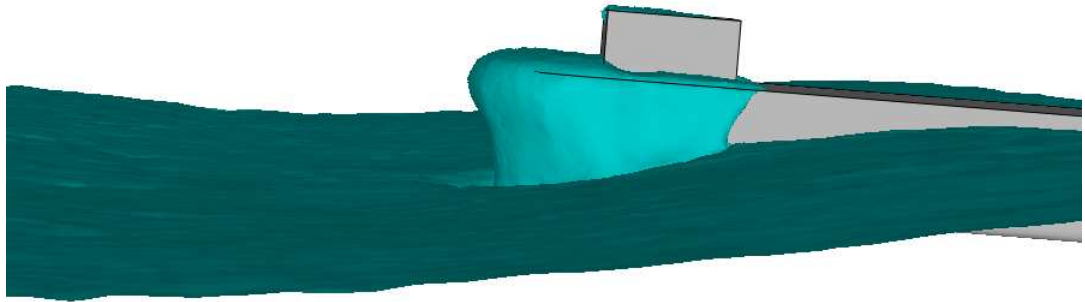


Time=1.275100e+01

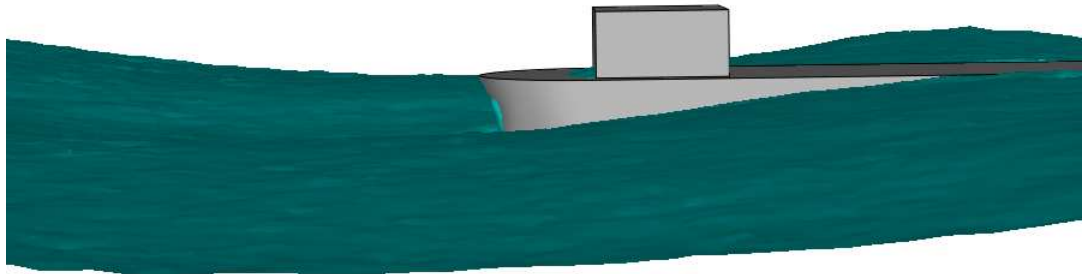


Time=1.275700e+01

Figure 4.8: Snapshots of the free surface wave elevation (top: prescribed motion; bottom: freely moving (2))

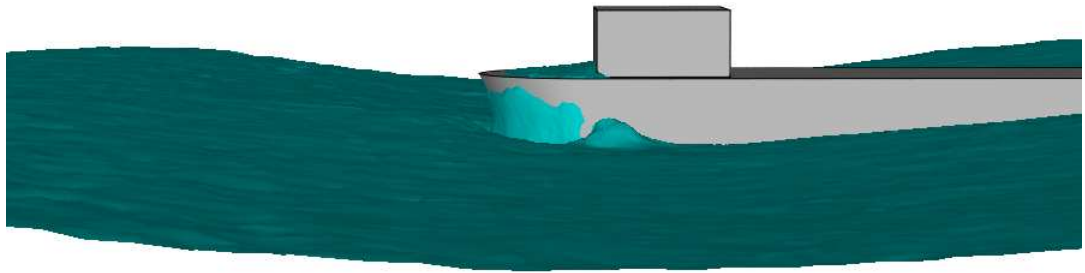


Time=3.357800e+01

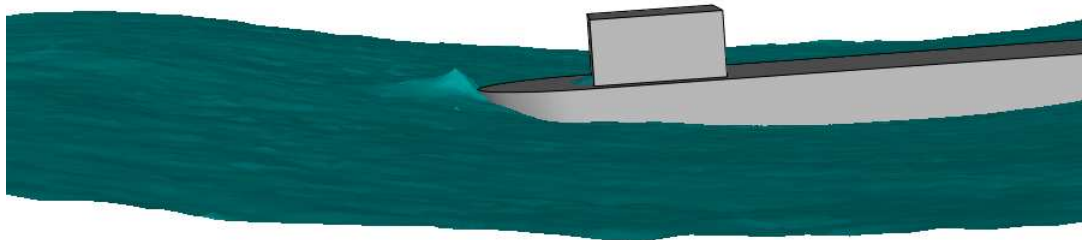


Time=3.357800e+01

Figure 4.9: Snapshots of the free surface wave elevation (top: prescribed motion; bottom: freely moving (3))



Time=3.400300e+01



Time=3.401200e+01

Figure 4.10: Snapshots of the free surface wave elevation (top: prescribed motion; bottom: freely moving (4))

motion in same extreme waves may result in large differences in forces on the hull. In particular, the FPSO model with prescribed motion in the present simulation accounts for larger loading forces and more green water shipping on the deck than the freely moving model in the same wave environment. The latter phenomenon can be observed in following 3-D snapshots from the numerical simulation. Figures 4.7, 4.8, 4.9, and 4.10 show the snapshots of the free surface elevation on the deck of the FPSO with prescribed motion (top) and that for the ship free to heave and pitch (bottom) at four selected time instances. As shown in these above figures, relatively mild green water loading on the deck can be observed for the freely moving case.

4.3 FPSO Model Moored in Extreme Waves

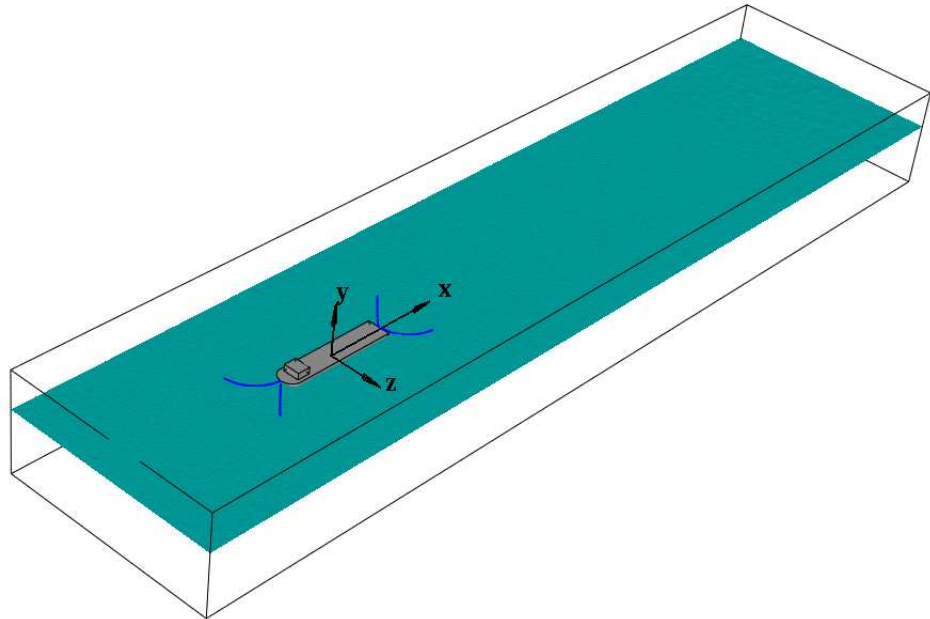


Figure 4.11: FPSO model moored in wave tank

The same FPSO model is further used in the numerical investigation of the mooring effects on a single FPSO model in extreme waves. Two cases are considered for comparison in this problem: the FPSO model sits in the extreme waves without and with mooring constraints. A spreading mooring system, as shown in Figure 4.11, is applied on the FPSO model. This

mooring system consists of four mooring cables: two of them are set at the front, and the other two the back. For the given head wave condition, the ship in each case is allowed to move in surge, heave, and pitch motions (i.e., 3-DOF).

The comparison of the motion responses of a freely moving FPSO and a moored FPSO is shown in Figure 4.12. It can be seen from Figure 4.12 that the surge motion in the moored FPSO case is reduced significantly in comparison to the freely moving FPSO case, as expected. We can also observe the effects of the mooring constraints to the heave and pitch motion, even though they are less significant than that of the surge motion.

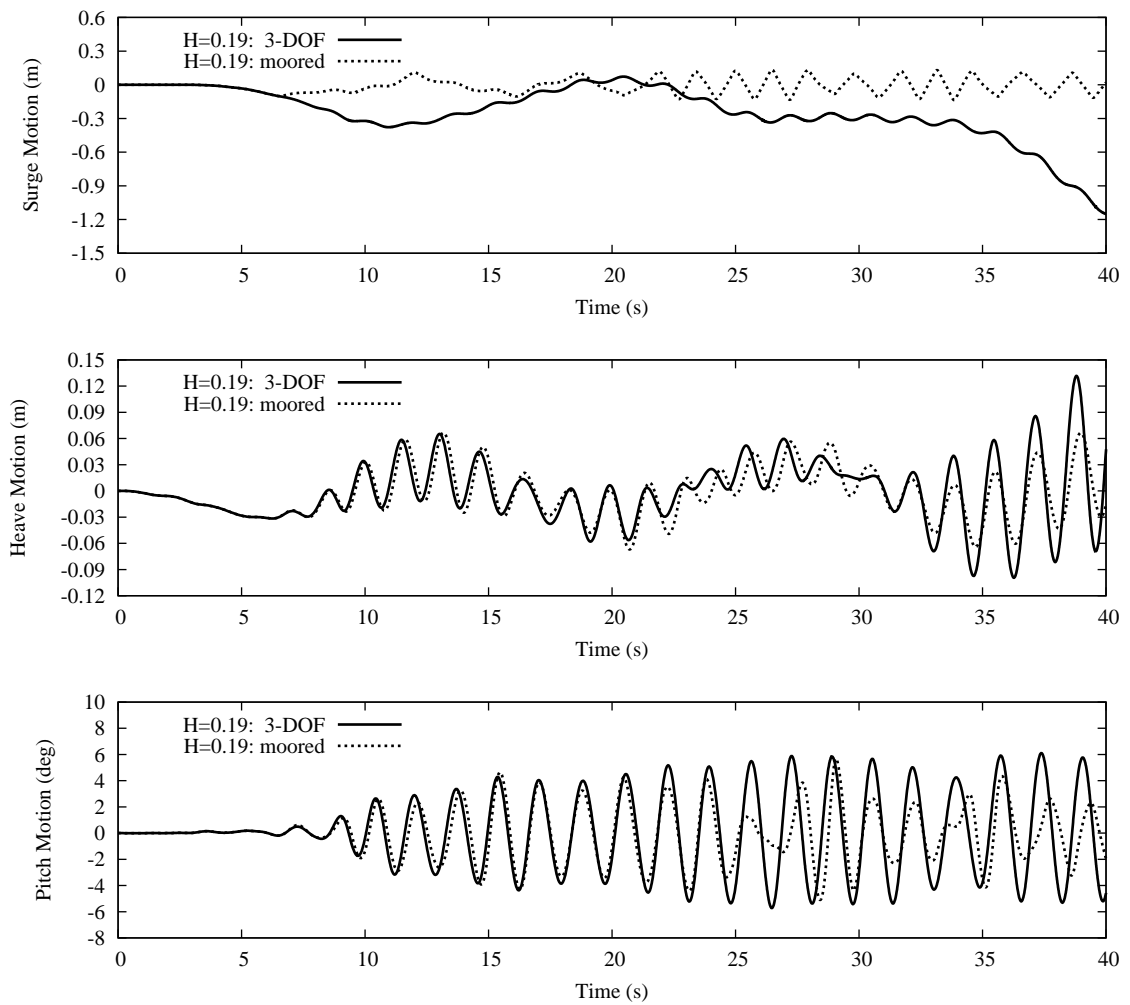


Figure 4.12: Comparison of motion responses of FPSO model with and without mooring constraints

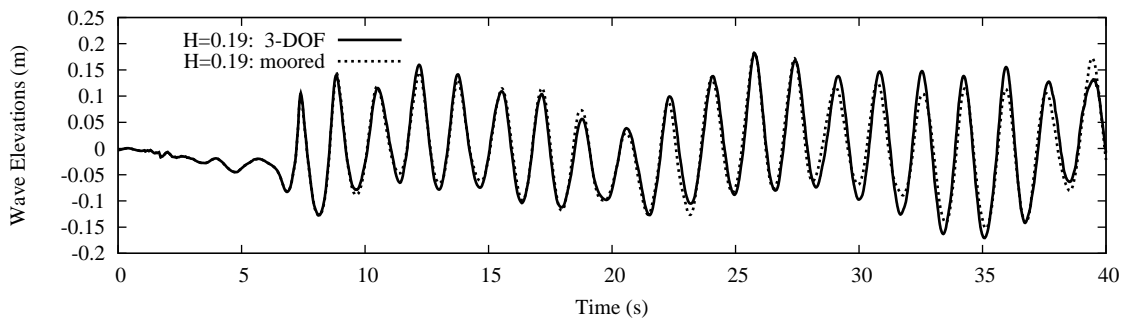


Figure 4.13: Comparison of the wave elevation at wave probe in front of the FPSO

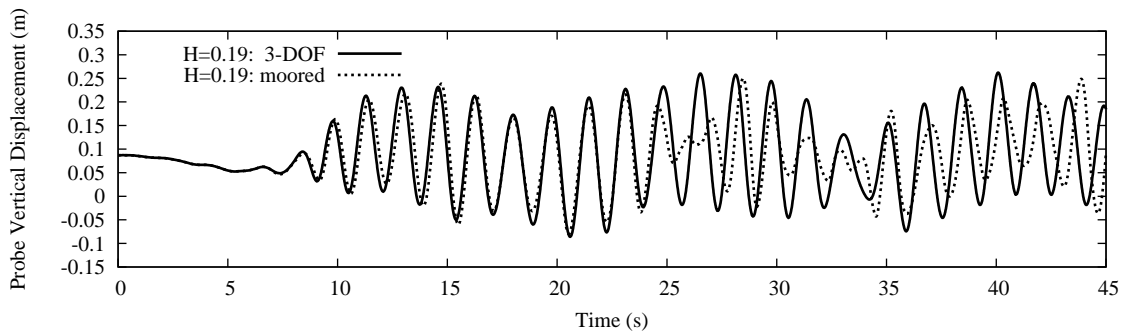


Figure 4.14: Vertical displacement of the wave probe on deck

The wave elevation at the given wave probe in front of the hull is also compared between the freely-moving FPSO case and the moored FPSO case, as shown in Figure 4.13. In addition, the water height at a given location on the deck in front of the deckhouse is recorded for both cases. The time history of the vertical displacements of this location for both cases are plotted in Figure 4.14. The comparison of the water height on the deck for the freely-moving FPSO case and the moored FPSO case is plotted in Figure 4.15.

It can be seen from Figure 4.13 that the wave elevations in front of the FPSO in two cases are similar at early time, and slightly different after 17 seconds due to the fact that the reflected waves generated by a freely-moving FPSO and a moored FPSO are different.

Figure 4.14 also shows the small difference of the vertical displacement of the wave probe on deck for both cases. The displacement of the wave probe on deck is somewhat reduced in the moored FPSO case due to the fact that the heave and pitch motions are smaller in comparison to the freely-moving FPSO case. The large differences of the water height on

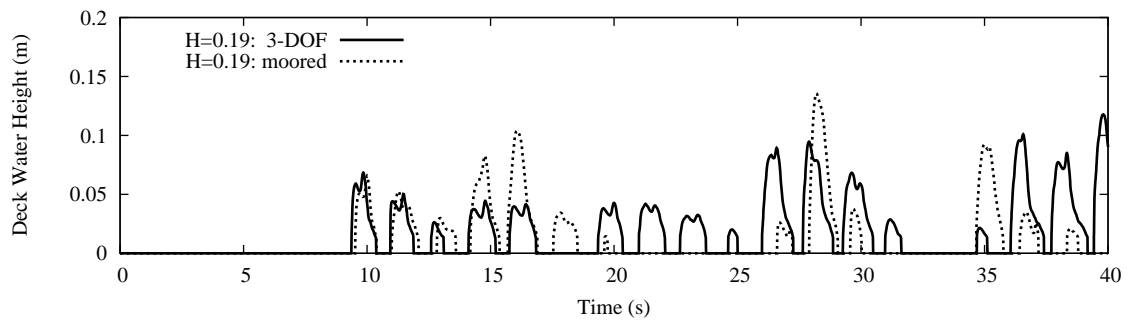


Figure 4.15: Comparison of the water height on deck

the deck between the freely-moving FPSO and the moored FPSO can be observed from Figure 4.15. The same scenario over the deck area in front of the deckhouse has also been confirmed by the 3-D views of green water on deck.

4.4 Two Side-by-side Vessels Moored in Extreme Waves

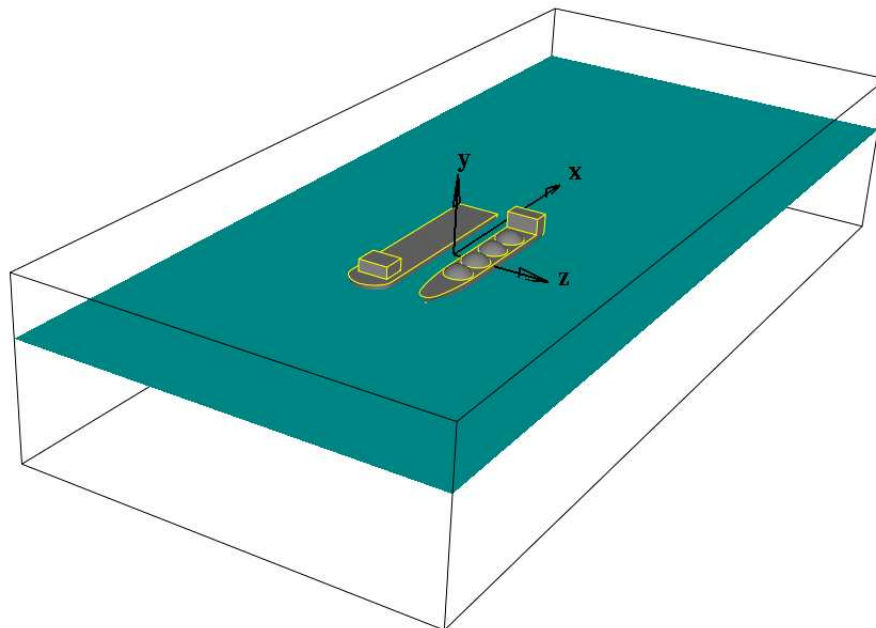


Figure 4.16: Side-by-side FPSO and LNGC freely moving

Side-by-side mooring configuration is widely used in marine engineering, but it is still a challenging problem for vessels in harsh environment. Furthermore, the offloading operation

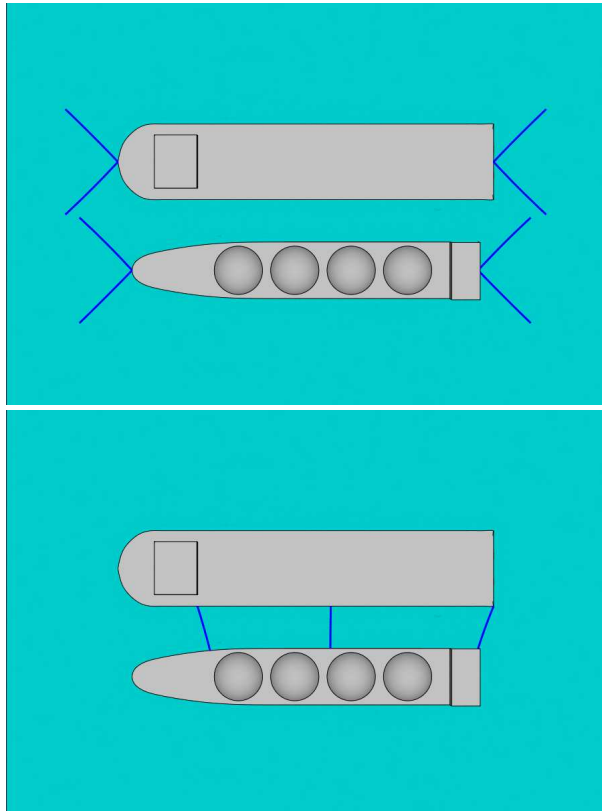


Figure 4.17: Side-by-side FPSO and LNGC with different mooring configurations

of LNG between terminals and carriers needs special care due to the unique requirements of LNG storage and transportation. Therefore, there is a great need for prediction of ship motions and interaction between vessels in this situation, and for reliable solutions to this problem.

In this dissertation, we first simulate two side-by-side FPSO and LNGC in extreme waves, as shown in Figure 4.16. In particular, three cases are considered: freely moving side-by-side FPSO and LNGC, side-by-side FPSO and LNGC with spread mooring constraints, and side-by-side FPSO and LNGC with side mooring constraints. For these cases with mooring constraints, a simple mooring cable model is used with different configurations, which are illustrated in Figure 4.17. Specially, for the case with spreading mooring constraints, these two vessels are moored side-by-side with individual mooring constraints on each vessel. As shown on the top of Figure 4.17, each system consists of four mooring cables: two mooring lines are attached to the bow and the other two are attached to the

Table 4.1: Main particulars for FPSO model and LNGC model

	units	FPSO Model	LNGC Model
length	m	3.5156	3.2178
beam	m	0.7188	0.5368
depth	m	0.3766	0.3735
draft	m	0.2896	0.2664
displacement	t	0.6748	0.3452

stern. The angle between each mooring line and the symmetrical plane of the relevant hull is 45 *degrees*. For the case with side mooring constraints, three mooring lines are attached between these two vessels as shown on the bottom of Figure 4.17.

The problem definition and the coordinate system are shown in Figure 4.16. The main particulars of two vessels are given in Table 4.1. Each vessel is treated as a rigid body that can move in 6-DOF in response to the waves. A same mesh configuration is applied for all three cases, as shown in Figure 4.18: uniform mesh size is applied to the most of the computational domain, with coarse mesh set on the far end in the downstream for numerical wave damping and relatively fine mesh specified on the surface of each vessel.

4.4.1 Freely Moving Side-by-side FPSO and LNGC

The first case considered in this problem is the numerical simulation of freely moving side-by-side FPSO and LNGC in head waves, as shown in Figure 4.16.

The comparison of the motion responses of FPSO and LNGC induced by extreme waves are shown in Figure 4.19. Significant differences between FPSO and LNGC responses can be observed in surge, heave, yaw, and sway motions, while roll and pitch motion responses of these two different vessels are relatively close. Specially, the plot in sway motion shows that these two vessels first approach together till around 30sec, then eventually separate away from each other. It also shows clearly in yaw motion that there is a contact at $t = 20 \text{ sec}$ between these two vessels.

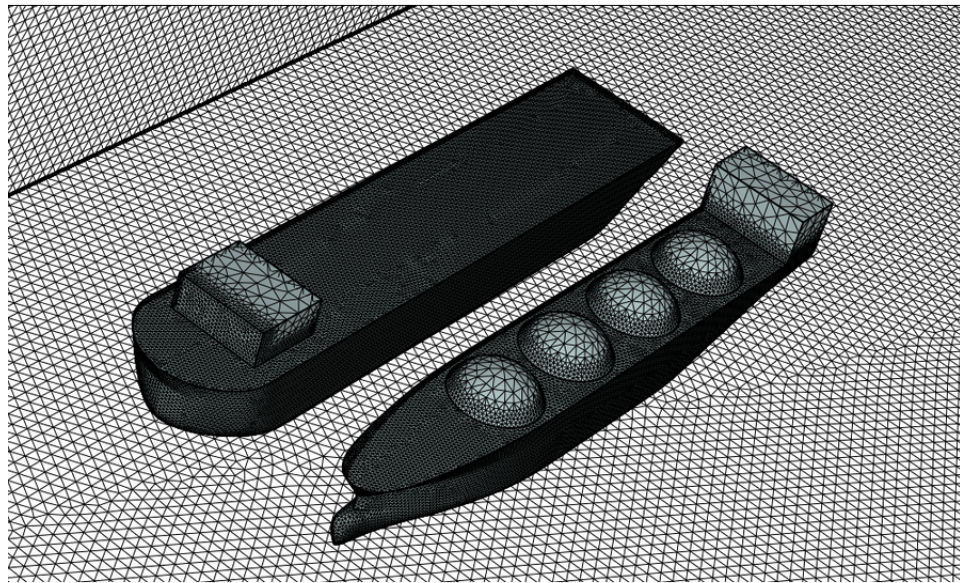
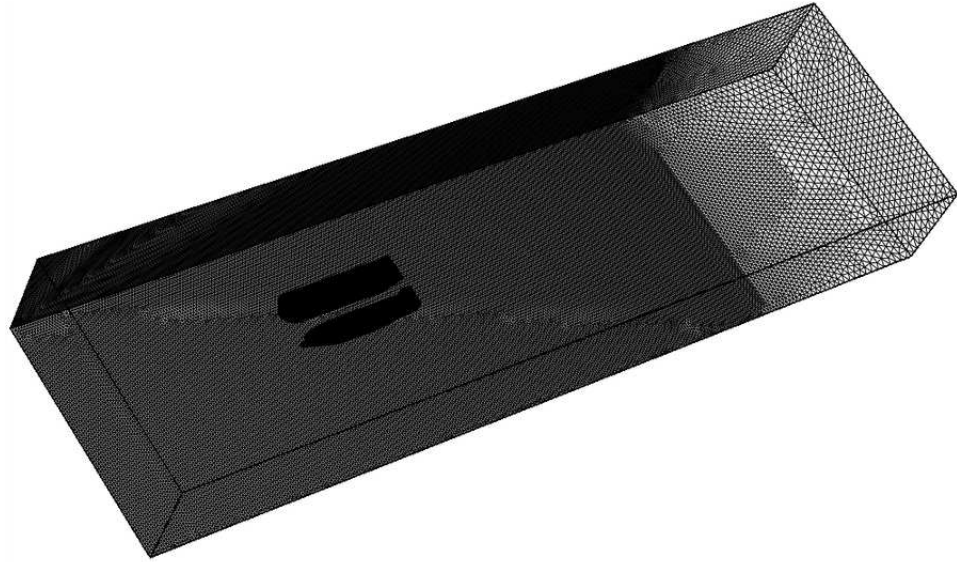


Figure 4.18: Mesh configuration: surface grids on walls of the tank (top) and the ship bodies(bottom)

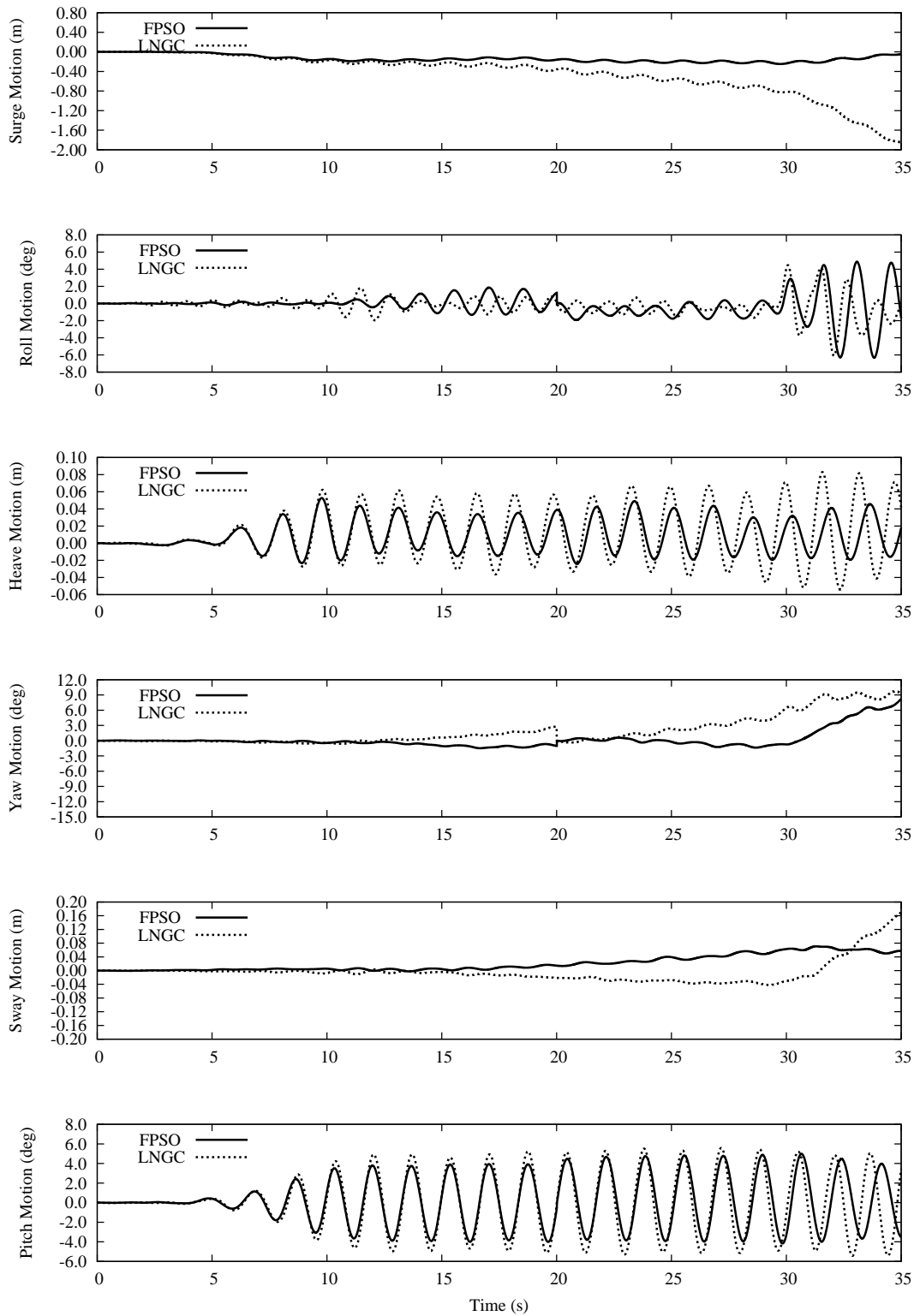


Figure 4.19: Motion responses of freely moving side-by-side FPSO and LNGC

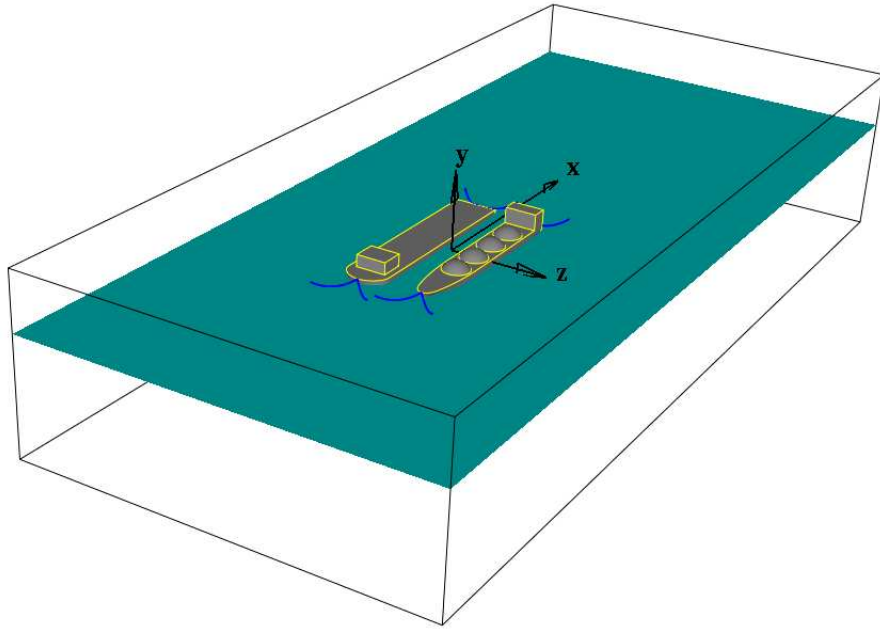


Figure 4.20: Side-by-side FPSO and LNGC constrained with spread mooring cables

4.4.2 Side-by-side FPSO and LNGC with Spread Mooring constraints

The second case considered is side-by-side FPSO and LNGC moored in head waves, where the vessels are constrained by a spreading mooring system as shown above. Figure 4.20 gives the 3-D view of this problem. The comparison of the motion response of FPSO and LNGC in this case are shown in Figure 4.22. It shows that considerable difference of motion responses between FPSO and LNGC can only be seen in roll and sway motions, while others are fairly close due to the spreading mooring constraints.

4.4.3 Side-by-side FPSO and LNGC with Side Mooring constraints

The last case considered in this problem is side-by-side FPSO and LNGC moored in head waves, with the side-by-side mooring configuration as shown above. Figure 4.21 gives the 3-D view of this problem. The comparison of the motion responses of FPSO and LNGC are shown in Figure 4.23. It can be seen that, given the side mooring constraints as such, the significant difference between two vessels occurs in sway motion; and it is considerably different to the spreading mooring case.

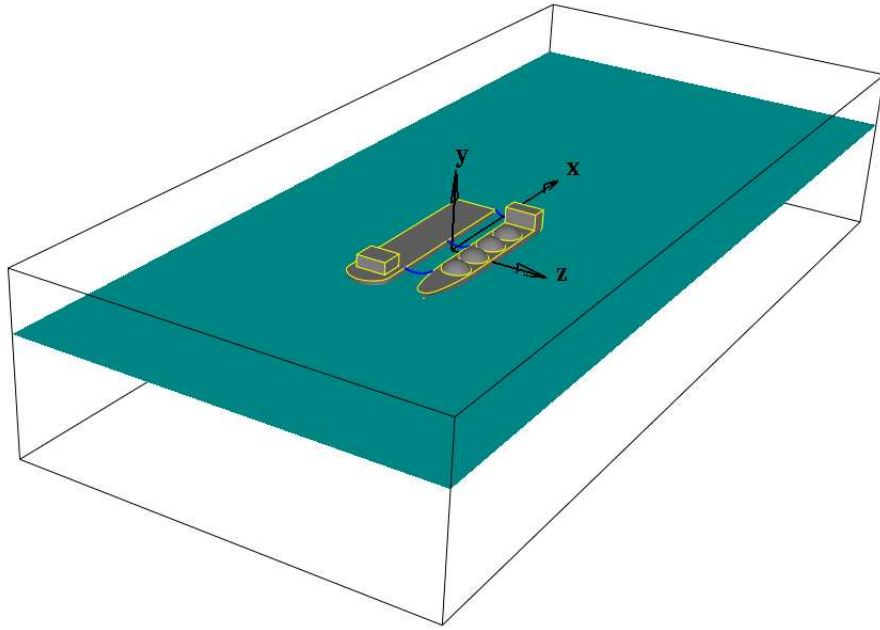


Figure 4.21: Side-by-side FPSO and LNGC constrained with side mooring cables

Moreover, in order to investigate the effects of mooring constraints on the motion responses of vessels, motion responses of FPSO and LNGC with different constraints are compared in Figures 4.24 and 4.25. Specifically, Figure 4.24 shows the comparison of motion responses of FPSO with different constraints, and Figure 4.25 shows the similar comparison of the LNGC.

It is clear that for all three side-by-side configurations, considerable responses of sway, roll, and yaw motions can be observed for both vessels even though the vessels are in head waves. This phenomenon can be attributed to the hydrodynamic interactions of two vessels. Figures 4.24 and 4.25 also show that different mooring configurations affect the motion responses of the vessels in a quite different ways.

It can also be seen from these two figures that the spread mooring system can significantly reduce responses of surge and yaw motions, and it also provides comparable constraints to heave, sway, and pitch motions. However, larger responses of roll motions are observed in this mooring configuration than the side mooring configuration. On the other hand, the side mooring configuration can not only offer reasonable constraints on surge

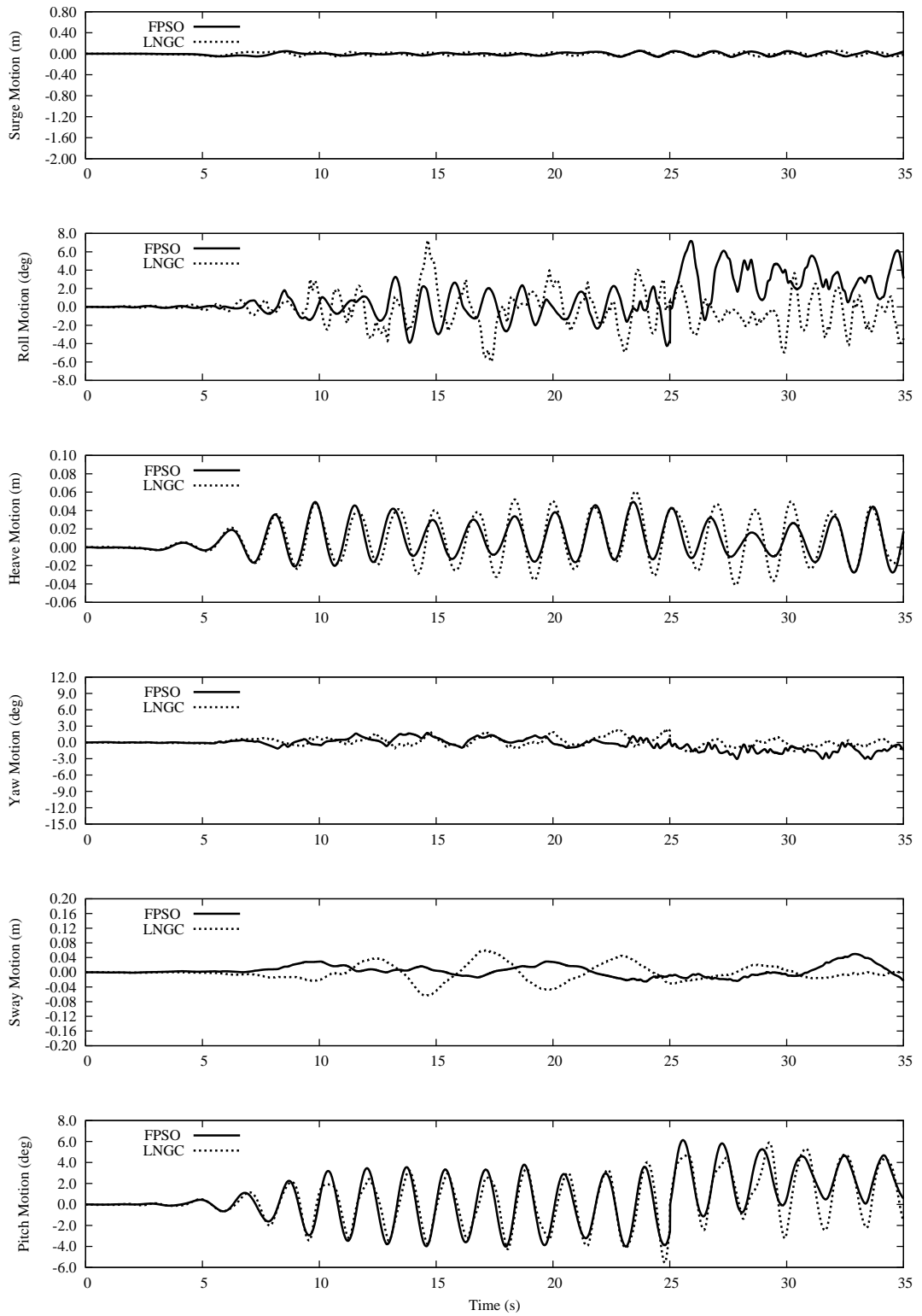


Figure 4.22: Motion responses of side-by-side FPSO and LNGC with spread mooring cables

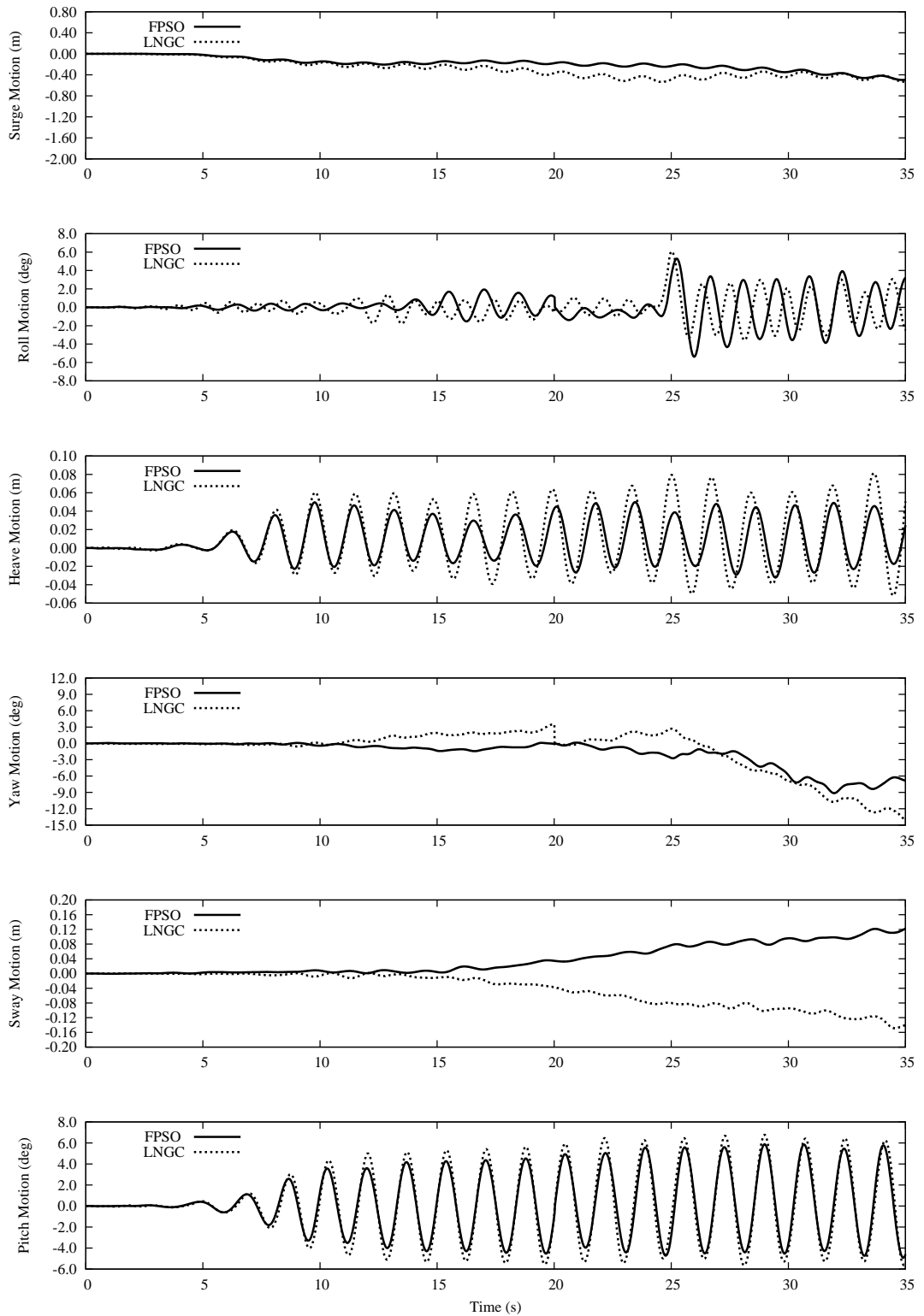


Figure 4.23: Motion responses of side-by-side FPSO and LNGC with side mooring cables

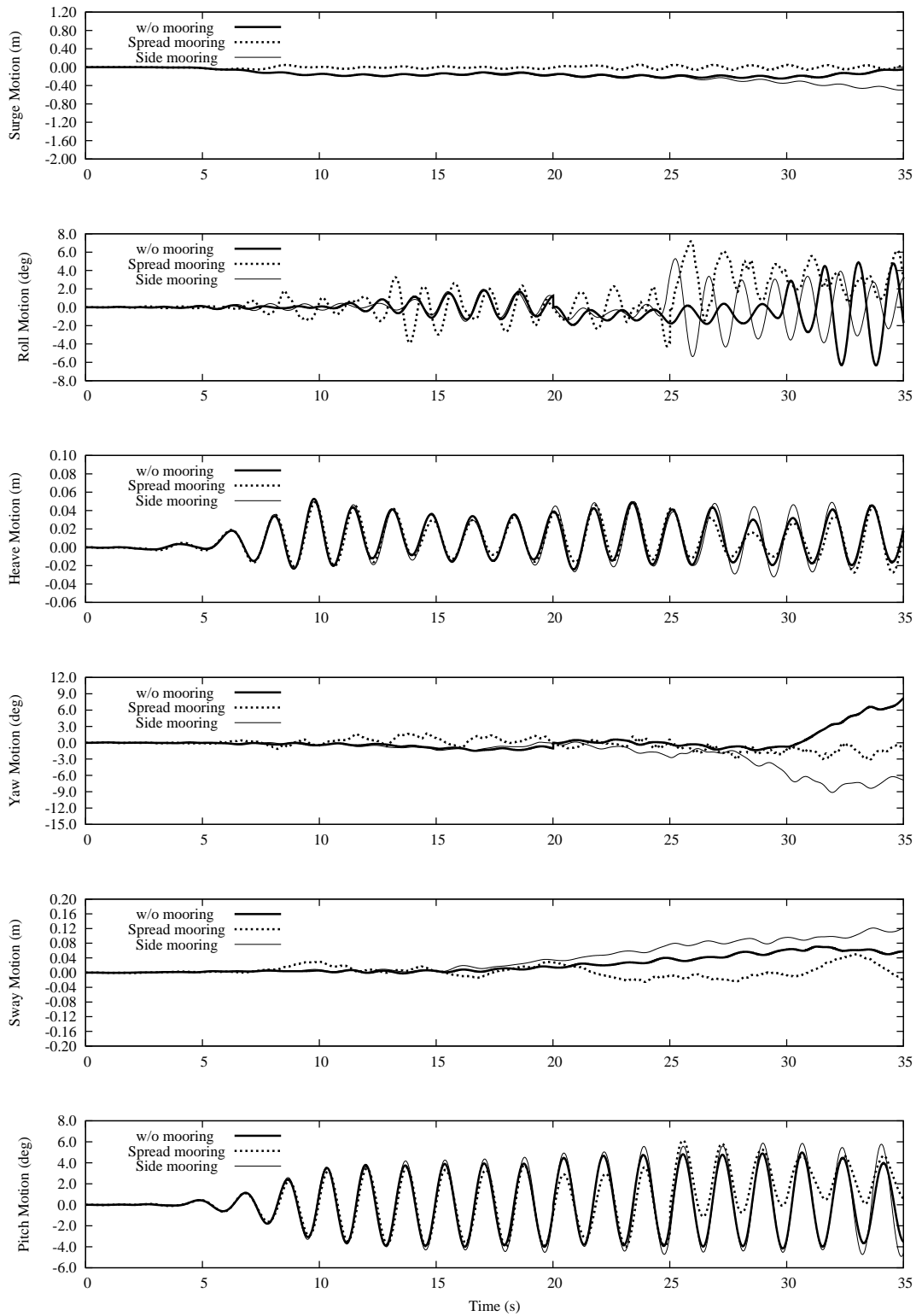


Figure 4.24: Comparison of motion responses of side-by-side FPSO and LNGC with or without mooring constraints (FPSO)

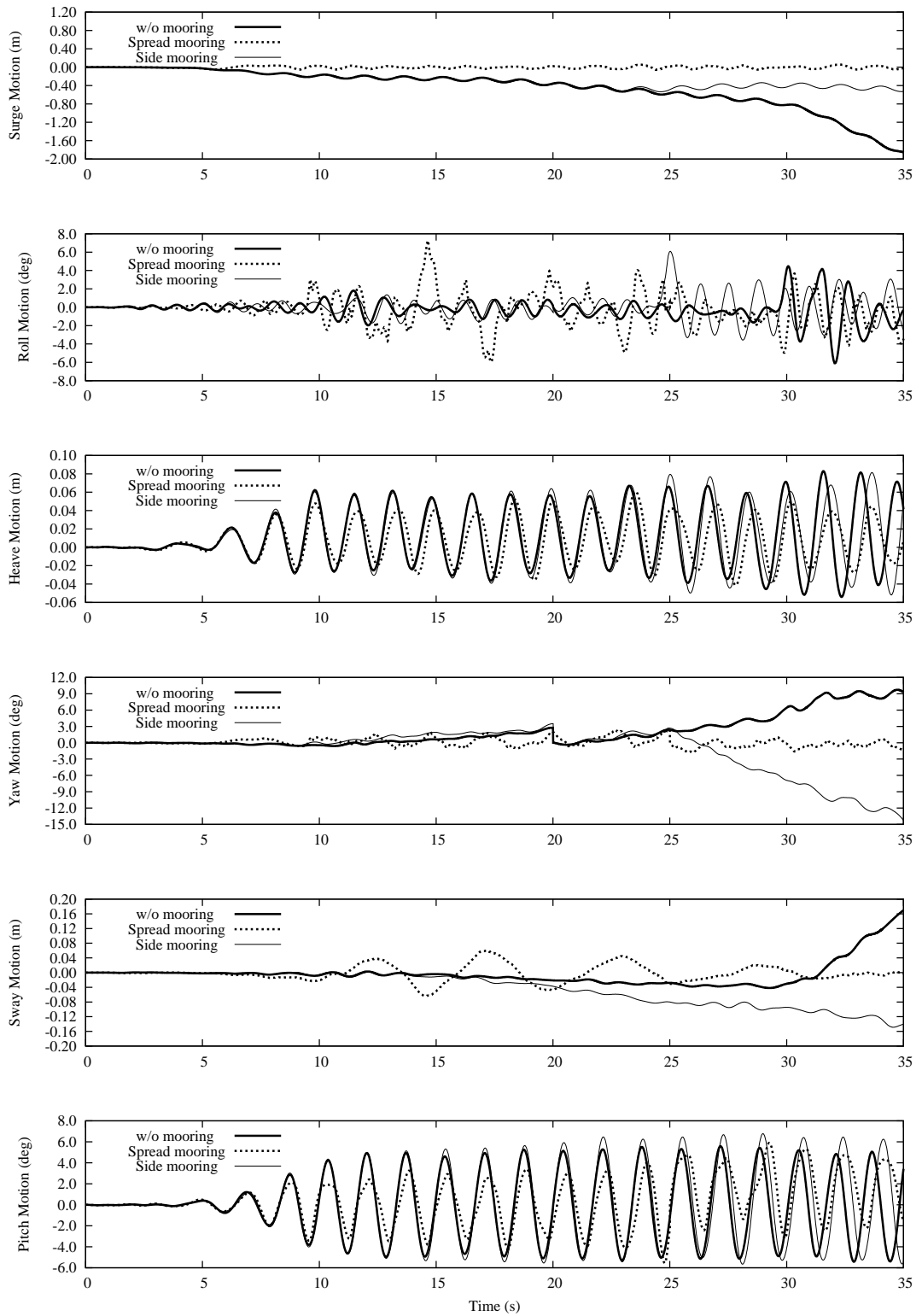
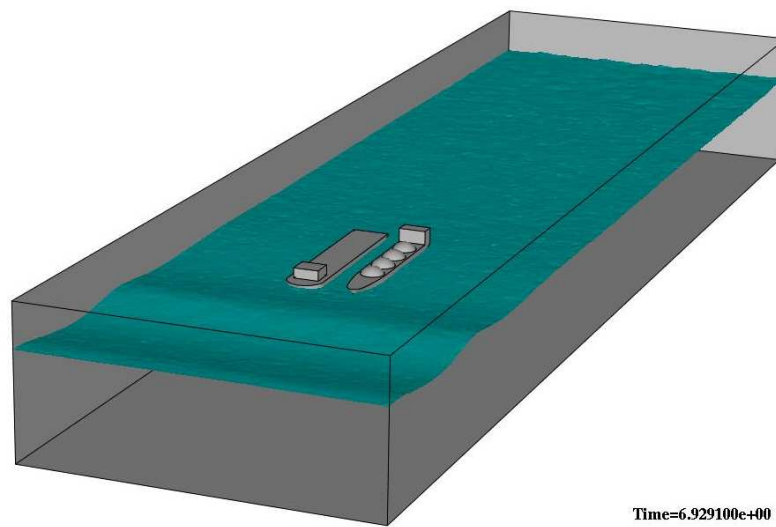
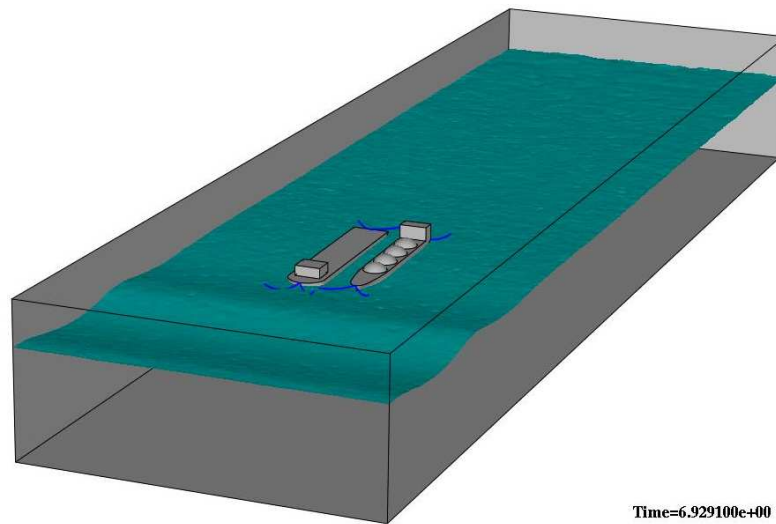


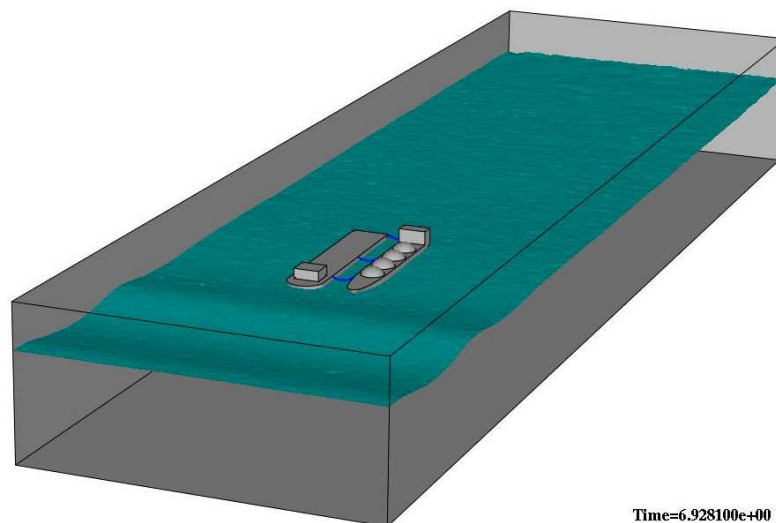
Figure 4.25: Comparison of motion responses of side-by-side FPSO and LNGC with or without mooring constraints (LNGC)



Time=6.929100e+00



Time=6.929100e+00



Time=6.928100e+00

Figure 4.26: Snapshots of side-by-side FPSO and LNGC in extreme waves with or without mooring constraints (top: free; middle: spreading mooring constraint; bottom: side mooring constraint)

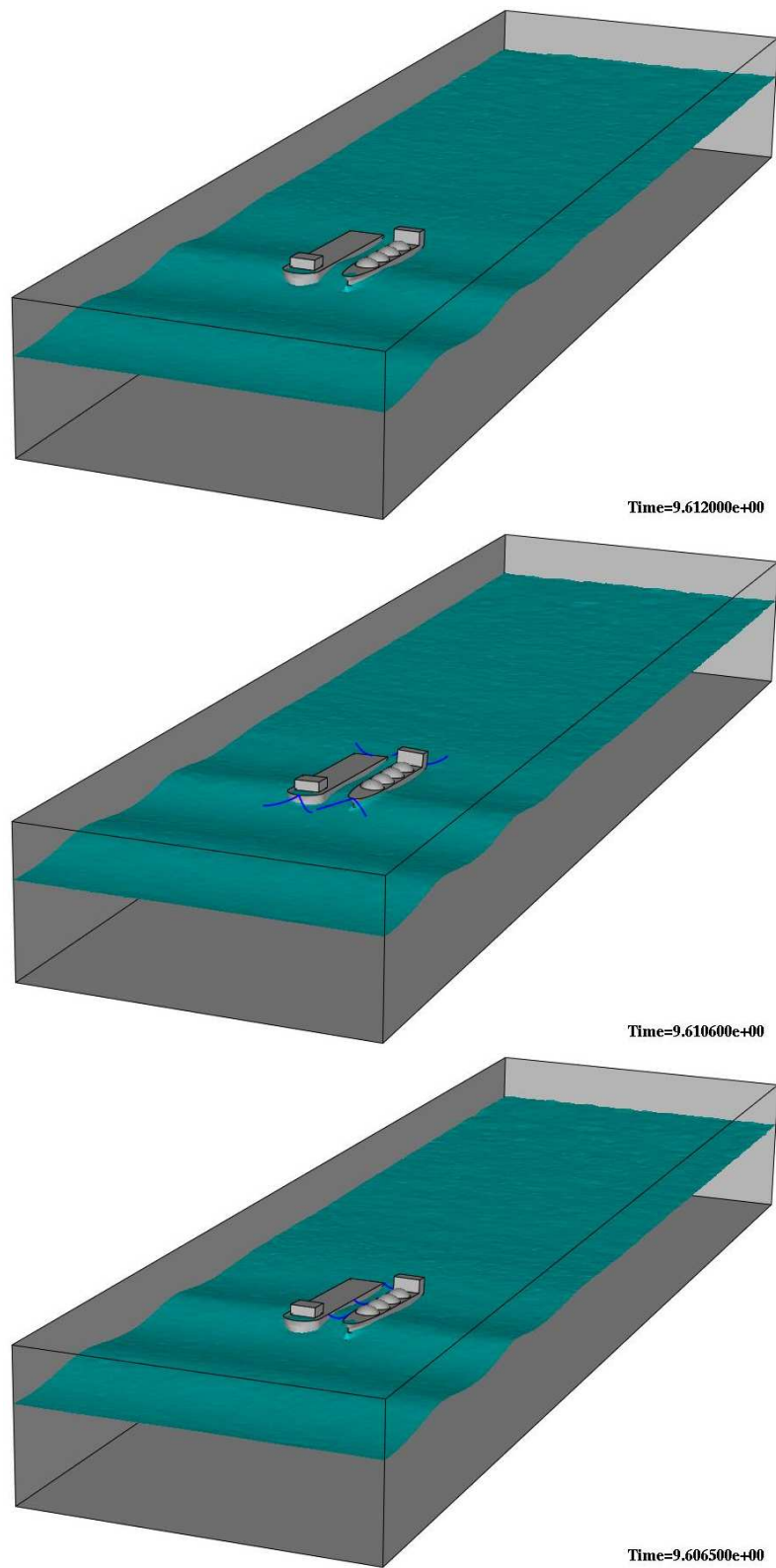


Figure 4.27: Snapshots of side-by-side FPSO and LNGC in extreme waves with or without mooring constraints (top: free; middle: spreading mooring constraint; bottom: side mooring constraint)

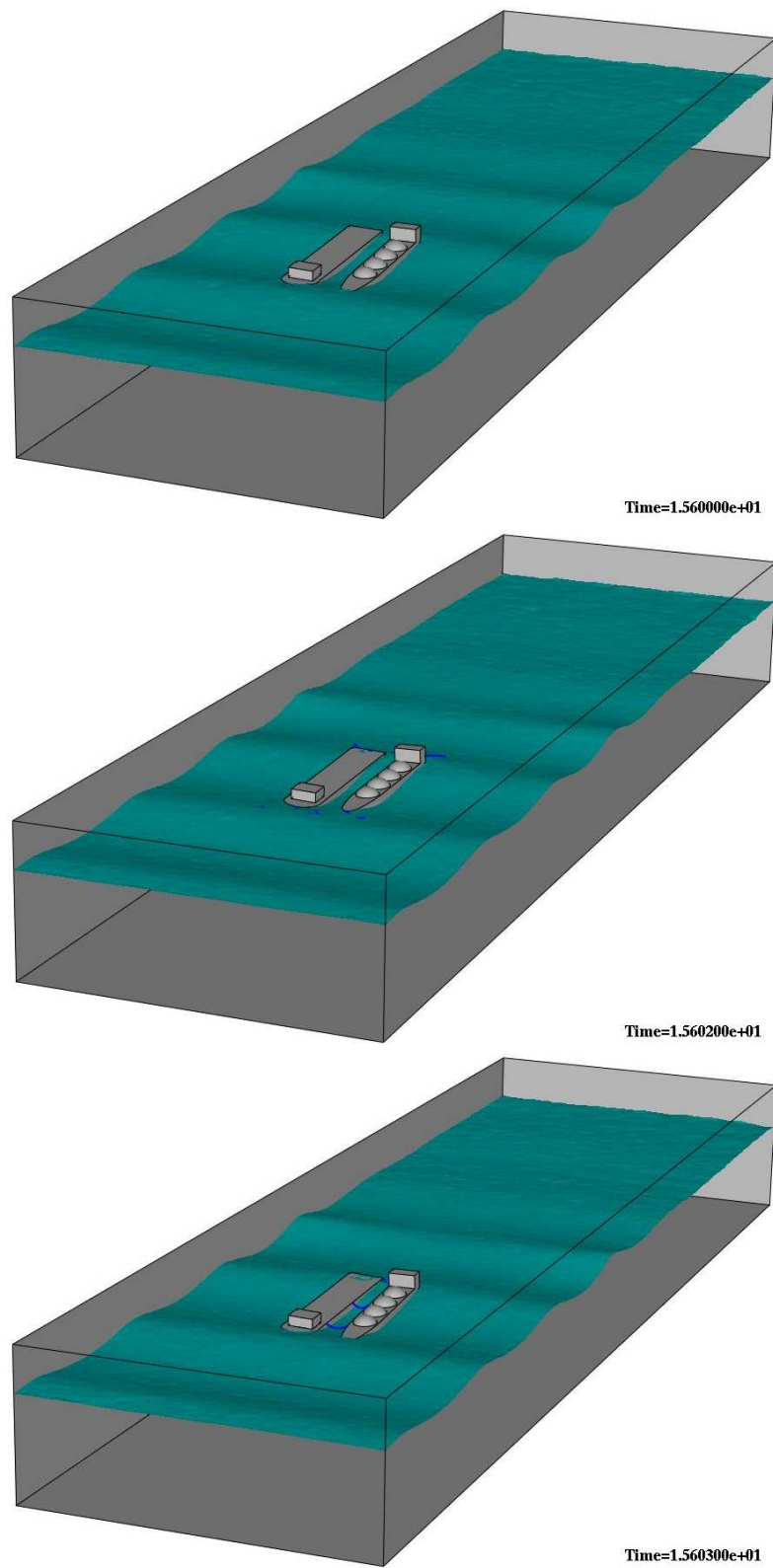


Figure 4.28: Snapshots of side-by-side FPSO and LNGC in extreme waves with or without mooring constraints (top: free; middle: spreading mooring constraint; bottom: side mooring constraint)

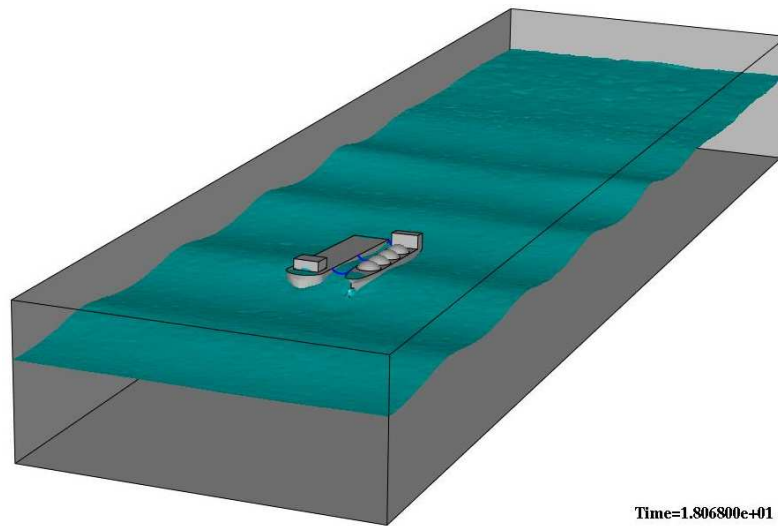
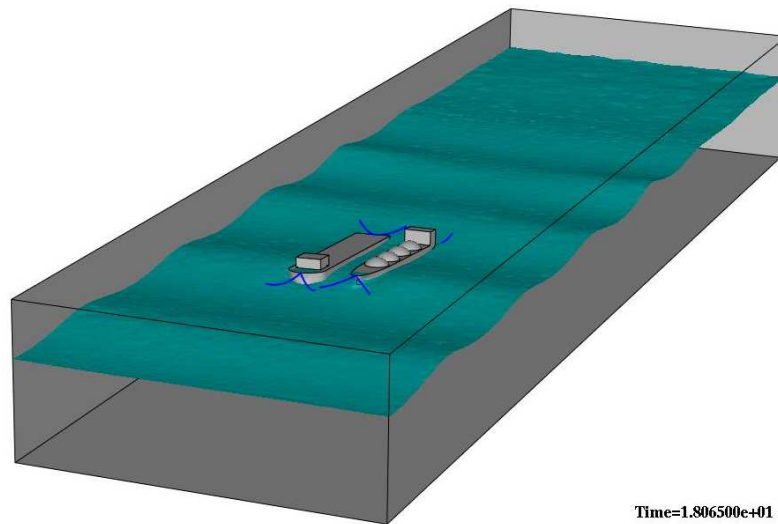
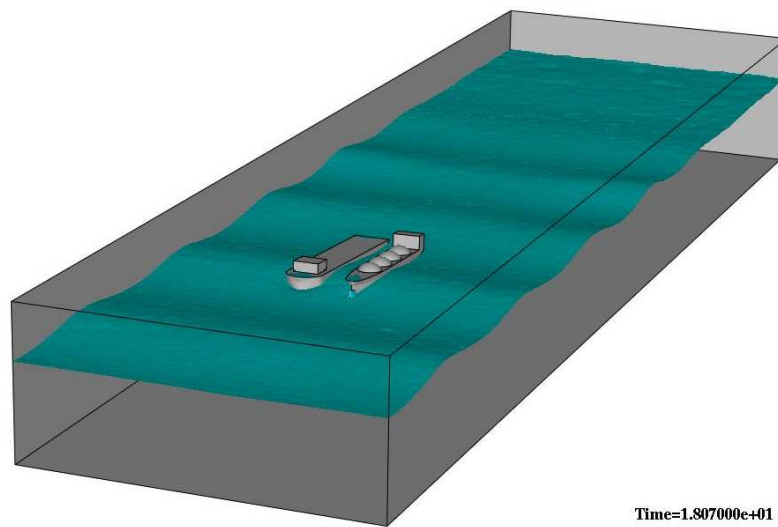


Figure 4.29: Snapshots of side-by-side FPSO and LNGC in extreme waves with or without mooring constraints (top: free; middle: spreading mooring constraint; bottom: side mooring constraint)

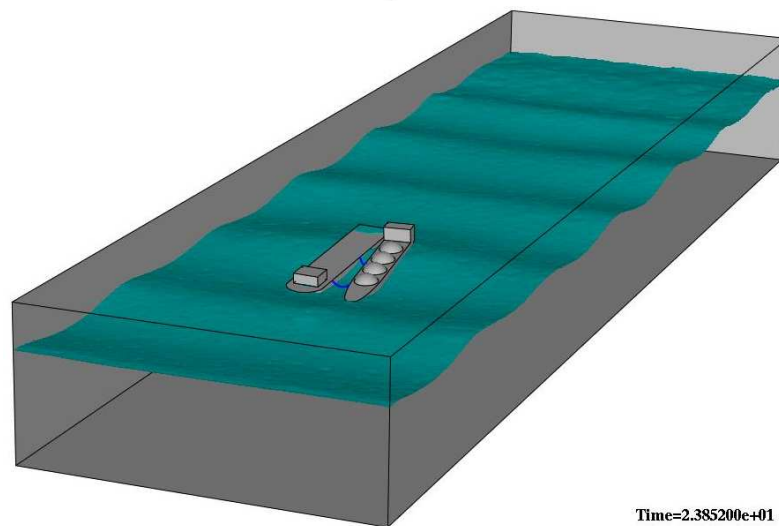
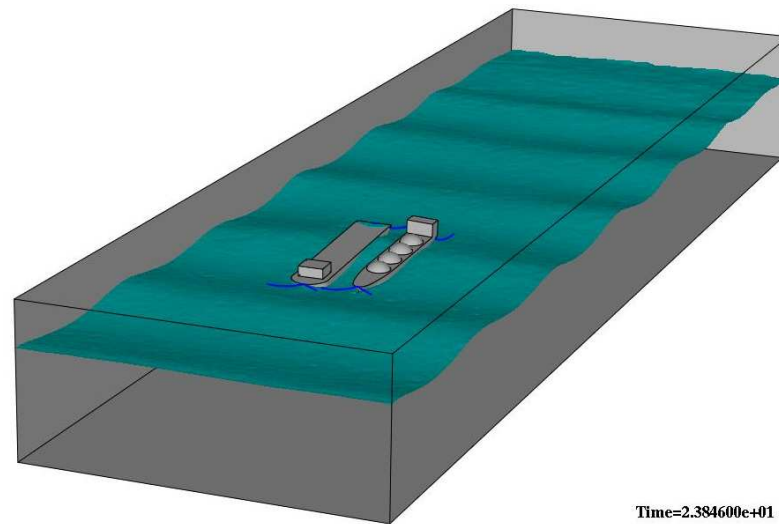
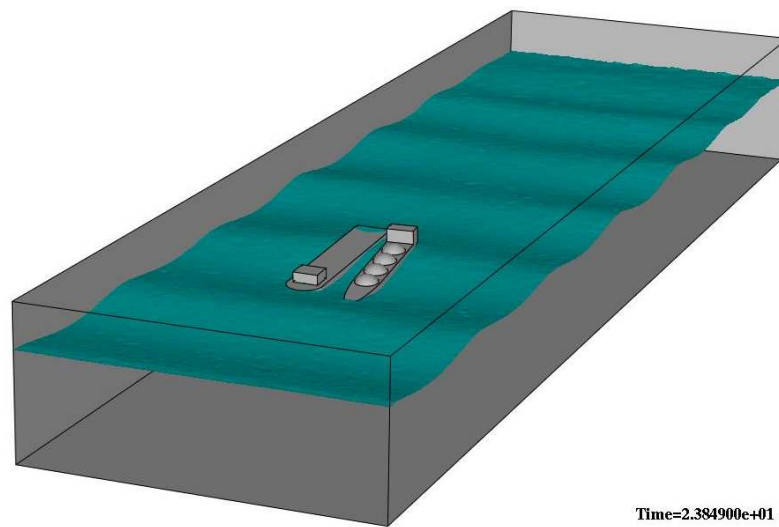


Figure 4.30: Snapshots of side-by-side FPSO and LNGC in extreme waves with or without mooring constraints (top: free; middle: spreading mooring constraint; bottom: side mooring constraint)

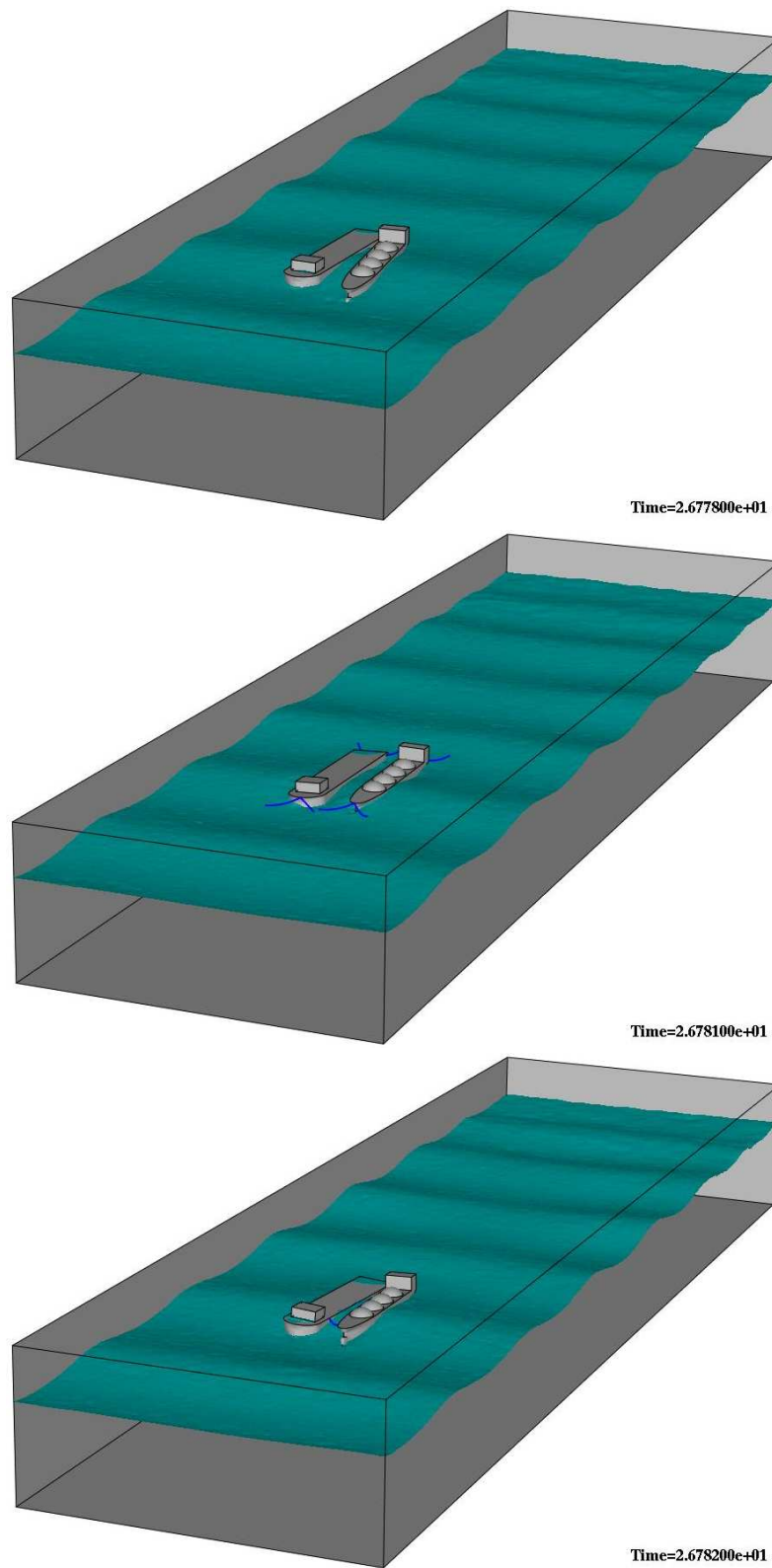


Figure 4.31: Snapshots of side-by-side FPSO and LNGC in extreme waves with or without mooring constraints (top: free; middle: spreading mooring constraint; bottom: side mooring constraint)

motion responses, but also reduce roll motion response in comparison with spread mooring configuration.

It can be concluded from the present numerical study that the hydrodynamic interaction between FPSO and LNGC are very important when they are moored side-by-side with a very close distance between them. Finally, several 3-D snapshots selected from each case are shown in Figures 4.26-4.31. Green water can be observed on the decks of both vessels for all three cases.

4.5 Ships with Different Mooring Configurations

In offshore engineering, another common mooring approach during offloading operation is tandem configuration. The sketch of this problem can be seen in Figure 4.32, and those vessel can be moored together (as shown in the figure) or independently.

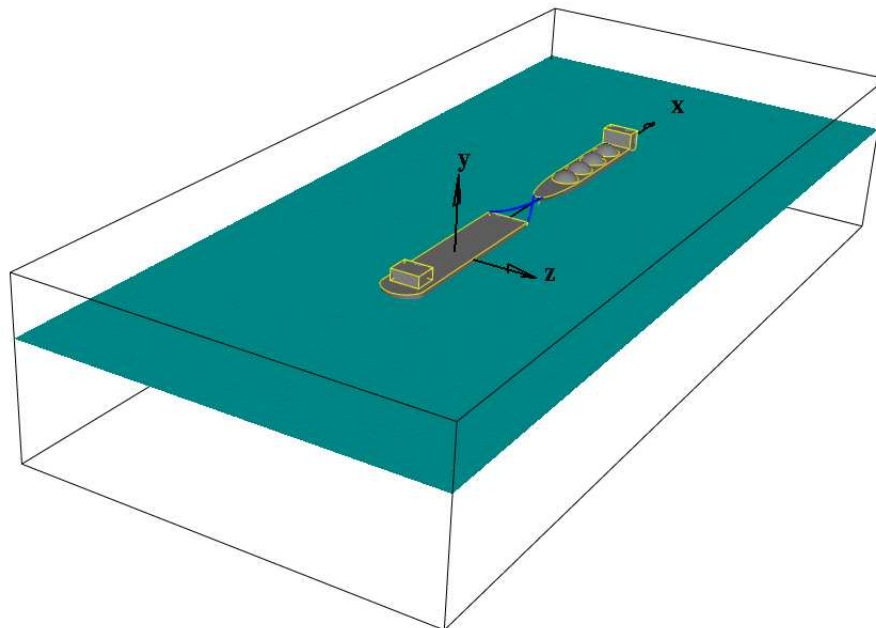


Figure 4.32: Problem definition of ships in tandem

4.5.1 Freely-Moving FPSO and LNGC in Tandem

In this dissertation particularly, the first case considered is freely-moving FPSO and LNGC in tandem in head waves, which is similar to what is shown in Figure 4.32 but without the mooring cables. Both ships are initially at rest in calm water and can move freely in 3-DOF (i.e., surge, heave and pitch), due to the fact that the flow is symmetric about the longitudinal middle plane of the ship in this case. The comparison of the motion responses of FPSO and LNGC are shown in Figure 4.33. Large surge motion responses can be observed on both ships from Figure 4.33. In addition, the LNGC experiences a larger surge and heave motions than FPSO due to its relative smaller size in comparison with FPSO. However, FPSO and LNGC experience a similar pitch motion response after 17 sec, and the difference before that moment is due to the different positions of each vessel along the wave propagation direction.

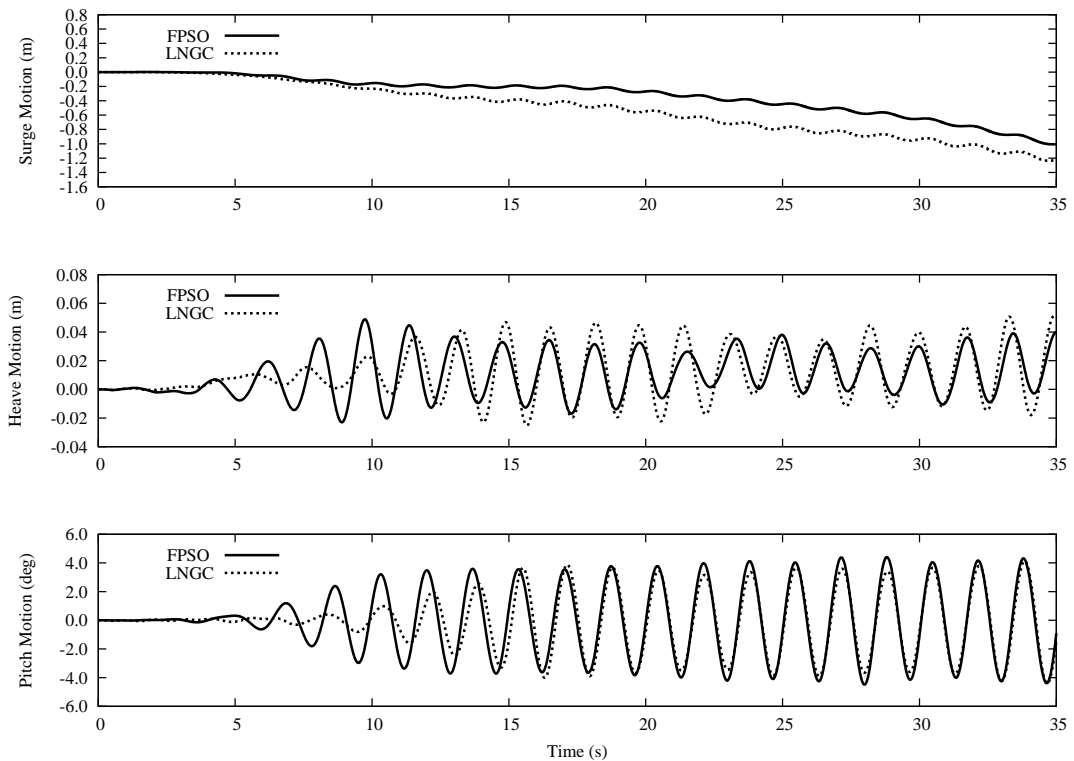


Figure 4.33: Comparison of motion responses of freely-moving FPSO and LNGC in tandem configuration

4.5.2 FPSO and LNGC in Tandem with Cross-mooring Cable Constrains

The second case considered is FPSO and LNGC in tandem with cross-mooring cable constraints in head waves. As shown in Figure 4.32, there are two cross cables between two ships. Both ships are initially at rest in calm water and can move freely in 3-DOF as same as these in the freely-moving case but constrained with cross-mooring cables. The comparison of the motion responses of FPSO and LNGC are shown in Figure 4.34. It can be seen from Figs. 4.33 and 4.34 that the FPSO and LNGC in tandem with cross-cable constraints have the similar motion responses as these without the mooring cable constraints. In another words, the present mooring constraints have very small effects on the motion responses when FPSO and LNGC are in tandem. Compared with the freely moving case, it can be seen that the present mooring cables failed to provide efficient constraints to prevent two vessels from approaching to each other.

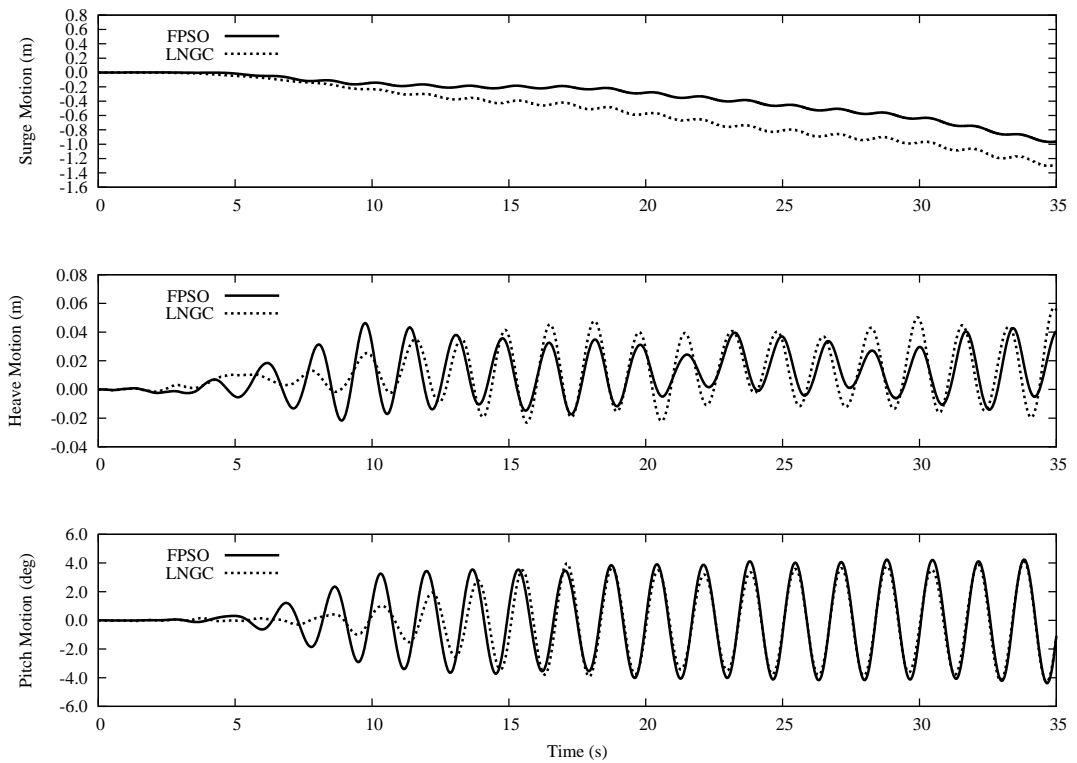


Figure 4.34: Comparison of motion responses of FPSO and LNGC in tandem with cross-mooring cable constraints

4.5.3 Comparisons of Different Configurations

To further investigate the effect of different position configurations on the motion responses of each ship, it is also of great interest to compare the motion responses of FPSO and LNGC in side-by-side and in tandem configurations. Due to the relatively large roll motion, the side-by-side FPSO and LNGC moored with spreading mooring system are not considered here. Thus the comparisons of motion responses of FPSO and LNGC in different position configurations without and with mooring cable constraints are shown in Figures 4.35-4.38. Specifically, Figures 4.35 and 4.36 compare motion responses of FPSO and LNGC in side-by-side and in tandem configurations without mooring cable constraints, respectively; Figures 4.37 and 4.38 compare motion responses of FPSO and LNGC with side mooring and in tandem mooring configurations, respectively.

In both cases with and without mooring configurations, as can be seen, FPSO (i.e., the large vessel in this configuration) accounts for similar motion responses in heave and pitch motions; however, significantly small responses in heave and pitch motions can be observed on the LNGC in tandem configuration. Moreover, significant motion responses in sway, roll, and yaw are observed in both vessels with side-by-side configuration with or without mooring constraints. In these motions mentions, the tandem mooring configuration has been shown to be more promising than side-by-side mooring configuration in extreme waves. However, the comparisons of surge motions in these figures shows that the tandem mooring configuration still needs special caution.

Though lack of comprehensive simulations conducted in this regard, the present numerical seakeeping tank has still been shown reliable for predicting ship motions for multiple-moored vessels in extreme waves.

4.6 Closure

In this chapter, the numerical seakeeping tank is used to investigate single ship and multiple ships motions induced by extreme waves. Highly nonlinear hydrodynamic phenomena such

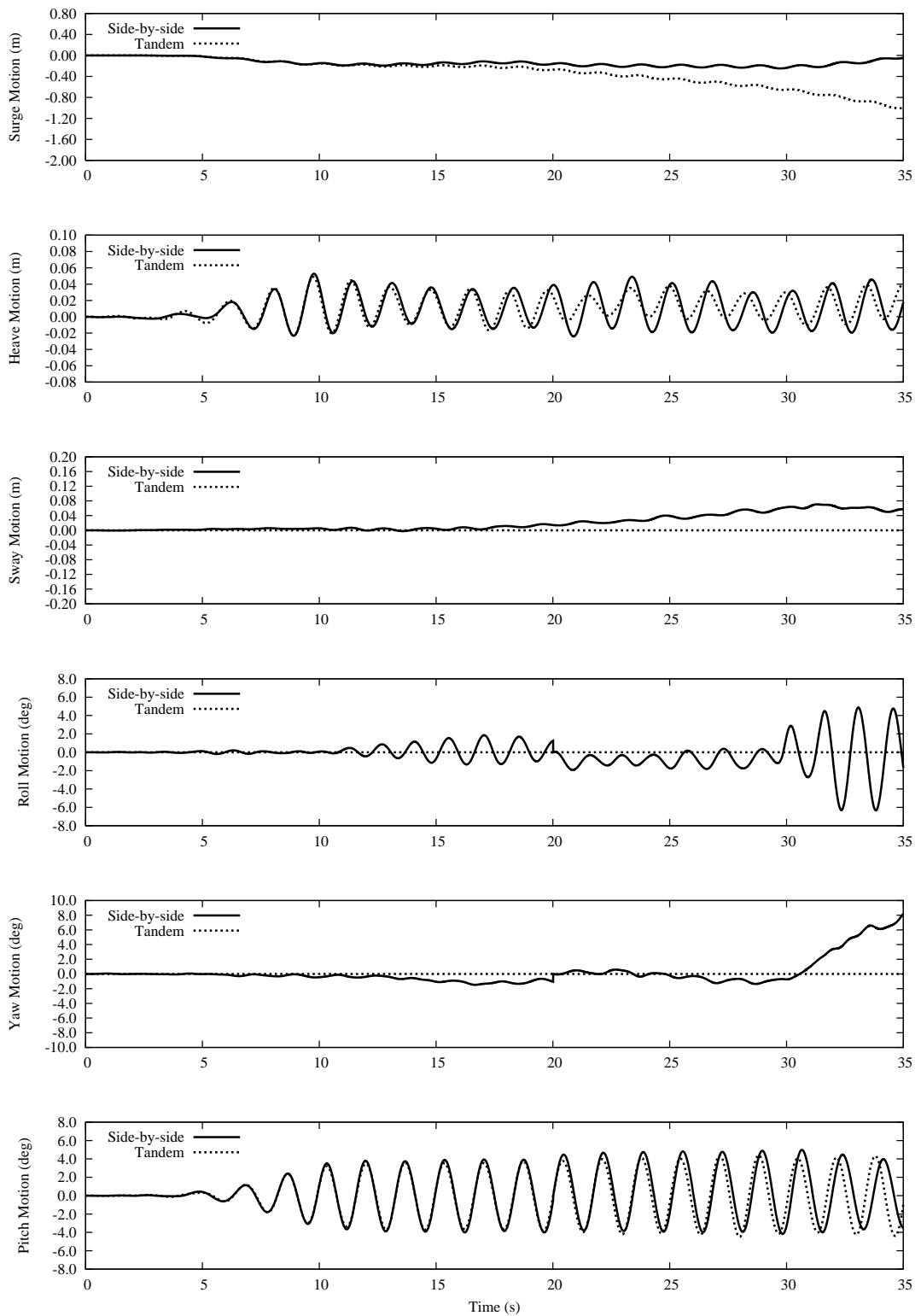


Figure 4.35: Comparison of motion responses of freely-moving FPSO in side-by-side and in tandem configurations

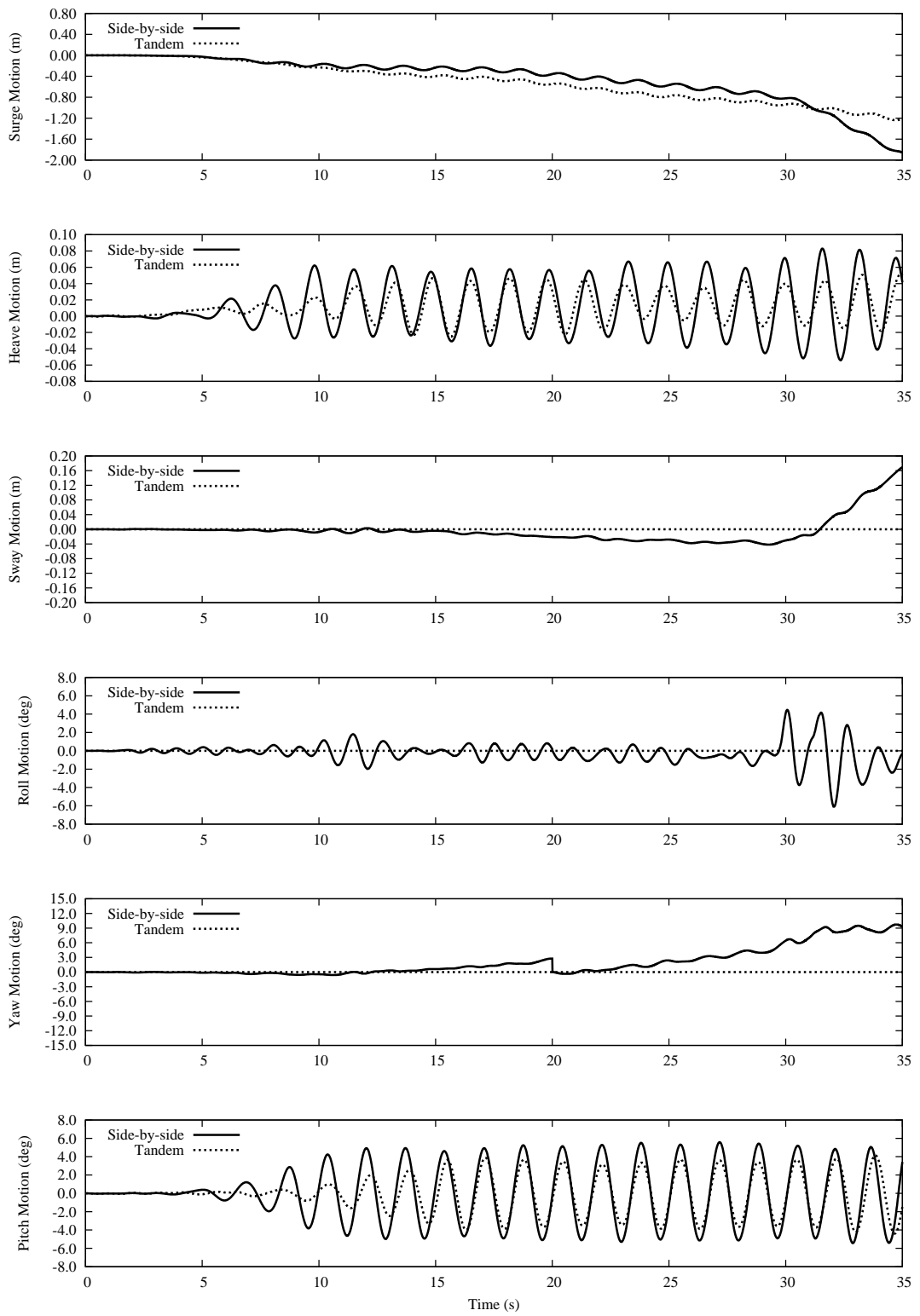


Figure 4.36: Comparison of motion responses of freely-moving LNGC in side-by-side and in tandem configurations

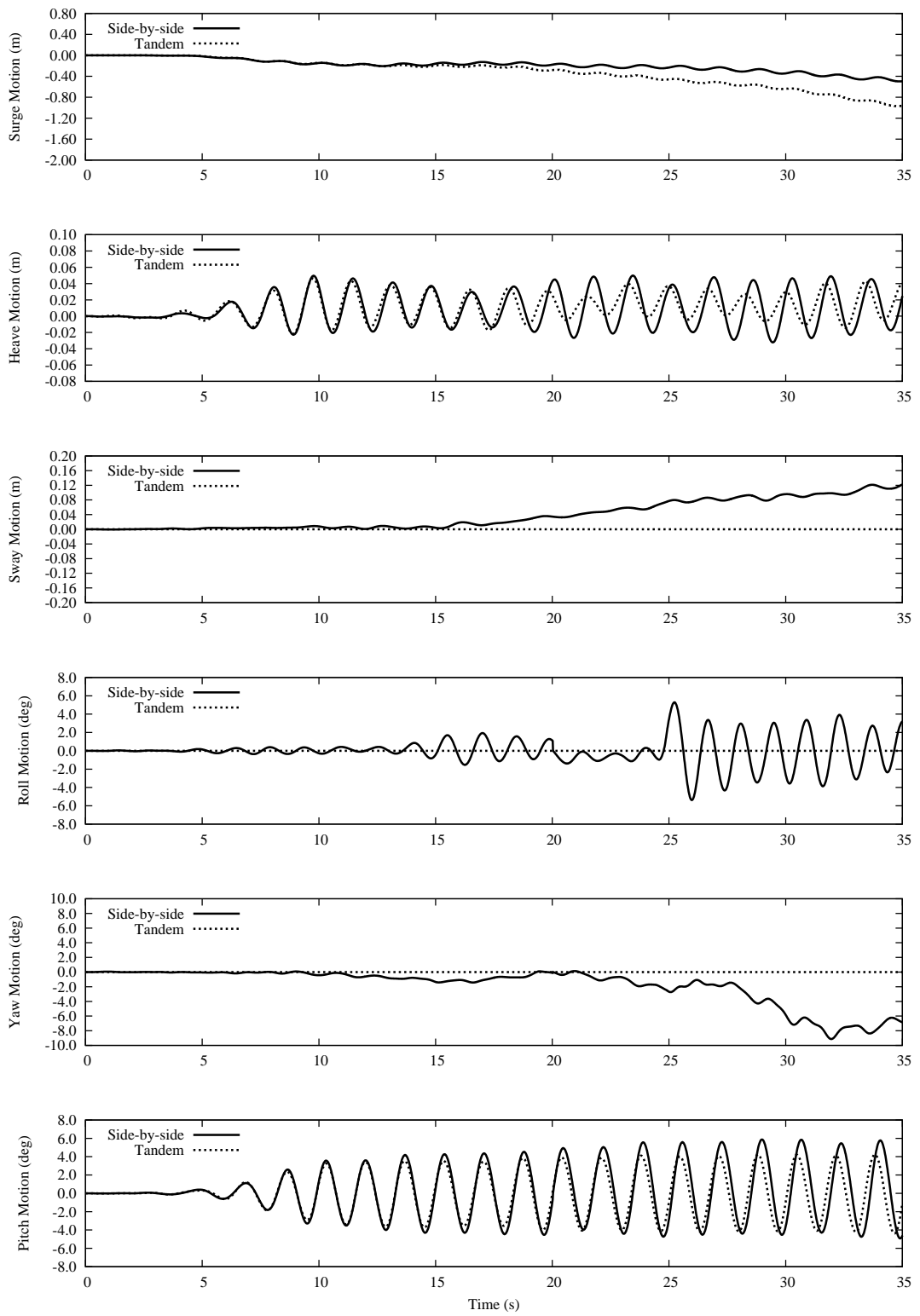


Figure 4.37: Comparison of motion responses of FPSO in side-by-side and in tandem configurations with mooring cable constraints

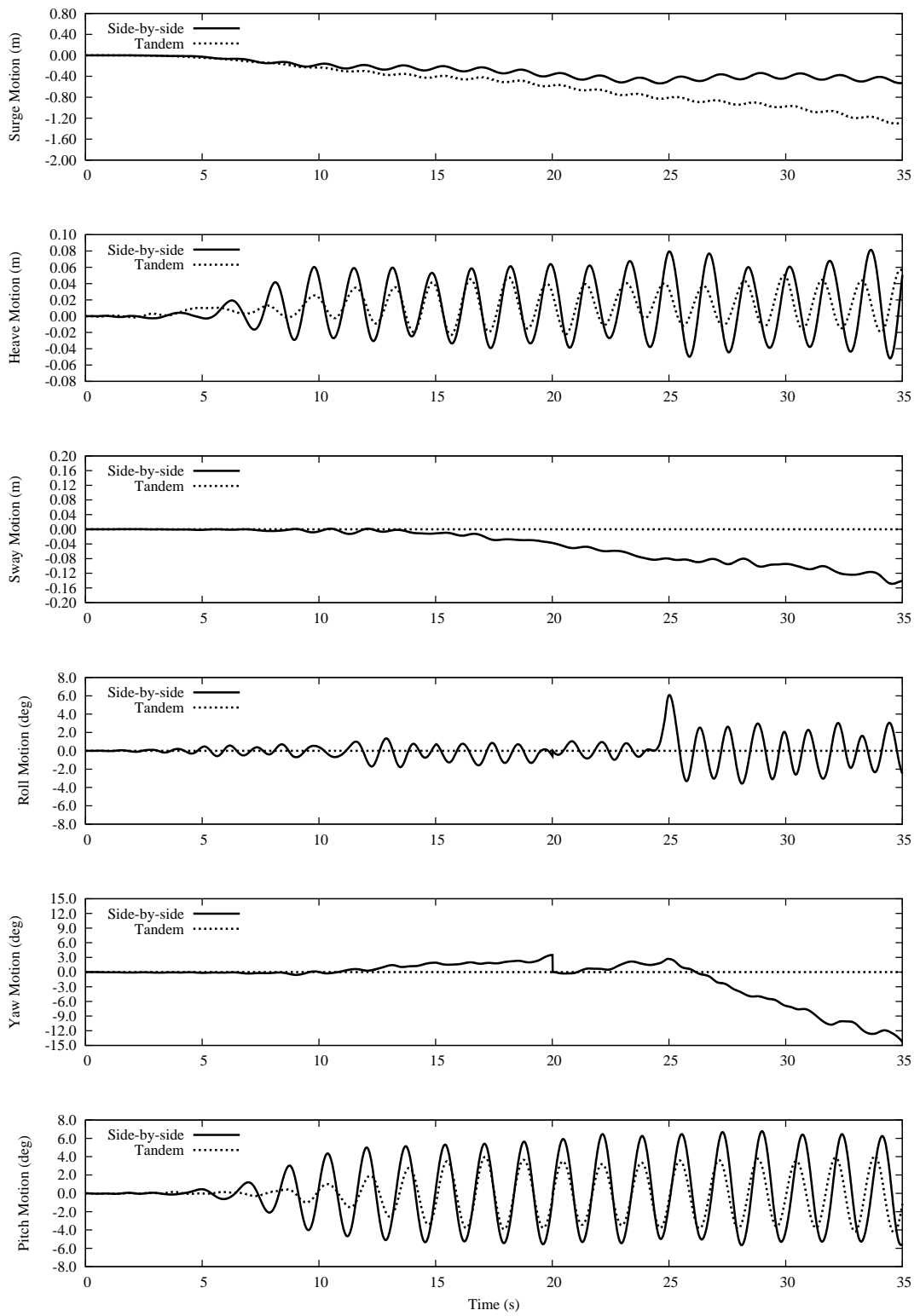


Figure 4.38: Comparison of motion responses of LNGC in side-by-side and in tandem configurations with mooring cable constraints

as green water on deck, wave-body interactions, ship-ship hydrodynamic interactions, and mooring effects have been successfully modeled. Ships with different mooring constraints in extreme waves are compared in detail. In addition, comparisons of ship motions with different position configurations are also presented. Base on these studies above, it has also be found in these studies that mooring cable constraints could help to reduce green water loads on ships if they are set properly.

Chapter 5: Summary and Conclusions

5.1 Summary and Conclusions

In this dissertation, a numerical seakeeping tank has been developed by integration of a simple mooring cable model, an unstructured grid-based incompressible flow solver, a VOF technique for capturing the free surface, and the general equations of rigid body motion (6-DOF).

With the aim of studying the ship motions induced by extreme waves, the numerical seakeeping tank is first validated by investigating the complex and highly nonlinear green water problems: green water overtopping a fixed deck and green water on deck of an FPSO model in extreme waves. The numerical results show a fairly good agreement with experimental measurements. Specially, in the first 2-D problem, a large transient wave is generated by a flap-type wavemaker in the numerical seakeeping tank. The whole process of the large wave overtopping on the deck, which includes wave approaching, overtopping, and separation, is captured in the numerical seakeeping tank. Wave elevation and velocity distribution are compared in detail with experimental measurements. In the 3-D green water on deck problem, a large regular wave is generated by a piston-type wavemaker. Highly nonlinear phenomena like green water shipping onto the deck has been simulated in the numerical seakeeping tank. Water height on the deck is also recorded and validated with experimental results. In addition, the simple mooring cable model is also validated by investigating the motions of two side-by-side boxes in a dam-breaking wave.

Finally, this validated numerical seakeeping tank is used to simulate motion responses of a single ship and two ships in side-by-side configuration and in tandem configuration in extreme waves. Highly nonlinear hydrodynamic phenomena such as green water on deck, wave-body interactions, ship-ship hydrodynamic interactions, and mooring cable effects

have been successfully modeled. In particular, single ship with different mooring constraints in extreme waves are compared in detail. Results shows that ship motions relative to the upcoming waves are very important to the green water shipping on deck and structure loading forces. Moreover, simulations of motion responses of multiple ships with different position configurations are also presented. More interactions are observed on the two ships with side-by-side configuration. The results also shows that different mooring configurations provide different effects in each motion response (upto 6-DOF), and multiple ships moored at certain distance in extreme waves require special caution.

Numerical results of all these case studies have demonstrated that the numerical sea-keeping tank presented in this dissertation can be used to predict ship motions induced by extremes waves, which are associated with highly nonlinear free surface flow problems such as green water problem, ship-ship hydrodynamic interactions, and mooring cable effects.

5.2 Future Work

In order to further study ship motions in extreme waves, future work on the development of the numerical seakeeping tank could focus on the following aspects:

- Coupling with a comprehensive FEM mooring model, which would provide more accurate mooring responses to the ship;
- Application of wave absorbing techniques to the numerical seakeeping tank;
- More validations such as impulse on the body surface and green water on the deck of the ship with different bow shapes; and
- Simulations of ship motions with forward speed in extreme waves.

Bibliography

Bibliography

- [1] J. N. Newman, “The theory of ship motions,” in *Advances in Applied Mechanics*. Academic Press, 1978, vol. 18, pp. 221–283.
- [2] T. Perez, *Ship Motion Control*. Springer, 2005.
- [3] O. Faltinsen, *Sea Loads on Ships and Offshore Structures*. Cambridge University Press, 1993.
- [4] BW Offshore, <http://www.bwoffshore.com/>, 2009.
- [5] Höegh LNG, <http://www.hoegh.com/lng//fleet/>, 2009.
- [6] D. W. Wang, D. A. Mitchell, W. J. Teague, E. Jarosz, and M. S. Hulbert, “Extreme waves under hurricane Ivan,” *Science*, vol. 309, p. 896, 2005.
- [7] B. Buchner, “Green water on ship-type offshore structure,” Ph.D. dissertation, Delft University of Technology, 2002.
- [8] K. B. Nielsen and S. Mayer, “Numerical prediction of green water incidents,” *Ocean Engineering*, vol. 31, pp. 363–399, 2004.
- [9] D. Llewelyn, M. Capsey, and E. Dyrkoren, “FPSO lessons learned - project report for OLF,” The Offshore Management Center, RGU, Tech. Rep., September 2002.
- [10] D. Cox and J. Ortega, “Laboratory observation of green water overtopping a fixed deck,” *Ocean Engineering*, vol. 29, pp. 1827–1840, 2002.
- [11] P. C. Sames, “Prediction of green water loads for a RoRo passenger ferry,” in *Proceedings of OMAE’02*, Oslo, Norway, June 2002.
- [12] J. Li, J. Yang, X. Liang, and M. Yao, “Model test for green water on FPSO,” *China Offshore Platform*, vol. 22(5), 2007.
- [13] Y. Ryu, K.-A. Chang, and R. Mercier, “Runup and green water velocities due to breaking wave impinging and overtopping,” *Exp Fluids*, vol. 43, pp. 555–567, 2007.
- [14] T. F. Ogilvie and E. O. Tuck, “A rational strip theory of ship motions: Part 1,” in *Report 013 Department of Naval Architecture and Marine Engineering*, Ann Arbor, 1969, pp. 92+ixp.
- [15] N. Salvesen, E. O. Tuck, and O. Faltinsen, “Ship motions and sea loads,” *Trans SNAME*, vol. 78, pp. 250–287, 1970.

- [16] M. S. Kashiwagi, S. Mizokami, H. Yasukawa, and Y. Fukushima, "Prediction of wave pressure and loads on actual ships by the enhanced unified theory," in *Proc 23rd Symp Naval Hydrodynamics*, Val de Reuil, France, 2000, pp. 95–109.
- [17] G. D. Weymouth, R. V. Wilson, and F. Stern, "Rans computational fluid dynamics predictions of pitch and heave ship motions in head seas," *J Ship Research*, vol. 49(2), pp. 80–97, 2005.
- [18] C. Hu and M. Kashiwagi, "Numerical and experimental studies on three-dimensional water on deck with a modified wigley model," in *Proc 9th Int Conf Num Hydrodynamics*, vol. 1, Michigan, USA, 2007, pp. 159–169.
- [19] B. Buchner, A. Dijk, and J. Wilde, "Numerical multiple-body simulations of side-by-side mooring to an FPSO," in *Proc 16th Int Offshore and Polar Eng Conf*, Stavanger, Norway, 2001.
- [20] S. Y. Hong, J. H. Kim, S. K. Cho, Y. R. Choi, and Y. S. Kim, "Numerical and experimental study on hydrodynamic interaction of side-by-side moored multiple vessels," *Ocean Engineering*, vol. 32, pp. 783–801, 2005.
- [21] J. R. Fournier, M. Naciri, and X. B. Chen, "Hydrodynamics of two side-by-side vessels experiments and numerical simulations," in *Proc. 16th ISOPE*, San Francisco, USA, 2006.
- [22] S. Cho, S. Hong, J. Kim, and I. Park, "Numerical studies of the nonlinear effect of sloshing on side-by-side moored LNGC and FSRU," in *Proc Int Conf Violent Flows*, Fukuoka, Japan, 2007.
- [23] M. Naciri, O. Waals, and J. Wilde, "Time domain simulations of side-by-side moored vessels lessons learn from a benchmark test," in *Proc 26th Int Conf Offshore Mech and Arctic Eng (OMAE2007)*, San Diego, USA, 2007.
- [24] G. X. Wu and R. E. Taylor, "Finite element analysis of two-dimensional nonlinear transient water waves," *Applied Ocean Research*, vol. 16, pp. 363–372, 1994.
- [25] G. X. Wu and R. E. Taylor, "Time stepping solutions of the two-dimensional nonlinear waves radiation problem," *Ocean Engineering*, vol. 22(8), pp. 785–798, 1995.
- [26] Q. W. Ma and S. Yan, "Quasi ALE finite element method for nonlinear water waves," *Journal of Computational Physics*, vol. 212, pp. 52–72, 2006.
- [27] M. S. Kirkgöz and M. Mamak, "Impulse modeling of wave impact pressures on vertical wall," *Ocean Engineering*, vol. 31, pp. 343–352, 2004.
- [28] C. Z. Wang and G. X. Wu, "An unstructured-mesh-based finite element simulation of wave interactions with non-wall-sided bodies," *Journal of Fluids and Structures*, vol. 22, pp. 441–461, 2006.
- [29] K. Trulsen, B. Spjelkavik, and E. Mehlum, "Green water computed with a spline-based collocation method for potential flow," *Int J Applied Mechanics Engineering*, vol. 7(1), pp. 107–123, 2002.

- [30] M. Greco, O. M. Faltinsen, and M. Landrini, “Shipping of water on a two-dimensional structure,” *J. Fluid. Mech.*, vol. 525, pp. 309–332, 2005.
- [31] J. J. Monaghan, “Simulating free surface flows with SPH,” *Journal of Computational Physics*, vol. 110, pp. 399–406, 1994.
- [32] M. Sussman, P. Smereka, and S. Osher, “A level set approach for computing solutions to incompressible two-phase flow,” *Journal of Computational Physics*, vol. 114, pp. 146–159, 1994.
- [33] R. Scardovelli and S. Zaleski, “Direct numerical simulation of free-surface and interfacial flow,” *Annual Review of Fluid Mechanics*, vol. 31, pp. 567–603, 1999.
- [34] A. Veldman, “The simulation of violent free-surface dynamics at sea and in space,” in *ECCOMAS CFD*, 2006.
- [35] D. Enright, “Use of the particle level set method for enhanced resolution of free surface flows,” Ph.D. dissertation, Stanford University, 2002.
- [36] C. Yang, H. Lu, R. Löhner, and W. C. Sandberg, “Computation of the three-dimensional nonlinear flow around a body in or near the free surface,” in *27th Intl Conf Offshore Mechanics Arctic Engineering (OMAE2008)*, Estoril, Portugal, June 2008.
- [37] F. H. Harlow and J. E. Welch, “Numerical study of large-amplitude free surface motions,” *Physics of Fluids*, vol. 8, pp. 2182–2189, 1965.
- [38] B. D. Nichols and C. W. Hirt, “Methods for calculating multi-dimensional, transient free surface flows past bodies,” in *Proc. First Intern. Conf. Num. Ship Hydrodynamics*, Gaithersburg, Maryland, 1975.
- [39] S. Osher and J. A. Sethian, “Fronts propagating with curvature-depend speed: Algorithms based on Hamilton-Jacobi formulations,” *Journal of Computational Physics*, p. 79(1), 1988.
- [40] C. W. Hirt and B. D. Nichols, “Volumes of fluid (VOF) method for the dynamics of free boundaries,” *Journal of Computational Physics*, vol. 39, pp. 201–225, 1981.
- [41] G. Chen and C. Kharif, “Two-dimensional navier-stokes simulations of breaking waves,” *Physics of Fluids*, vol. 11, pp. 121–133, 1999.
- [42] B. Biausser, P. Fraunie, S. Grilli, and R. Marcer, “Numerical analysis of the internal kinematics and dynamics of three-dimensional breaking waves on slopes,” *Int J Offshore and Polar Eng*, vol. 14, pp. 247–256, 2004.
- [43] G. Fekken, A. E. P. Veldman, and B. Buchner, “Simulation of green water using the Navier-Stokes equations,” in *Proc. of the 7th Int. Conf. on Numerical Ship Hydrodynamics*, Nantes, France, 1999.
- [44] R. H. M. Huijsmans and E. van Groesen, “Coupling freak wave effects with green water simulations,” in *Proceeding of the 14th ISOPE*, Toulon, France, May 2004.

- [45] S. H. Rhee, “Unstructured grid based Reynolds-Averaged Navier-Stokes method for liquid tank sloshing,” *J Fluids Eng*, vol. 127(3), pp. 572–582, 2005.
- [46] C. Yang and R. Löhner, “Computation of 3D flows with violent free surface motion,” in *Proc. 15th ISOPE*, Seoul, Korea, 2005.
- [47] C. Yang, R. Löhner, and H. Lu, “An unstructured-grid based Volume-of-Fluid method for extreme wave and freely-floating structure interaction,” *Journal of Hydrodynamics*, vol. 18(3): S. 1, pp. 415–422, 2006.
- [48] C. Yang, H. Lu, R. Löhner, X. Liang, and J. Yang, “An unstructured-grid based VOF method for ship motions induced by extreme waves,” in *9th Int Conf Num Ship Hydrodynamics*, Ann Arbor, USA, 2007.
- [49] C. Yang, H. Lu, R. Löhner, X. Liang, and J. Yang, “Numerical simulation of highly nonlinear wave-body interactions with experimental validation,” in *Proc Int Conf Violent Flows (VF-2007)*, Fukuoka, Japan, 2007.
- [50] H. Lu, C. Yang, and R. Löhner, “Numerical studies of green water on a moored FPSO,” in *Proc 18th Int Offshore and Polar Eng Conf (ISOPE)*, Vancouver, Canada, 2008.
- [51] R. Löhner, *Applied CFD Techniques: an introduction based on finite element methods*, 2nd ed. John Wiley & Sons, Ltd, 2008.
- [52] R. Löhner, “Multistage explicit advective prediction for projection-type incompressible flow solvers,” *Journal of Computational Physics*, vol. 195, pp. 143–152, 2004.
- [53] R. Löhner, C. Yang, and E. Oñate, “Simulation of flows with violent free surface motion and moving objects using unstructured grids,” *International Journal for Numerical Methods in Fluids*, vol. 53, 1315–1338.
- [54] C. Yang and R. Löhner, “On the modeling of highly nonlinear wave-body interactions,” in *Proc 16th Int Offshore and Polar Eng Conf (ISOPE)*, San Francisco, 2006.
- [55] H. Lu, C. Yang, and R. Löhner, “Numerical studies of ship-ship interactions in extreme waves,” in *GCMS09*, Istanbul, Turkey, July 2009.
- [56] J. Kim and P. Moin, “Application of a fractional-step method to incompressible Navier-Stokes equations,” *Journal of Computational Physics*, vol. 59, pp. 308–323, 1985.
- [57] P. M. Gresho, C. C. Upson, S. Chan, and R. L. Lee, “Recent progress in the solution of the time-dependent, three-dimensional, incompressible Navier-Stokes equations,” in *Proc. 4th Int. Symp. Finite Element Methods in Flow Problems*, (T. Kawai ed.), 1982, pp. 153–162.
- [58] J. B. Bell and D. L. Marcus, “A second-order projection method for variable-density flows,” *Journal of Computational Physics*, vol. 101(2), pp. 334–348, 1992.
- [59] B. Alessandrini and G. Delhommeau, “A multigrid velocity-pressure- free surface elevation fully coupled solver for calculation of turbulent incompressible flow around a hull,” in *Proceedings of the 21st Symposium on Naval Hydrodynamics*, Trondheim, Norway, 1996.

- [60] Y. Kallinderis and A. Chen, “An incompressible 3-D Navier-Stokes method with adaptive hybrid grids,” *AIAA-96-0293*, 1996.
- [61] J. Donea, S. Giuliani, H. Laval, and L. Quartapelle, “Solution of the unsteady Navier-Stokes equations by a fractional step method,” *Computer Methods in Applied Mechanics and Engineering*, vol. 30, pp. 53–73, 1982.
- [62] P. M. Gresho and S. Chan, “On the theory of semi-implicit projection methods for viscous incompressible flows and its implementation via a finite element method that introduces a nearly-consistent mass matrix,” *International Journal for Numerical Methods in Fluids*, vol. 11, pp. 587–620, 1990.
- [63] R. Löhner, “A fast finite element solver for incompressible flows,” *AIAA-90-0398*, 1990.
- [64] D. Martin and R. Löhner, “An implicit linelet-based solver for incompressible flows,” *AIAA-92-0668*, 1992.
- [65] R. Ramamurti and R. Löhner, “A parallel implicit incompressible flow solver using unstructured meshes,” *Computers and Fluids*, vol. 5, pp. 119–132, 1996.
- [66] A. Takamura, M. Zhu, and D. Vinteler, “Numerical simulation of pass-by maneuver using ALE technique,” in *JSAE Annual Conference*, Tokyo, Japan, May 2001.
- [67] E. Eaton, “Aero-acoustics in an automotive HVAC module,” in *American PAM User Conference*, Birmingham, Michigan, 2001.
- [68] R. Löhner, “Matching semi-structured and unstructured grids for Navier-Stokes calculations,” *AIAA-93-3348-CP*, 1993.
- [69] R. Löhner, “Overlapping unstructured grids,” *AIAA-01-0439*, 2001.
- [70] R. G. Dean and R. A. Dalrymple, *Water Wave Mechanics For Engineering and Scientists*. World Scientific Publishing Company, 1991.
- [71] S. A. Hughes, *Physical Models and Laboratory Techniques in Coastal Engineering*, ser. Advanced Series on Ocean Engineering. World Scientific Publishing Company, Inc., 1993, vol. 7.
- [72] R. Löhner, C. Yang, and E. Oñate, “Large-scale simulation of flows with violent free surface motion,” in *International Conference on Computational Methods Marine Engineering (MARINE2005)*, Barcelona, Spain, 2005.
- [73] M. Gomez-Gesteira, D. Cerqueiro, C. Crespo, and R. A. Dalrymple, “Green water overtopping analyzed with a SPH model,” *Ocean Engineering*, vol. 32, pp. 223–238, 2005.
- [74] B. Buchner and T. Bunnik, “Extreme wave effects on deepwater floating structures,” in *Offshore Technology Conference (OTC 18493)*, Houston, Texas, USA, April - May 2007.
- [75] U. P. Bulgarelli, “The application of numerical methods of the solution of some problems in free-surface hydrodynamics,” *Journal of Ship Research*, vol. 49, pp. 288–301, 2005.

- [76] H. Chen and K. Yu, “Numerical simulation of wave runup and greenwater on offshore structures by a level-set rans method,” in *Proce. 16th ISOPE*, San Francisco, USA, May 2006.
- [77] C. Hu, M. Kashiwagi, and A. Kitadai, “Numerical simulation of strongly nonlinear wave-body interactions with experimental validation,” in *Proceeding of the 16th ISOPE*, San Francisco, USA, May - Jun 2006.
- [78] J. M. Hyman, “Numerical methods for tracking interfaces,” *Physica*, vol. 12D, pp. 396–407, 1984.
- [79] B. J. Koo and M. H. Kim, “Global analysis of fpso and shuttle tankers during side-by-side offloading,” *Final Project Report for MMS*, March 2006.
- [80] P. Lin and P. L.-F. Liu, “A numerical study of breaking waves in the surface zone,” *Journal of Fluid Mechanics*, vol. 359, pp. 239–264, 1998.
- [81] R. Löhner, “Regridding surface triangulations,” *Journal of Computational Physics*, vol. 126, pp. 1–10, 1996.
- [82] R. Löhner, C. Yang, J. Cebral, F. C. O. Soto, and J. Waltz, “Improving the speed and accuracy of projection-type incompressible flow solvers,” *Computer Methods in Applied Mechanics and Engineering*, vol. 195, pp. 3087–3109, 2006.
- [83] R. Löhner, C. Yang, and E. Oñate, “On the simulation of flows with violent free surface motion,” *AIAA-06-0291*, 2006.
- [84] L. Poldervaart, H. Oomen, and J. Ellis, “Offshore lng transfer: A worldwide review of offloading availability,” in *Offshore Technology Conference (OTC 18026)*, Houston, USA, 2006.
- [85] E. Stein, R. de Borst, and T. Hughes, *Encyclopedia of Computational Mechanics*. John Wiley & Sons, Ltd., 2004.
- [86] C. Yang and R. Löhner, “Fully nonlinear ship wave calculation using unstructured grids and parallel computing,” in *Proc. 3rd Osaka Col. on Advanced CFD Appl. to Ship Flow and Hull Form Design*, Osaka, Japan, 1998.
- [87] R. Zhu, G. Miao, and Z. Lin, “Numerical research on FPSOs with green water occurrence,” *Journal of Ship Research*, vol. 53(1), pp. 7–18, 2009.

Curriculum Vitae

Haidong Lu was born on Oct 21, 1979 in Haimen, Jiangsu Province, China. He got his Bachelor Degree in Engineering in 2001 at University of Shanghai for Science and Technology (USST), Shanghai, China; in 2004, he graduated from Institute of Fluid Mechanics at USST and finished Master in Engineering with the thesis of Experimental Study on Dense Phase Pneumatic Conveying in Pipe-lines. He joined the CFD group at George Mason University in the following Fall semester (2004) as a Ph.D. student.